UNIVERSITAT JAUME·I

Programa de Doctorado en Ciencias

Escuela de Doctorado de la Universitat Jaume I

Development of transparent semiconductor oxides with optical properties for the functionalization of glass surfaces

Memoria presentada por Jaime González Cuadra para optar al grado de doctor la Universitat Jaume I

JAIME|GONZALEZ|CUADRA
Firmado digitalmente por JAIME|GONZALEZ|CUADRA
Fecha: 2023.11.15 09:15:56 +01'00'

Jaime González Cuadra

Assinado por: **João António Labrincha Baptista**
Num. de Identificação: 06052832
Data: 2023.11.15 08:28:34+00'00'
CHAVE MÓVEL

Prof. Dr. João Antonio Labrincha

DIEGO|FRAGA|CHIVA
Firmado digitalmente por DIEGO|FRAGA|CHIVA
Fecha: 2023.11.15 12:09:54 +01'00'

Dr. Diego Fraga Chiva

Castellón, Diciembre de 2023

“Be the flame, not the moth”

Giacomo Casanova

Acknowledgements

I would like to take this opportunity to thank everyone who has helped me in some manner to bring this thesis to completion.

Professor Juan Bautista Carda and Dr. Diego Fraga Chiva, my thesis advisors, provided me with the opportunity to produce this thesis. Without their assistance, guidance, and perseverance, it would have been impossible to complete this thesis.

I would also like to thank Professor João Labrincha, co-director of this thesis, for allowing me to work in his lab at the institute of materials of Aveiro (CICECO) and for his assistance with all the publications produced during this thesis, as well as Professor Tito Trindade of the chemistry department of CICECO for his assistance and supervision.

I would also like to thank my colleagues at all three places where I was able to complete this thesis: the solid state chemistry group at Universitat Jaume I, the department of Materials and Ceramic Engineering (DEMaC), and the nanoLAB both belonging to the University of Aveiro. Thank you for your unwavering support and for always feeling so accompanied.

I would also like to acknowledge the technicians of the serveis centrals d' instrumentació cientfica (SCIC) for providing the resources necessary for the advancement of my research.

We would also like to thank the project PID2020-116719RB-C43 funded by MCIN/ AEI /10.13039/501100011033 for the funding they have given to carry out this doctoral thesis.

Acknowledgements

I would also like to thank the “Cátedra de innovación Cerámica Ciutat de Vila-real" for the support to the diffusion and dissemination of the results obtained in this doctoral thesis. I would like to make a special mention to my mother, as she has always supported me in everything I have done and without her help the completion of this thesis would have been impossible.

Last but not least, I would like to thank all my friends for their unconditional help and support, whose presence has made this last part of the thesis much easier and more enjoyable.

To all of you, thank you very much.

Acknowledgements

Financial Support

This thesis has been made possible thanks to the funding obtained through the projects:

- Project PID2020-116719RB-C43 funded by MCIN/ AEI/10.13039/501100011033.
- Project TED2021-130963B-C22 funded by AEI/10.13039/501100011033/Union Europea NextGenerationEU/PPTR.

Thanks were also due to the European Ceramic Society (ECERS) through the JECS trust (Contract 2022308) for its funding through the mobility programmes for financing the relevant stays developed in this study.

Summary

Semiconductor oxide thin films have sparked significant interest in the realm of materials science and engineering due to their distinct physical, chemical, and electrical characteristics, rendering them valuable in a broad array of applications. These films typically possess thicknesses ranging from a few nanometers to a few micrometers and are commonly deposited on different substrates utilizing diverse techniques like sputtering, pulsed laser deposition, or chemical vapor deposition.

Extensive research is being conducted on oxide thin films for their potential applications in microelectronics, optics, energy storage, sensing, and catalysis. For instance, in the field of microelectronics, oxide thin films are being investigated for their suitability as high-k gate dielectrics, ferroelectric memory elements, and transparent conductive oxides for displays and solar cells. In optics, these thin films find utility as anti-reflective coatings, optical filters, and waveguides. In the realm of energy storage, oxide thin films are employed in supercapacitors, batteries, and fuel cells.

The present thesis is focused on the synthesis of transparent thin films on glass surfaces in order to provide them with new properties such as the degradation of contaminants or bacterial agents. This objective originates from the daily emergence of new social needs, which necessitates the constant production of new materials to help build a better future. It is a proven fact that there is a growing demand for new, highly specialised materials that are capable of meeting society's diverse requirements. One of these needs is the generation of an environment free of pollutants and pathogenic bacteria that can affect our health.

Summary

In this sense, the present thesis deals with the synthesis, characterisation and application of oxides, both in powder and thin film form, which have a wide range of applications. In particular titanium oxides and zinc oxides, functionalised with nanoparticles in order to improve their properties as antimicrobial agents or photocatalysts. This wide range of applications lies in the fact that these thin-film synthesised oxides absorb UV radiation by forming reactive oxygen species capable of degrading pollutants such as bacterial agents. Moreover, as they are synthesised in thin film form they do not affect the transparency of the substrate and are easily functionalised with nanoparticles improving their optical properties.

In this way, using the oxides ZnO and TiO_2, the study of their optical properties and their use as photocatalysts has been approached.

This doctoral thesis is therefore divided into four parts. Chapter 1 is centred around an introductory chapter, which is dedicated to the study of the structural characteristics of these oxides, the different phases that can be formed depending on the structure, as well as the different synthesis methods to produce both powder and thin films. In addition, the use of these oxides as photocatalysts and their different applications thanks to this property will be introduced.

Chapter 2 sets out the objectives of this doctoral thesis, following on from chapter 3 which is based on the synthesis and characterisation of a ZnO-based composite with Ag NPs that has strong bactericidal and bacteriostatic properties in order to obtain a powder to functionalise surfaces and give them new properties.

Summary

This section led to the publication of a scientific article in a high impact journal in this field, Applied Sciences (Switzerland).

A third part, corresponding to chapter 4 and 5, where transparent thin layers are directly generated on glass surfaces in order to give them other properties, in this case photocatalytic and bactericidal activity. Fundamentally, the interaction of UV light with these films was studied and how they were able to generate reactive oxygen species in order to degrade environmental pollutants or bacteria.

Specifically, chapter 4 is based on the study of transparent TiO_2 thin films whose photocatalytic and bactericidal properties are enhanced by incorporating Ag NPs on their surface and chapter 5 is based on transparent ZnO thin films on glass also studying their interaction with UV light to evaluate the same properties as in the case of titanium oxide. This section resulted in the publication of two scientific articles in the high impact journals in this field, Applied Surface Science and Ceramics Internacional.

Finally, in the last chapter, chapter 6, the different conclusions drawn from the studies carried out in this thesis are presented as a whole.

Summary

Las películas finas de óxido semiconductor han despertado un gran interés en el campo de la ciencia y la ingeniería de materiales debido a sus características físicas, químicas y eléctricas, que las hacen valiosas para una amplia gama de aplicaciones. Estas películas suelen tener espesores que oscilan entre unos pocos nanómetros y unos pocos micrómetros y suelen depositarse sobre distintos sustratos utilizando diversas técnicas como el sputtering, la deposición por láser pulsado o la deposición química en fase vapor.

Se están llevando a cabo numerosas investigaciones sobre las películas finas de óxido por sus posibles aplicaciones en microelectrónica, óptica, almacenamiento de energía, detección y catálisis. En el campo de la microelectrónica, por ejemplo, se están investigando las películas finas de óxido por su idoneidad como dieléctricos de puerta de alta k, elementos de memoria ferroeléctricos y óxidos conductores transparentes para pantallas y células solares. En el campo de la óptica, estas películas finas son útiles como revestimientos antirreflectantes, filtros ópticos y guías de ondas. En el campo del almacenamiento de energía, las películas finas de óxido se emplean en supercondensadores, baterías y pilas de combustible.

La presente tesis se centra en la síntesis de películas delgadas transparentes sobre superficies de vidrio para dotarlas de nuevas propiedades como la degradación de contaminantes o agentes bacterianos. Este objetivo tiene su origen en la aparición diaria de nuevas necesidades sociales, que hacen necesaria la producción constante de nuevos materiales que ayuden a construir un futuro mejor.

Summary

Es un hecho probado que existe una demanda creciente de nuevos materiales altamente especializados que sean capaces de satisfacer las diversas necesidades de la sociedad. Una de estas necesidades es la generación de un medio ambiente libre de contaminantes y bacterias patógenas que puedan afectar a nuestra salud.

En este sentido, la presente tesis aborda la síntesis, caracterización y aplicación de óxidos, tanto en polvo como en lámina delgada, que presentan un amplio abanico de aplicaciones. En particular, óxidos de titanio y óxidos de zinc, funcionalizados con nanopartículas para mejorar sus propiedades como agentes antimicrobianos o fotocatalizadores. Este amplio abanico de aplicaciones radica en que estos óxidos sintetizados en capa fina absorben la radiación UV formando especies reactivas de oxígeno capaces de degradar contaminantes como los agentes bacterianos. Además, al estar sintetizados en forma de película fina no afectan a la transparencia del sustrato y son fácilmente funcionalizables con nanopartículas mejorando sus propiedades ópticas.

De esta forma, utilizando los óxidos ZnO y TiO_2, se ha abordado el estudio de sus propiedades ópticas y su uso como fotocatalizadores.Esta tesis doctoral se divide, por tanto, en cuatro partes. El capítulo 1 se centra en un capítulo introductorio, dedicado al estudio de las características estructurales de estos óxidos, las diferentes fases que se pueden formar en función de la estructura, así como los diferentes métodos de síntesis para producir tanto polvo como láminas delgadas. Además, se introducirá el uso de estos óxidos como fotocatalizadores y sus diferentes aplicaciones gracias a esta propiedad.

Summary

En el capítulo 2 se exponen los objetivos de esta tesis doctoral, dando continuidad al capítulo 3 que se basa en la síntesis y caracterización de un compuesto a base de ZnO con NPs de Ag que presenta fuertes propiedades bactericidas y bacteriostáticas con el fin de obtener un polvo para funcionalizar superficies y dotarlas de nuevas propiedades.

Esta sección dio lugar a la publicación de un artículo científico en una revista de gran impacto en este campo, Applied Sciences (Suiza).

Una tercera parte, correspondiente a los capítulos 4 y 5, en la que se generan directamente capas finas transparentes sobre superficies de vidrio para conferirles otras propiedades, en este caso actividad fotocatalítica y bactericida. Fundamentalmente, se estudió la interacción de la luz UV con estas películas y cómo eran capaces de generar especies reactivas de oxígeno para degradar contaminantes ambientales o bacterias.

En concreto, el capítulo 4 se basa en el estudio de láminas delgadas transparentes de TiO_2 cuyas propiedades fotocatalíticas y bactericidas se ven potenciadas al incorporar NPs de Ag en su superficie y el capítulo 5 se basa en láminas delgadas transparentes de ZnO sobre vidrio estudiando también su interacción con la luz UV para evaluar las mismas propiedades que en el caso del óxido de titanio. Este apartado ha dado lugar a la publicación de dos artículos científicos en las revistas de mayor impacto en este campo, Applied Surface Science y Ceramics Internacional.

Finalmente, en el último capítulo, el 6, se presentan en conjunto las diferentes conclusiones extraídas de los estudios realizados en esta tesis.

List of abbreviations

AR	Avarage Roughnesss
XRD	X-Ray Diffraction
GIXRD	Grazing Incidence X-ray diffraction
EDX	Energy Dispersive X-Ray
PL	Photoluminiscense
TiO_2	Titanium Dioxide
PLAL	Pulsed Laser Ablation
JCPPDS	Joint Committee on Powder Diffraction Standards
NPs	Nanoparticles
RhB	Rhodamine B
ROS	Reactive Oxide Species
SEM	Scanning Electron Microscopy
TEM	Transmission Electron Microscopy
4-NP	4-Nitrophenol
UV/Vis	Ultraviolet-Visible
XPS	X-Ray Photoelectron Spectroscopy
RMS	Root-mean-square
OH•	Hydroxyl radicals
ICP-MS	Inductively coupled plasma mass spectrometry
DNA	Deoxyribonucleic acid
ZnO	Zinc Oxide

Table of contents

Table of contents

RELATED ARTICLES TO THIS THESIS

J.G. Cuadra, L. Scalschi, B. Vicedo, M. Guc, V. Izquierdo-roca, S. Porcar, D. Fraga, J.B. Carda, applied sciences ZnO / Ag Nanocomposites with Enhanced Antimicrobial Activity, (2022) 1–13. https://doi.org/10.3390/app12105023.

J.G. Cuadra, S. Molina-Prados, G. Mínguez-Vega, A.C. Estrada, T. Trindade, C. Oliveira, M.P. Seabra, J. Labrincha, S. Porcar, R. Cadena, D. Fraga, J.B. Carda, Multifunctional Silver-Coated Transparent TiO_2 Thin Films for Photocatalytic and Antimicrobial Applications, Appl. Surf. Sci. 617 (2023) 156519. https://doi.org/10.1016/j.apsusc.2023.156519.

J.G. Cuadra, A.C. Estrada, C. Oliveira, L.A. Abderrahim, S. Porcar, D. Fraga, T. Trindade, M.P. Seabra, J. Labrincha, J.B. Carda, Functional properties of transparent ZnO thin films synthetized by using spray pyrolysis for environmental and biomedical applications, Ceram. Int. (2023). https://doi.org/10.1016/j.ceramint.2023.07.246.

During the PhD process the following works have also been published:

S. Porcar, J.G. Cuadra, D. Fraga, T. Stoyanova Lyubenova, G. Soraca, J.B. Carda, Effect of al, ga, and in doping on the optical, structural, and electric properties of ZnO thin films, Appl. Sci. 11 (2021). https://doi.org/10.3390/app112110122.

J.B. Carda Castelló, D. Fraga Chiva, E.Barrachina Albert, I. Calvet Roures, J.G. Cuadra, S. Porcar García, Ciència dels materials: metalls, ceràmiques i polímers, 2022. https://doi.org/10.6035/sapientia181.

J.G. Cuadra, S. Porcar, D. Fraga, T. Stoyanova-Lyubenova, J.B. Carda, Enhanced Electrical Properties of Alkali-Doped ZnO Thin Films with Chemical Process, Solar. 1 (2021) 30–40. https://doi.org/10.3390/solar1010004.

CHAPTER 1

Introduction

“Nature has evolved for millions of years to solve problems. If we can learn from that and emulate it, we can solve many technological problems.”

Joanna Aizenberg

1.1. Motivation of work

Semiconductor oxide thin films have garnered significant interest in the field of materials science and engineering due to their unique physical, chemical, and electrical properties, making them useful in a wide range of applications [1,2]. These thin films typically have a thickness ranging from a few nanometers to a few micrometers and are typically deposited on various substrates using different techniques, such as sputtering, pulsed laser deposition, or chemical vapor deposition [3–5]. Oxide thin films are being extensively researched for their potential applications in microelectronics, optics, energy storage, sensing, and catalysis [6–8] (Figure 1.1).

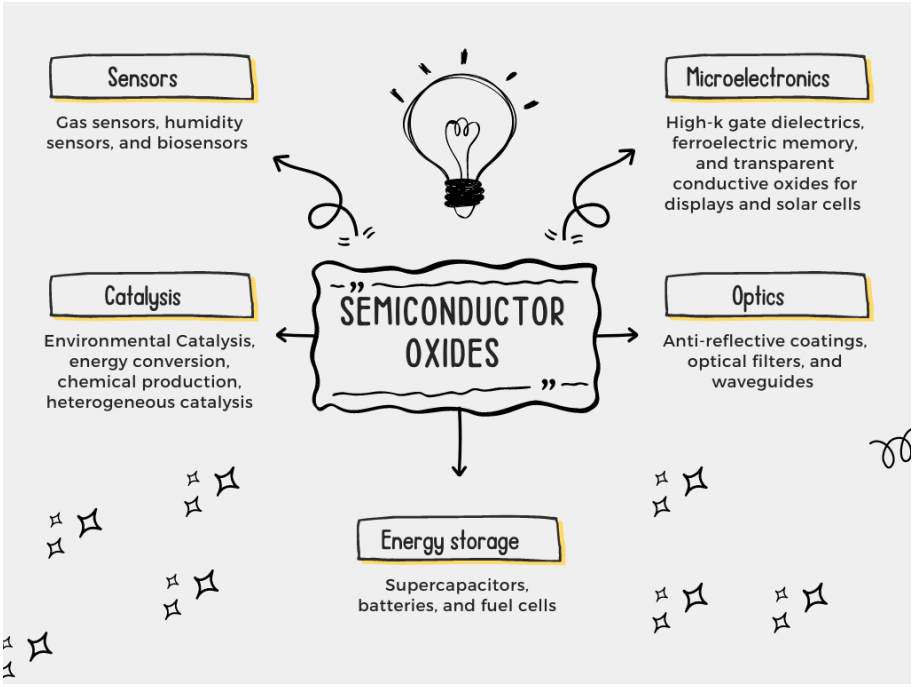

Figure 1.1 Potential applications of oxide semiconductors

For example, in microelectronics, oxide thin films are being explored for their use in high-k gate dielectrics, ferroelectric memory, and transparent conductive oxides for displays and solar cells [9–12]. In optics, these thin films are used as anti-reflective coatings, optical filters, and waveguides [13,14] . In energy storage, oxide thin films are used in supercapacitors, batteries, and fuel cells [15–17], while in sensing, these thin films are utilized as gas sensors, humidity sensors, and biosensors [18,19].

Additionally, oxide thin films also have applications in catalysis, where they are used as catalysts or catalyst supports in various chemical reactions. A branch of catalysis with more interest in the field of thin films is photocatalysis. Photocatalysis is a process that utilizes light energy to drive chemical reactions, and it has become a critical area of research due to its potential applications in various fields, including energy production, environmental remediation, and medicine [20–24]. One of the key advantages of thin film oxides in photocatalysis is that they offer a large surface area-to-volume ratio, which enhances their catalytic activity [25,26].This is because the high surface area allows for more efficient light absorption and greater interaction between the catalyst and the reactants [27].

In addition, thin film oxides can be engineered to have specific properties that are tailored to the desired photocatalytic application. For example, the morphology, crystal structure, and chemical composition of the oxide film can be adjusted to optimize its performance for a particular reaction [28,29].

Overall, the use of thin film oxides in photocatalysis research is critical for advancing this field and developing new technologies that can benefit society. With continued research and development, it is likely that thin film oxides will play an increasingly important role in the development of new and improved photocatalytic systems in the future [30,31].

The most commonly used oxide thin films are metal oxides, such as titanium dioxide (TiO_2), zinc oxide (ZnO), and indium oxide (In_2O_3), and transition metal oxides, such as tungsten oxide (WO_3), molybdenum oxide (MoO_3), bismuth vanadate ($BiVO_4$) and vanadium oxide (VO_x) [32–36].

1.2. Semiconductor Oxides

1.2.1. Crystal Structure and Defects in Semiconductor Oxides

Semiconductors can be differentiated based on many criteria, which are contingent upon their specific characteristics and intended uses. One possible approach of categorising these compounds is by examining their electronic band structure, the periodic table (namely groups 2,3,4,5 and 6 compounds), crystalline structure, or electrical characteristics. None of the aforementioned classification schemes can be universally deemed as entirely satisfactory [37,38].

Consequently, we refrain from adhering to any particular and inflexible scheme. Instead, we employ these diverse schemes selectively, based on their utility in characterising distinct materials and their respective applications. To gain a comprehensive understanding and provide an accurate depiction of semiconductors, it is imperative to take into account their interatomic bonding arrangements, structural features, and the diverse defects that exist within the material.

This chapter begins by examining the many types of interatomic bonding that exist in different solid materials. Subsequently, we proceed to give several definitions pertaining to the crystalline structure. Hence, while it is theoretically possible to employ either the interatomic bonding or structural symmetry notions for categorization purposes, these approaches are inadequate for fully describing the physical properties and behaviour of semiconductors.

In order to classify and provide a comprehensive description of the physical features of semiconductors, it is imperative to examine the electronic band structure, which will be discussed in the next sections.

The primary classifications of solids, with respect to their structural organisation, encompass crystalline, polycrystalline, and amorphous states. It is important to acknowledge that a significant proportion of semiconductors employed in electronic applications are characterised by their crystalline nature .

However, it is worth mentioning that several electronic devices have also incorporated polycrystalline and amorphous semiconductors, which have demonstrated diverse utility in various applications.

Crystalline materials exhibit a periodic and consistently repeated three-dimensional arrangement of atoms. The explanation of crystals involves the definition of a lattice, which may be seen as a periodic arrangement of lattice points in three dimensions. In such an array, every point possesses identical surrounds.

The complete solid can be replicated through the iterative translation of the primordial cell in three spatial dimensions. In order to achieve geometrical simplicity, it is also feasible to opt for a bigger atomic arrangement, known as a unit cell, as the fundamental constituent of the crystalline substance. The succeeding chapters provide a detailed account of semiconductors, emphasising their classification as solids through the principle of periodicity [39].

This characterization holds significant significance as it simplifies the analysis by focusing on a single unit cell, rather than an extensive assembly of approximately 5×10^{22} atoms cm^{-3}.

Polycrystalline materials consist of many crystalline areas, commonly referred to as grains, which exhibit distinct orientations and are demarcated by grain boundaries. Amorphous semiconductors, in contrast to their crystalline counterparts, exhibit a lack of long-range order and possess only short-range order without any periodic arrangement.

The explanation of the crystalline structure involves the definition of a lattice, which can be characterised as a periodic arrangement of points in three dimensions. These points, known as lattice points, exhibit similar surroundings. The crystal formations are created through the arrangement of individual atoms or groups of identical atoms on or in close proximity to these lattice points. In three-dimensional space, the number of distinct arrangements of lattice points with identical surroundings is limited to a total of 14 [39].

In principle, it is possible to replicate all crystal formations through the iterative displacement of an atom or a cluster of atoms at any location inside one of the 14 point lattices known as Bravais space lattices. These lattices are associated with the seven crystal systems, each characterised by a distinct set of axes. Within the context of a Bravais lattice, the points that are in closest proximity to a given point are commonly denoted as its nearest neighbours. The quantity of nearest neighbours associated with a single point is formally known as the coordination number [40].

The complete solid can be replicated through the iterative translation of the primordial cell in three spatial dimensions. In order to facilitate geometric considerations, it is possible to select a larger pattern, referred to as a unit cell, as the fundamental constituent of the crystalline substance.

The unit cell is characterised by three lattice translation vectors, which are vectors that connect lattice points. The vectors that have a magnitude of one and are aligned with the axes, denoted as a, b, and c, are referred to as the primitive vectors. These vectors can be used as the edges of a unit cell. The unit cell undergoes translations by integral multiples of these vectors in order to create a lattice, allowing the lattice sites to be specified in terms of a translation vector **R** (Equation.1.1) [40].

$$\mathbf{R} = m_1\boldsymbol{a} + m_2\boldsymbol{b} + m_3\boldsymbol{c} \tag{1.1}$$

Where m_1,m_2,m_3 are the integers.

Figure 1.2 illustrates the unit cell that characterises the seven crystal systems and 14 Bravais lattices [40]. Additionally, Table 1.1 provides a comprehensive overview of the characteristics associated with both the crystal systems and Bravais lattices. The dimensions and configuration of the unit cell are determined by lattice parameters, also known as lattice constants, which encompass the lengths of the unit cell edges and the angles formed between the crystallographic axes.

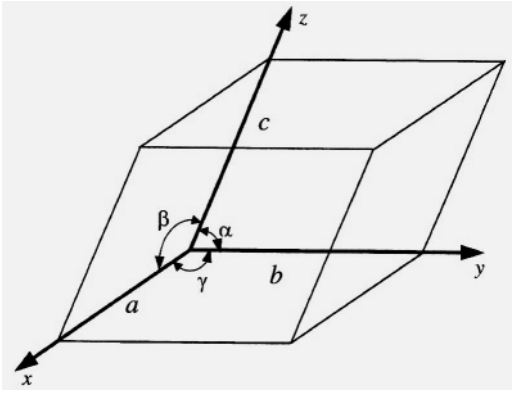

Figure 1.2 Cyrstallographic axes and lattice parameters [40]

The handling of crystal structures encompasses a significant consideration of symmetry features, namely the application of operations to fixed lattice points. The utilisation of various concepts, such as point symmetry, including reflection in a plane (commonly known as mirror symmetry), inversion symmetry, rotation axes, and rotation-inversion axes, proves to be valuable in comprehending and articulating the characteristics of crystalline materials. This is due to the fact that individual atoms or groups of atoms within the lattice possess distinct symmetry properties [41].

Table 1.1 Description of the seven crystal systems and 14 Bravais lattice [41].

Crystal system	The unit cell parameters	Bravais lattices
Cubic	$a=b=c$, $\alpha=\beta=\gamma=90°$	Simple, body-centered, face-centered
Tetragonal	$a=b\neq c$, $\alpha=\beta=\gamma=90°$	Simple, body-centered
Orthorombic	$a\neq b\neq c$, $\alpha=\beta=\gamma=90°$	Simple, body-centered, face-centered, base-centered
Trigonal (Rhombohedral)	$a=b=c$, $\alpha=\beta=\gamma\neq90°$	Simple
Hexagonal	$a=b\neq c$, $\alpha=\beta=90°$, $\gamma=120°$	Simple
Monoclinic	$a\neq b\neq c$, $\alpha=\beta=90°\neq\gamma$ or $\alpha=\gamma=90°\neq\beta$	Simple, base-centered
Triclinic	$a\neq b\neq c$, $\alpha\neq\beta\neq\gamma\neq90°$	Simple

The symmetry procedures under consideration encompass a transformation of coordinates. The mirror symmetry with respect to the yz-plane can be mathematically represented by the transformation equations y' = y, z' = z, and x' = -x [42,43].

In crystallography, the existence of a mirror plane in a crystal structure is conventionally indicated by the sign "**I**". The concept of inversion symmetry is mathematically expressed through the coordinate transformation x'=-x, y'=-y, z'=-z, and is commonly indicated by the symbol **I**.

The concept of rotational symmetry pertains to the occurrence of an identical structure when a specified angle of rotation is applied around a particular axis. On the other hand, a rotation-inversion symmetry axis denotes a rotation that is accompanied by a simultaneous inversion.

The assemblage of symmetry operations is commonly referred to as a point group. The space group of a crystal is defined by the combination of point group operations and translation symmetry, represented by a translation vector **R** [44].

The most basic form of a three-dimensional unit cell is the simple cubic unit cell, wherein an atom is located at each vertex of the cube. Two unit cells that exhibit a close relationship to the simple cubic cell are the body-centered cubic (BCC) unit cell and the face-centered cubic (FCC) unit cell.

The BCC crystal structure incorporates an atom positioned at the central point of the cube, while the FCC unit cell accommodates an atom on each face of the cube, in addition to the atoms located at each corner [45,46].

Certain semiconductors have the ability to undergo crystallisation in various configurations, which is contingent upon temperature or pressure conditions. This phenomenon gives rise to polymorphism and the coexistence of distinct polytypes. This thesis primarily focuses on the study of ZnO and TiO_2, with an emphasis on exploring their crystalline structures and key features.

Zinc oxide (ZnO) exhibits multiple crystalline structures, commonly referred to as polymorphs. There exist three recognised polymorphs of zinc oxide (ZnO): (i) wurtzite with a *P63/mc* space group, (ii) zinc blende with an *F43m* space group, and (iii) rocksalt with a *Fm/3m* space group. (Figure 1.3).

The crystal lattice of these formations exhibits varying configurations of zinc (Zn) cations and oxygen (O) anions, leading to discernible characteristics and behaviours [47,48].

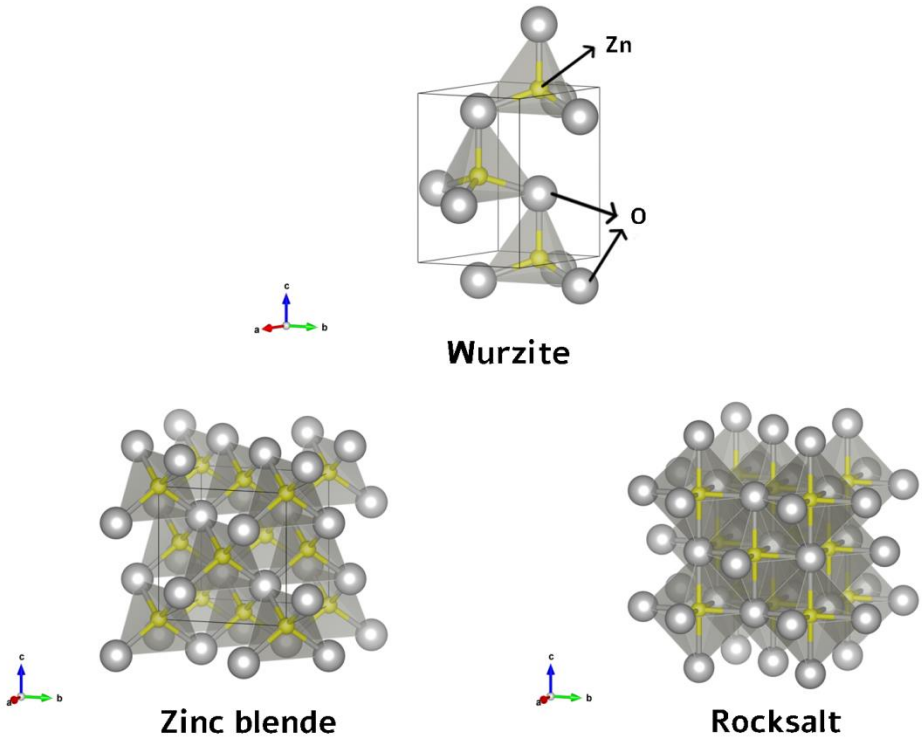

Figure 1.3 Three-dimensional representation of three different polymorphs of ZnO. The small yellow spheres represent the zinc atoms, the larger gray ones represent the oxygen atoms, and the gray tetrahedral shapes illustrate the orientation in space of the ZnO_4 tetrahedron.

Under ambient conditions, the Wurtzite structure exhibits higher thermodynamic stability. The ZnO compound has a wurtzite crystal structure, wherein each sublattice of the unit cell contains a total of four atoms. The zinc (Zn) atom in group 2 is coordinated by four oxygen (O) atoms in group 6, or vice versa.

In the case of Zinc Blende, it exhibits a cubic close-packed (face-centered) arrangement of oxygen (O) atoms, with the Zn (II) ions occupying tetrahedral spaces in the lattice. These tetrahedral sites are only half occupied, resulting in a unit cell containing 8 Zn atoms and 16 surrounding elements [49,50].

In the realm of TiO_2, rutile, anatase and brookite are usually accepted as three of the primary polymorphs, although brookite can also be observed. (Figure 1.4). Rutile is considered the thermodynamically stable phase, but both anatase and brookite are classified as metastable phases. The synthesis of brookite is very challenging, thereby limiting its frequency of study. Both rutile and anatase possess unique crystal structures that play a significant role in determining their individual properties and behaviours [51,52].

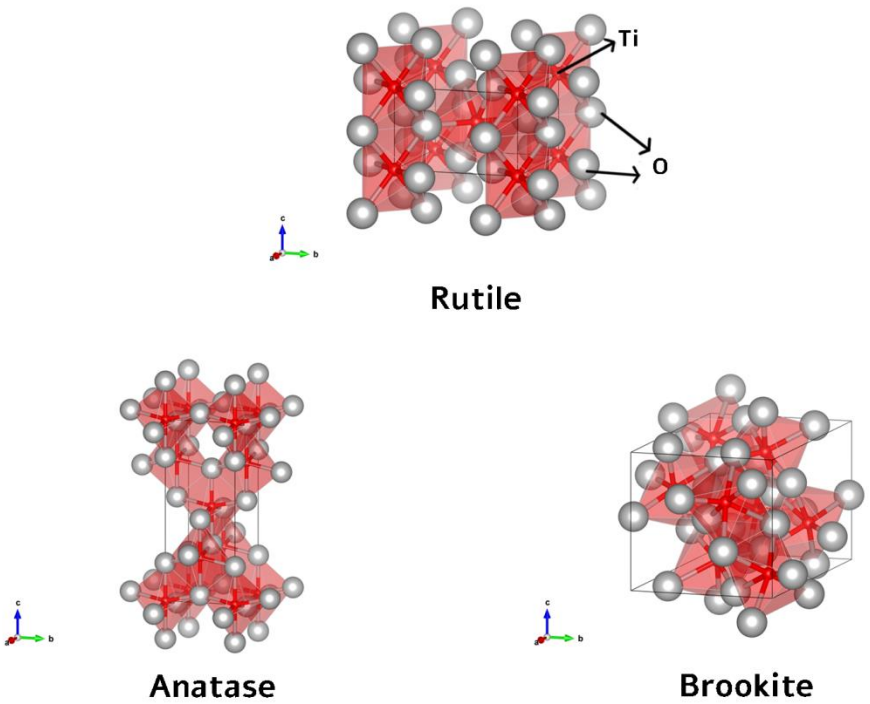

Figure 1.4 Three-dimensional representation of the three different polymorphs of the TiO_2. The small red spheres represent the titanium atoms, the larger gray ones represent the oxygen atoms, and the red octhaedral shapes illustrate the orientation in space of the TiO_6 octhaedron.

The Rutile exhibits a tetragonal crystal structure (*P42/mnm*) , characterised by a unit cell in the shape of a rectangular prism. This unit cell possesses three axis lengths that are not equal and accommodates two formula units of TiO_2. Within this particular arrangement, the titanium (Ti) cations demonstrate octahedral coordination, wherein they are surrounded by six oxygen (O) anions [53,54].

Conversely, each oxygen anion is encompassed by three titanium cations. The tetragonal crystal class imparts distinctive structural and physical features to rutile, setting it apart from anatase, and making it a unique crystalline form of TiO_2.

The Anatase structure possesses unique attributes, as it undergoes crystallisation in the tetragonal (*I41/amd*) crystal system. The unit cell of Anatase is a rectangular prism that accommodates four formula units of TiO_2 [55,56]. Regarding coordination, it can be observed that each Ti cation present in anatase exhibits octahedral coordination with six adjacent O anions. This particular characteristic is also observed in rutile. Nevertheless, there is a disparity in the atomic arrangement within the unit cell of the two structures [57,58].

Anatase exhibits reduced symmetry in comparison to rutile and is classified within the tetragonal or orthorhombic crystal systems, hence contributing to its distinctive structural and physical characteristics. Table.1.2 shown below presents a concise summary of the crystallographic properties exhibited by several polymorphs of TiO_2.

Table 1.2 Crystallographic properties of anatase and rutile

Property	Anatase	Rutile	Reference
Crystal structure	Tetragonal	Tetragonal	[59]
Atoms per unit cell (Z)	4	2	[59]
Space group	*I41/amd*	*P42/mnm*	[60]
Lattice parameters (nm)	a = 0.3785 c = 0.9514	a = 0.4594 c = 0.2958	[61]
Unit cell volume (nm^3)	0.1363	0.0624	[62]
Density ($kg\ m^{-3}$)	3894	4250	[63]

Defects, in a broad sense, encompass various forms of deviations from ideal crystal formations. Semiconductors, along with other solid-state materials, might potentially possess a range of faults that are incorporated into the material through processes like as growth and processing. At this point, it is advantageous to present overarching classification systems for problems.

There exists a distinction between two types of flaws: (i) structural defects and (ii) transitory defects. In the first scenario, the arrangement of atoms in actual crystals undergoes a permanent alteration, while temporary defects refer to elementary excitations such phonons, which are quanta of energy associated with lattice vibrations [64,65].

The categorization of structural defects encompasses various types, including point defects, one-dimensional or line defects, two-dimensional or planar defects, and three-dimensional or volume defects. Point defects involve substitutional and interstitial impurity atoms, vacancies, and other similar imperfections.

Line defects refer to one-dimensional defects like dislocations, while planar defects encompass two-dimensional imperfections such as surfaces, grain boundaries, and stacking faults. It is imperative to underscore that imperfections in actual materials have the potential to interact and give rise to a multitude of potential combinations [66].

It is noteworthy to acknowledge that flaws can also function as attracting centres for free electrons or holes. In the realm of defects, it is worth noting that only point defects possess the necessary low formation energies to be generated in thermal equilibrium. Furthermore, the quantity of point defects escalates in tandem with thermal activation.

Therefore, within a specific temperature range, crystal structures exhibit the existence of point defects, namely vacancies and interstitials. Additional imperfections associated with increased dimensionality, such as dislocations, manifest themselves during the growth and/or processing stages of semiconductor materials [67,68].

These faults have the potential to result in device failure, making them a significant problem in terms of reliability.

In certain instances, it is possible for a fault to not impede the initial functioning of a device, but rather manifest throughout extended periods of operation, ultimately resulting in device failure.It is imperative to reiterate the importance of reducing fault densities to sufficiently low levels that do not have an impact on semiconductor characteristics or device performance.

The figure 1.5 illustrates simple native (or intrinsic) point defects, which encompass a vacancy [69], representing a vacant site within the lattice, and an interstitial, which refers to an atom placed into a space located between the crystal structure sites [70].

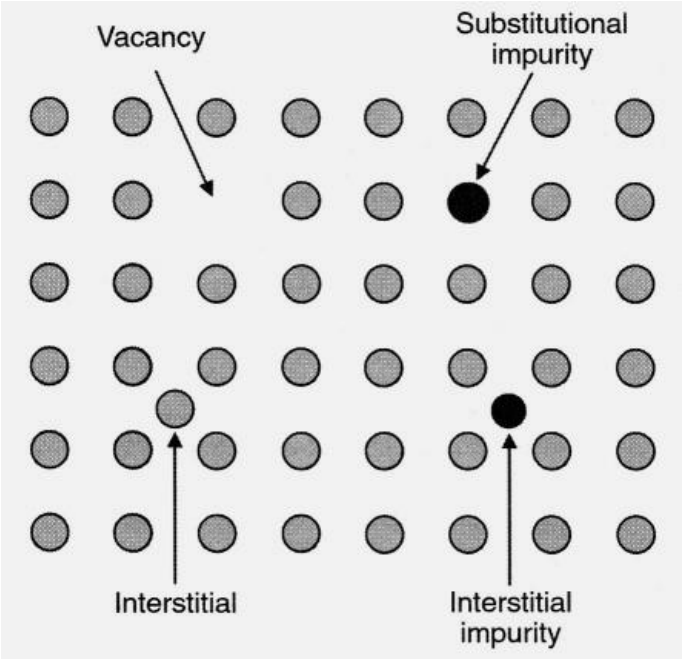

Figure 1.5 Native and foreign point defects in materials.To maintain simplicity, the distortion of the lattice surrounding these faults has been omitted from the depiction.

It is important to acknowledge that, despite its absence in Figure 1.5, the crystal experiences localised zones of distortion as a result of these imperfections. This occurs because the surrounding atoms in the lattice must adjust to accommodate these defects.

A Schottky defect refers to a vacant site within the lattice structure. In this scenario, the atom that should occupy the site has either relocated from the interior to the surface of the crystal or become imprisoned at an extended defect, such as a dislocation [71]. A Frenkel defect is the term used to describe a vacancy that is coupled with an interstitial atom, forming a vacancy-interstitial pair.

It is important to acknowledge that the quantity of these flaws not only increases in bigger quantities with rising temperature in thermal equilibrium but can also be elevated by nonequilibrium mechanisms such as displacement of atoms caused by high-energy electron or nuclear particle bombardment [72,73].

Clusters of point defects, such as a pair of vacancies or precipitates consisting of impurity atoms, can also occur in some instances. The phenomenon of vacancies in solids can provide insight into the process of atom diffusion inside the material, as atoms can travel towards vacancies, leading to the migration of vacancies in the opposite direction. Atomic diffusion can also take place when atoms or ions undergo a transition in their interstitial locations [74].

The expression for the equilibrium density of vacancies in a crystal (Equation.1.2), which consists of N atoms per unit volume at a temperature T, is denoted as Nv.

$$N_v \cong N e^{\frac{-E_v}{k_B T}} \tag{1.2}$$

The value of N_v is determined by the energy of production of a vacancy, E_v, which is normally around 1 electron volt (eV). It is important to acknowledge that inside compound crystals (AB), the occurrence of an antisite defect is possible when an atom A occupies an atom B site, or vice versa [74].

Dislocations are flaws of considerable significance, as they exert a substantial and frequently detrimental influence on the electrical and optical characteristics of semiconductors [75].

Furthermore, dislocations exhibit significant interactions with other defects, hence resulting in the creation of these defects. There are two primary forms of dislocation in materials: an edge dislocation and a screw dislocation (see to Figure 1.6). An edge dislocation is characterised by the presence of an additional plane inserted along the edge of a crystal, while a screw dislocation induces a helical distortion within the crystal.

The influence of dislocations, including their type and distribution, on numerous properties of crystalline semiconductors is well-documented. These aspects encompass crystal development, mechanical strength, and electrical characteristics [76,77].

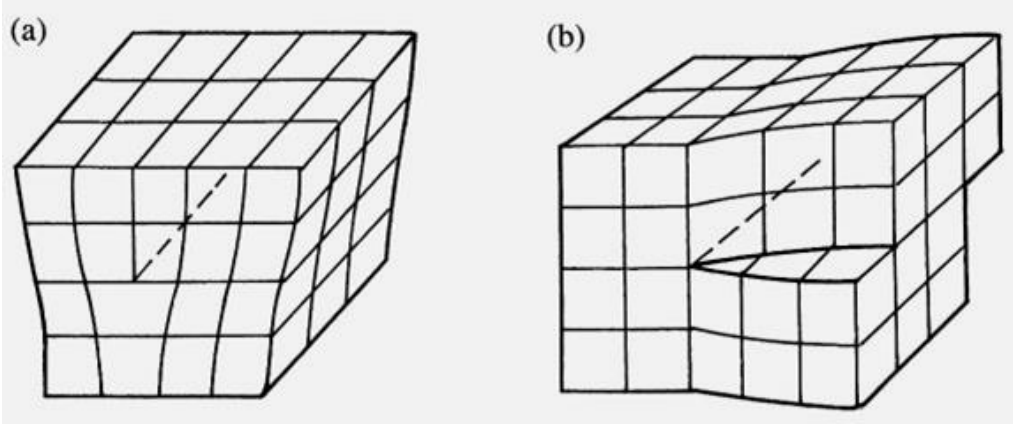

Figure 1.6 Ilustration of an edge dislocation (a) and a screw dislocation (b).

Dislocations can arise by the aggregation of point defects at an atomic plane, or they can be generated when stress induces the slipping of atomic planes past each other at elevated temperatures during growth or processing. Dislocations are not observed in thermodynamic equilibrium due to their significant energy levels, leading to the production of massive dislocation-free crystals such as silicon (Si) [78].

Surface defects encompass two types: (i) free surfaces, which are universally present in all materials, and (ii) unintentionally produced interfaces, in contrast to deliberately formed interfaces like p-n junctions and contacts [79,80].

The grain boundary is commonly regarded as a two-dimensional imperfection; however, it should be noted that this defect possesses a distinct thickness in actuality. Typically, grain borders exhibit a significant concentration of interface states which possess the ability to capture free carriers, induce carrier scattering, and serve as sites for impurity segregation.

A volume defect refers to any deviation in volume inside a semiconductor that exhibits variations in composition, structure, and/or orientation compared to the surrounding crystal. Volume defects are generated through the aggregation of vacancy clusters, which can undergo growth and subsequent collapse, resulting in the formation of dislocation loops [81].

Certain impurities have the potential to undergo precipitation, resulting in the formation of a distinct phase. Additionally, impurity atoms and vacancies have the propensity to combine and create enormous three-dimensional structures.

The existence of imperfections in semiconductors can result in two significant consequences. Firstly, it can introduce energy levels within the energy gap, hence influencing the electrical characteristics of the material. Secondly, it can lead to a decrease in carrier mobility due to an elevated amount of scattering caused by these defects [82,83].

The transport capabilities of semiconductors are contingent upon the existence of diverse imperfections that function as scatterers of carriers. The effects observed in this context exhibit variations based on temperature, resulting in a non-linear relationship between electrical conductivity and temperature. This can be attributed to the distinct temperature dependencies of defect concentration and electrical activity [84].

As previously stated, not all departures from a perfect crystal structure have negative consequences. Certain faults are intentionally generated in order to create materials and gadgets that possess specific desirable qualities. The subsequent chapters will go into the examination of n- and p-type doped areas as well as epitaxial multilayers found in diverse devices. To restate, the presence of impurity atoms within crystals is classified as point defects when they hinder the effective use of the material or device [85,86].

However, if these impurity atoms are intentionally introduced into the material to regulate conductivity or optical properties, they are referred to as donors, acceptors, and recombination centres. Furthermore, it is crucial to highlight that even minute quantities of impurity atoms can have a profound impact on the electrical characteristics of a semiconductor.

Hence, in the realm of semiconductors, it is of utmost importance to effectively regulate the presence of inadvertent dopant atoms, ensuring that their concentration remains below thresholds that could adversely impact the operation of electronic devices.

Currently, the level of compositional purity of silicon (Si) is such that the concentration of undesirable impurities is below one part per billion (ppb), meaning that there is less than one impurity atom for every billion silicon atoms [87].

It is important to acknowledge that the deliberate addition of dopant atoms to a semiconductor material is necessary for the purpose of regulating its electrical properties.

This process typically involves introducing dopant atoms within a range that spans from one dopant atom per 100 million semiconductor atoms to one dopant atom per thousand semiconductor atoms [88].

1.2.2. Band Theory of Solids for Semiconductor Oxides

The differentiation between metals, semiconductors, and insulators can be elucidated by examining the electronic band structure of solids, as depicted in Figure 1.7. Firstly, it is important to highlight that energy bands devoid of electrons, commonly referred to as empty energy bands, do not make any contribution to the electrical conductivity of a material. Conversely, completely filled bands that contain electrons also do not contribute to electrical conductivity [89,90].

This is because the carriers within these bands are unable to acquire additional energy, even when an electric field is applied, as all the energy levels within the bands are already occupied.When comparing, it can be observed that the partially filled bands encompass both electrons and vacant energy levels that exist at elevated energy states. The latter phenomenon enables carriers to acquire energy when subjected to an externally applied electric field.

Consequently, carriers inside a partially occupied band can make a significant contribution to the overall electrical conductivity of the material. In the context of metallic materials, the electronic band structure gives rise to a situation where the highest energy band is not completely filled [91].

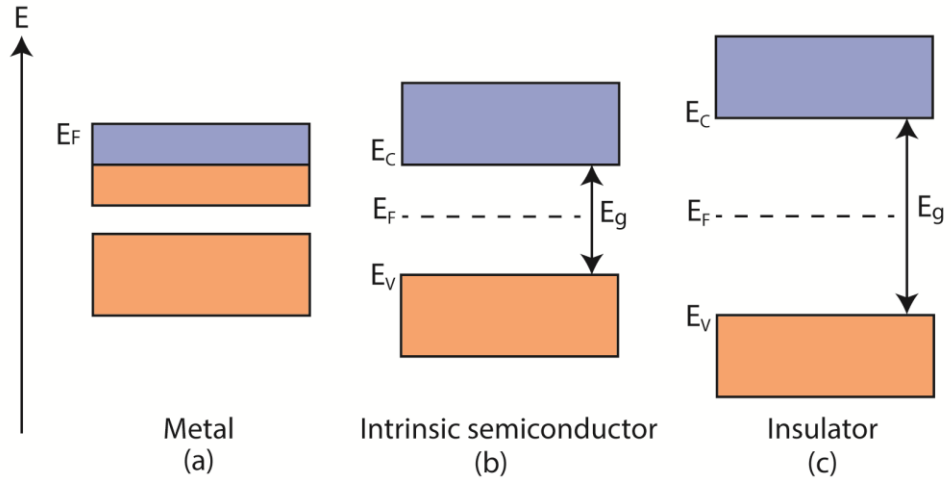

Figure 1.7 Schematic illustration depicting the typical band diagrams for three distinct materials: (a) a metal, (b) an intrinsic semiconductor at absolute zero temperature (T=0 K), and (c) an insulator. The Fermi level is symbolised by dashed lines. The sections that appear purple in the visual representation indicate the presence of filled bands, whereas the orange portions correlate to the absence of bands.

The distinguishing characteristic between a semiconductor and an insulator is in the magnitude of the energy gap that separates the highest filled band, also known as the valence band, and the lowest empty band, referred to as the conduction band.

In the context of an intrinsic semiconductor, the valence band, which is the highest occupied band, is distinctly separated from the conduction band, which is the lowest unoccupied band, by a relatively narrow energy gap that is disallowed for electron transitions. At a temperature of absolute zero (T = 0 K), the conduction band is devoid of any electrons.

In the context of semiconductors, it is observed that the energy gap (E_g) is quite small. As a result, at normal room temperature, the electrons located at the uppermost energy level of the valence band are stimulated by thermal energy and transition to the conduction band [91].

This transition enables these electrons to participate in the transportation of charge carriers inside the material. In the context of insulators, it is observed that the energy gap is significantly larger in comparison to semiconductors. Consequently, at normal room temperature, the likelihood of thermal excitation causing an electron to transition from the valence band to the conduction band is considerably diminished.

Figure 1.7 illustrates the concept of the Fermi energy, also known as the Fermi level (E_f), which serves as the baseline energy for determining the likelihood of electron states being occupied. Therefore, in the case of metals, the Fermi energy (E_f) is situated within a partially occupied permitted band, as illustrated in Figure 1.7. Conversely, in semiconductors and insulators, it is positioned within the prohibited band.

At this moment, it is imperative to establish an extra parameter that proves to be valuable in the characterization of semiconductors (refer to Figure 1.8). The electron affinity, denoted as eχ, is a measure of the energy difference between the vacuum level, which represents the energy of a free electron, and the lowest energy level in the conduction band [92].

Another crucial component to consider is the work function (often represented as Φ), which represents the energy disparity between the vacuum level and the Fermi level. It is important to acknowledge that the electron affinity (eχ,) remains constant for a specific semiconductor, whereas the work function (Φ) is contingent upon the doping level, hence influencing the position of the Fermi level [92].

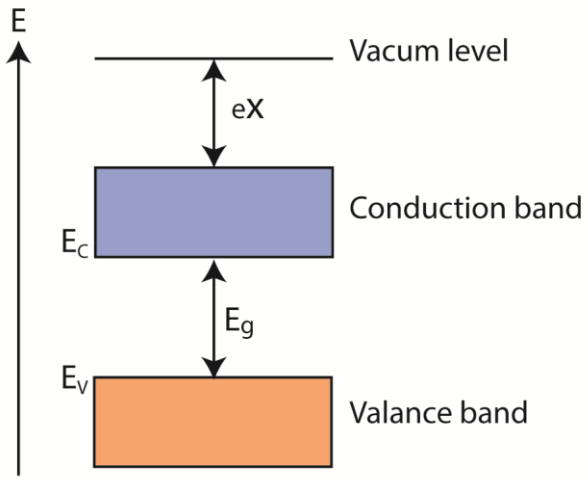

Figure 1.7 A schematic representation of a standard band diagram, which serves to elucidate key concepts relevant to the characterization of a semiconductor. Specifically, this diagram encompasses the electron affinity (eχ), denoting the disparity in energy levels between the vacuum level and the lowermost point of the conduction band.

1.2.3. Optical aborption in Semiconductor Oxides

In the context of electronic transitions (refer to Figure 1.9), the principles of energy and momentum conservation ($\hbar k$) are crucial, where k is the value of the wave vector. A direct-gap semiconductor is characterised by the occurrence of direct (or vertical) transitions when the minimum of the conduction band and the maximum of the valence band coincide at a specific value of the wave vector k [92].

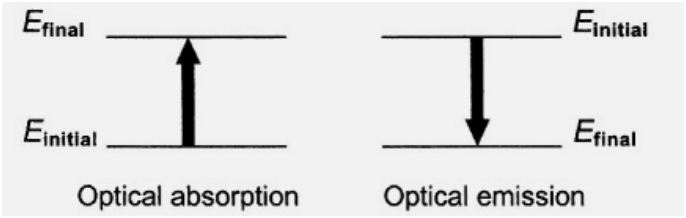

Figure 1.9 Schematic illustration of the optical absorption and emission processes, with the arrows denoting the electronic transitions [92].

In the context of optical emission, the predominant transitions in semiconductors occur between the states with the highest probability of being occupied at the minimum of the conduction band and the ones with the highest probability of being unoccupied at the maximum of the valence band [93].

In the case where the band extrema do not manifest at identical wave vector k, the resulting transitions are classified as indirect, hence characterising the material as an indirect-gap semiconductor. In order to uphold momentum conservation in semiconductors, the involvement of an additional particle, specifically a phonon, is necessary.

However, it is important to note that the likelihood of this process occurring is significantly smaller when compared to direct transitions.Broadly speaking, there are multiple optical absorption mechanisms, each of which adds to the overall absorption coefficient (α). The mechanisms encompassed in this study consist of (i) the fundamental absorption process, (ii) exciton absorption, (iii) absorption resulting from dopants and defects, (iv) absorption arising from intraband transitions, and (v) free carrier absorption [92,93].

The absorption mechanism observed at photon energies exceeding the energy gap is attributed to the movement of electrons from occupied valence band states to unoccupied conduction band states. At energy levels that are somewhat lower than the energy gap, the absorption process can be attributed to the presence of excitons and the transitions occurring between impurity states and band states.

These transitions involve movements from acceptor states to the conduction band and from the valence band to donor states. The absorption continuum at lower energies arises from free carrier absorption caused by transitions occurring inside the energy bands. The subsequent sections provide a detailed explanation of these absorption methods [94,95].

During the process of fundamental absorption, an incident photon induces the excitation of an electron from the valence band to the conduction band. The conservation of both energy and momentum is a fundamental need in this particular process.

Given that the momentum of a photon is significantly smaller than the momentum of a crystal, it can be inferred that the absorption process mostly preserves the momentum of the electron.

As previously mentioned, in cases when the minimum of the conduction band and the maximum of the valence band coincide at a specific wave vector k, the resulting transitions are classified as direct, leading to the designation of the material as a direct-gap semiconductor.

In the event that the band extrema do not manifest at identical wave vector k, the resulting transitions are classified as indirect, hence categorising the material as an indirect-gap semiconductor.

In order to uphold momentum conservation in semiconductors, an additional particle, specifically a phonon, must be involved. However, the likelihood of this process occurring is significantly smaller when compared to direct transitions.

Hence, it can be observed that the fundamental absorption in indirect-gap semiconductors has substantially diminished strength in comparison to direct-gap materials.

The phenomenon of optical absorption can be characterised by the absorption coefficient (α), which can be determined by the analysis of transmission data.

Given an incident light intensity denoted as I_0, the transmitted light intensity as I, and the reflectivity as R, the transmission, denoted as $T = \frac{I}{I_0}$, can be expressed as Equation.1.3-1.5, assuming interference is neglected [92].

$$T = \frac{(1-R)^2 \exp(-\alpha d)}{1-R^2(-2\alpha d)} \tag{1.3}$$

where d is the thickness of the material. For large αd this expression can be reduced to

$$T = (1-R)^2 \exp(-\alpha d) \tag{1.4}$$

and, in the absence of reflection, it can be further reduced to

$$I = I_0 \exp(-\alpha d) \tag{1.5}$$

The absorption coefficient (α) (Equation 1.6) can be expressed as

$$\alpha(h\nu) = A \sum P_{if} n_i n_f \tag{1.6}$$

where P_{if} is the transition probability, n_i and n_f are the densities of the electrons in the initial state and of empty energy levels in the final state, respectively, and the sum is over all initial and final states.

Thus, for direct transitions between parabolic valence and conduction bands, the absorption coefficient is

$$\alpha(h\nu) = A(h\nu - E_g)^{\frac{1}{2}} \quad (1.7)$$

where A is a constant the energy gap, E_g and $h\nu$ are in eV, and α is in cm^{-1}.

It is important to acknowledge that in numerous semiconductors, including both crystalline and amorphous forms, the absorption coefficient within the absorption edge region has been observed empirically to obey Urbach's rule (Equation 1.8):

$$\alpha(h\nu) = \alpha_0 \exp[g(h\nu - h\nu_0) \quad (1.8)$$

where the coefficient g is a temperature-dependent parameter for ionic crystals, whereas for covalent semiconductors g depends on the concentrations and the electrical charges of impurities.

In materials with an indirect band gap, the valence band's highest energy and the conduction band's minimum energy do not coincide at the same wave vector k. In instances of conservation of energy and momentum, transitions occur with the involvement of three particles, namely photons, electrons, and phonons. In contrast to photons, phonons possess relatively high momentum despite their modest energy.

Therefore, in the context of indirect transitions, the principle of momentum conservation is upheld through the process of either absorbing or emitting a phonon possessing a distinct energy value denoted as E_p.

The absorption coefficient pertaining to a transition that involves phonon absorption can be expressed as (Equation 1.9):

$$\alpha_a(h\nu) = \frac{A(h\nu - E_g + E_p)^2}{\exp\left(\frac{E_p}{k_{BT}}\right) - 1} \tag{1.9}$$

And the absorption coefficient for a transition involving phonon emission is given by Equation 1.10.

$$\alpha_e(h\nu) = \frac{A(h\nu - E_g - E_p)^2}{1 - \exp\left(-\frac{E_p}{k_{BT}}\right)} \tag{1.10}$$

It is important to observe that the denominator term in these equations exhibits a correlation with the quantity of phonons, as dictated by the principles of Bose-Einstein statistics (Equation 1.11).

$$n_{phonons}\left[exp\left(\frac{E_p}{k_{BT}}\right) - 1\right]^{-1} \tag{1.11}$$

Both phonon absorption and emission processes can occur when the energy of the incident photon (hν) is greater than the sum of the energy bandgap(E_g) and the phonon energy (E_p). Consequently, the absorption coefficient can be expressed as such (Equation 1.12):

$$\alpha(h\nu) = \alpha_a(h\nu) + \alpha_e(h\nu) \tag{1.12}$$

The absorption mechanism in indirect-gap materials necessitates the participation of an additional particle, specifically a phonon, in contrast to direct-gap materials. Therefore, the likelihood of light absorption, and consequently the absorption coefficient, is significantly reduced in this scenario compared to direct-gap materials.

This suggests that light must traverse a significant distance within the material prior to undergoing absorption. In the vicinity of the absorption edge, the absorption coefficient (α) exhibits a range of values for direct transitions, whereas for indirect transitions, it can span from 10 to 10^3 [96].

1.2.4. Recombination Process

Within the realm of semiconductors, the occurrence of different types of excitations, such as photon or electron irradiation, has the potential to result in the production of charge carriers that surpass the densities observed under thermal equilibrium conditions.

The equilibrium is restored through the recombination of electron-hole pairs. Recombination centres that possess energy levels inside the bandgap of a semiconductor can be classified into two categories: radiative and nonradiative. The distinction between these categories is based on whether the recombination process leads to the emission of a photon (radiative) or not (nonradiative) [92].

The utilisation of semiconductors in the context of luminescence is a significant area of application, wherein the recombination processes assume a pivotal role.

When a semiconductor is subjected to a specific type of energy input, it has the potential to release photons that surpass the amount of thermal radiation [97].

The luminescence process can be classified into three categories based on the source of excitation of the luminescent material: photoluminescence (excitation by photons), electroluminescence (excitation through the application of an electric field), and cathodoluminescence (excitation by cathode rays or energetic electrons).

The phenomenon of luminescence in semiconductors is commonly explained by the process of radiative recombination between electron-hole pairs. This recombination can occur between states in either the conduction or valence bands, as well as states inside the energy gap caused by the presence of donors and acceptors.

In the context of semiconductors, the occurrence of photon emission takes place within the visible region of the electromagnetic spectrum when the energy gap possesses suitable values (0.4 and 0.7 μm, corresponding to about 3.1 and 1.8 eV) [98,99].

Semiconductors possess highly desirable qualities that render them highly appealing for a wide range of optoelectronic applications. Additionally, the utilisation of luminescence measuring techniques proves to be an effective and influential tool for the comprehensive analysis and evaluation of the electrical properties exhibited by semiconductors.

The phenomenon of luminescence in semiconductors arises from the occurrence of electronic transitions between quantum mechanical states, often characterised by energy differences ranging from slightly below 1 electron-volt (eV) to several electron-volts (eV).

The luminescence spectra can be categorised into two main types: intrinsic, also known as fundamental or edge emission, and extrinsic, often referred to as characteristic or activated emission [100].

The phenomenon of intrinsic luminescence arises from the recombination of electrons and holes across the energy gap, signifying its inherent nature within the material. At ambient temperatures, intrinsic luminescence appears as a band of energies with its intensity peak at a photon energy $(h\nu_p \cong E_g)$. Hence, the measurement of any alteration in the energy gap, such as those caused by variations in temperature or high levels of doping, enables monitoring $h\nu_p$.

As previously mentioned, in direct-gap semiconductors such as GaAs and CdS, the predominant transitions occur directly across the minimum energy gap.

These transitions involve the most probable movement of electrons from the most filled states located at the minimum of the conduction band to the states that are most likely to be unoccupied at the maximum of the valence band.

The occurrence of radiative recombination between electrons and holes is highly probable in the aforementioned transitions. In the case of indirect-gap semiconductors, such as silicon (Si) and gallium phosphide (GaP), the recombination of electron-hole pairs necessitates the involvement of an additional particle known as a phonon [100].

Consequently, the likelihood of this recombination process occurring is considerably diminished as compared to direct transitions. Hence, the primary emission in indirect-gap semiconductors is relatively feeble, particularly when juxtaposed with emissions caused by impurities or defects. The emission spectra observed in both direct-gap and indirect-gap semiconductors are considered extrinsic in nature due to their dependence on the presence of different impurities.

1.3. Synthesis methods of oxide semiconductors

1.3.1. Sol–gel Method

The sol-gel process can be broadly defined as the chemical transformation of a precursor solution into an inorganic solid. Typically, the inorganic precursor employed in this context is either an inorganic metal salt or a metal organic species, such as a metal alkoxide or acetylacetonate.

Metal alkoxides are commonly employed as precursors in aquatic environments, and their conversion into the oxidic network is achieved through hydrolysis and condensation processes [101–103].

In the context of aqueous sol-gel processes, the oxygen required for the synthesis of the oxidic chemical is sourced from the water molecules. In the case of non-aqueous sol-gel systems, the absence of water hinders the availability of oxygen necessary for the synthesis of metal oxide. According to reports, the formation of metal oxide nanoparticles follows a similar non-hydrolytic preparation method as that used for bulk metal oxide formation [103–105].

In this process, the oxygen required for nanoparticle formation is supplied by the solvent, which can be ethers, alcohols, ketones, or aldehydes, or by the organic component of the precursor, such as alkoxides or acetylacetonates. For instance, previous studies have employed titanium isopropoxide and titanium chloride as precursor materials in order to synthesise anatase nanocrystals.

The process of ether elimination had significant importance in the formation of the M–O–M bond. The reaction proceeds by a mechanism involving the condensation of two metal alkoxides via an elimination process [106–108].

The Ester elimination process is a chemical reaction that occurs between metal carboxylates and metal alkoxides. This reaction has been shown to produce zinc oxide, titania, and indium oxide.

The reaction between metal oleates and amines bears resemblance to ester eliminations, namely in the context of the controlled synthesis of titania nanorods [109].

Nevertheless, the use of ketones as solvents typically leads to the liberation of oxygen by aldol condensation. This process involves the reaction between two carbonyl compounds, resulting in the elimination of water. The water molecules released during this reaction serve as the agent responsible for supplying oxygen during the creation of metal oxide. The synthesis of ZnO and TiO_2 has been reported utilising acetone as a solvent [110,111].

1.4. Synthesis methods of thin films

A thin film is a layer of material that has a thickness on the order of nanometers (nm) to micrometers (μm). Thin films find extensive utilisation in diverse industries such as electronics, optics, coatings, and other related sectors [112].

Thin film deposition techniques comprise a diverse range of methodologies employed for the purpose of fabricating thin layers of material onto substrates.

The utilisation of these approaches has significant importance across diverse industries such as electronics, optics, and materials research, wherein the precise management of film thickness and characteristics is of utmost significance [113].

Some of the best known techniques for final layer deposition are shown in figure 1.10. Physical Vapor Deposition (PVD), in which we can find the following variables: Sputtering, Thermal Evaporation, Electron Beam Evaporation and Pulsed Laser Deposition (PLD) [114].

Within the deposition techniques we can also find Chemical Vapor Deposition (CVD), also with its different variants such as: Sputtering, Thermal Evaporation, Electron Beam Evaporation and Pulsed Laser Deposition (PLD): Low-Pressure Chemical Vapor Deposition (LPCVD), Metal-Organic Chemical Vapor Deposition (MOCVD), Atomic Layer Deposition (ALD).

Other variants of these techniques are Chemical Solution Deposition (CSD), Sol-Gel Process, Spray Deposition or Pulsed Laser Ablation (PLA).

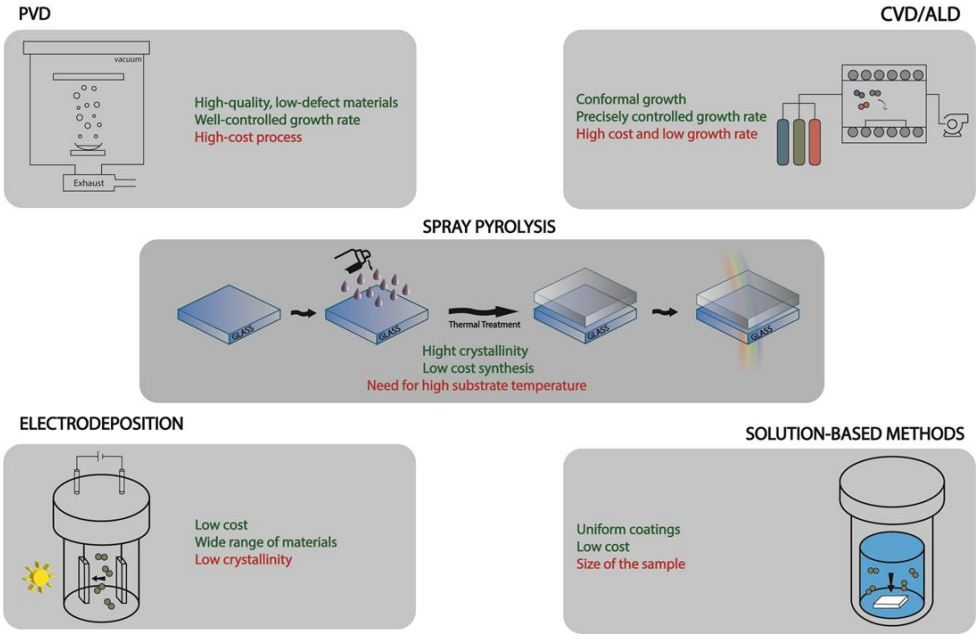

Figure 1.10 Scheme of the most prevalent thin film deposition techniques

Each of these deposition processes presents distinct advantages and is selected depending on the specific demands of the thin film and its intended application.

The selection of the most suitable approach is determined by researchers and engineers, who take into consideration several criteria like the composition of the material, the thickness of the film, its uniformity, and the compatibility with the substrate.

In this section, the methods of thin film synthesis will be explained in general terms, with emphasis on the spray pyrolysis method, which has been the most widely used during this thesis.

1.4.1. Spray pyrolysis

Various techniques are used for the deposition of thin films, each with its own advantages and disadvantages. However, spray pyrolysis is gaining popularity due to its simplicity and versatility.

Spray pyrolysis techniques involve the acceleration of a liquid or liquid/solid phase precursor solution from a specially designed atomizing nozzle (atomizer) in order to transport a droplet of reagents to a surface or interface. The classification of atomizers is dependent on a number of parameters.

We based the respective methodologies on four classes of atomizers powered by distinct energy sources: liquid-and-gas energy, mechanical energy, vibrational energy, and electrical energy [115].

This technique involves the atomization of a precursor solution or suspension, which is then sprayed onto a heated substrate to form a thin film as shown in Figure. 1.11.

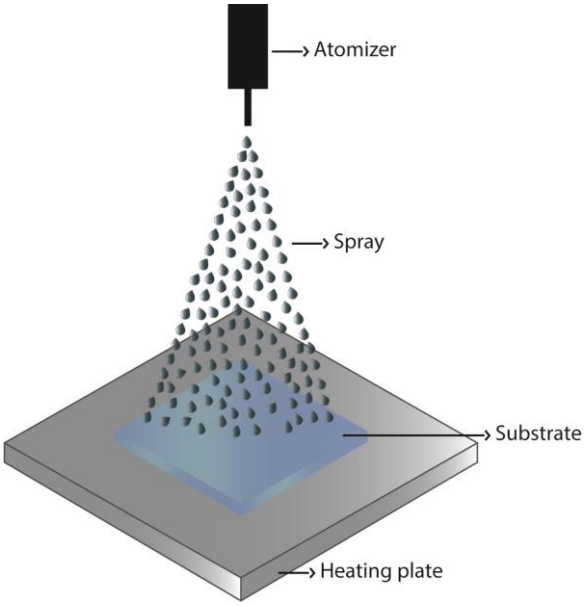

Figure 1.11 Diagrammatic illustration of the spray pyrolysis set up

Spray pyrolysis entails a variety of simultaneous or sequential processes. Aerosol generation and transport, solvent evaporation, droplet impact with successive spreading, and precursor decomposition are the most essential of these processes. Except for the production of aerosols, the deposition temperature is implicated in all processes listed.

Consequently, the substrate's surface temperature is the most influential factor in determining the morphology and properties of the film. By increasing the temperature, the microstructure of the film can transform from fractured to porous. In numerous investigations, the deposition temperature was cited as the most crucial spray pyrolysis variable [116,117].

Spray pyrolysis offers several advantages over other methods, such as its compatibility with large-area deposition and the ability to control the properties of the thin film by adjusting the precursor concentration and deposition temperature [117,118].

In numerous investigations, the deposition temperature was cited as the most crucial spray pyrolysis variable. Additionally, it is relatively inexpensive and easily scalable for industrial production. Spray pyrolysis has been used to deposit a wide range of materials, including metal oxides for electronic and optical applications, as well as thin films for energy conversion and storage applications [119] .

Therefore, this technique is a promising tool for researchers and engineers in various fields for the generation of thin films with tailored properties. To acquire a thin film with the desired properties using spray pyrolysis and deposition, it is necessary to consider a number of crucial parameters.

These parameters are affected by the used material and the desired thin film properties. The concentration of the precursor solution or suspension is a crucial parameter since it influences the quality and thickness of the thin film [120].

In addition, the type and parameters of the discharge nozzle, such as the particle size and shape, affect the uniformity and morphology of the thin film.

Additionally, the gas flow rate plays an important role in the transport of precursor particles to the substrate and can affect the uniformity and thickness of the thin film.

In addition to affecting the thickness of the thin film, the deposition time can influence its morphology and crystal structure.

Lastly, post-deposition annealing can improve the crystallinity and electrical properties of the thin film. Optimising these parameters is necessary to achieve the desired properties of the thin film and to guarantee the reproducibility of the results [121].

1.4.2. Physical Vapor Deposition (PVD)

The process of Physical Vapor Deposition (PVD), also known as thin film deposition, involves the deposition of material in the form of atoms or molecules by vaporizing it from a solid or liquid source.

This vapor is transported through a vacuum or low pressure gaseous or plasma environment to the substrate where it is deposited. PVD is performed using two primary techniques, namely sputtering and evaporation.

Sputtering can be accomplished through various methods such as Direct Current (DC), Radio Frequency (RF), and Ion Beam sputtering [122,123].

On the other hand, the evaporation process involves resistive heating, flash evaporation, and e-beam evaporation among other techniques PVD is typically used to create films with thicknesses ranging from a few nanometers to thousands of nanometers, as well as multilayer coatings, graded composition deposits, and freestanding structures [124].

The size and shape of the substrate can vary greatly, from small watchbands to large architectural glass panels. The typical deposition rate for PVD processes is between 10-100 Å (1-10 nanometers) per second. PVD can be used to deposit films of elements, alloys, and compounds using reactive deposition processes.

Reactive deposition processes involve the formation of compounds through the reaction of the depositing material with the ambient gas environment or with a co-depositing material [125,126].

Quasi-reactive deposition involves the deposition of compound materials from a compound source where the loss of volatile or less reactive species is compensated for by having a partial pressure of reactive gas in the deposition environment, such as the quasi-reactive sputter deposition of ITO (indium-tin-oxide) using a partial pressure of oxygen in the plasma [127].

1.4.3. Chemical Vapor Deposition (CVD)

Chemical vapor deposition (CVD) and physical vapor deposition (PVD) differ primarily in their use of chemical precursors or reactions during the deposition process. Chemical deposition can be divided into subcategories depending on the deposition medium [128,129].

CVD or atomic layer deposition (ALD) are used for deposition primarily through vapor-phase processes. Organometallic compounds are commonly used as precursors due to their volatility. The key difference between CVD and ALD is that the latter relies on self-limiting surface chemical reactions.

CVD is commonly used for synthesizing thin film semiconductors, including metal oxides. The latest advancement in chemical vapor deposition involves combining this technique with other types of treatments, such as plasma treatments, or more cost-effective production methods like mist CVD [130,131].

Mist CVD entails atomizing a precursor solution into a mist using ultrasonic vibrations, which is then supplied to the substrate using a carrier gas. The precursor mist is thermally decomposed, leading to the formation of a film on the substrate [132]. The absence of a vacuum system in this process enables the production of films that are both highly productive and low-cost . The example chosen in this case is ZnO nanotubes deposited on glass using the CVD technique [133].

1.4.4. Atomic Layer Deposition (ALD)

Atomic Layer Deposition (ALD) is a process used for the synthesis of oxide thin films with precise control over the thickness and composition of the deposited material.

The ALD process involves the sequential deposition of atomic layers onto a substrate surface through self-limiting surface reactions [134]. The process typically involves four steps: preparation of the substrate, deposition of the first precursor, purge, and deposition of the second precursor.

During the deposition of the first precursor, a single atomic layer is deposited onto the substrate surface through self-limiting reactions [135]. The process is then repeated with the deposition of the second precursor to form a second atomic layer on top of the first one.

The process can be repeated multiple times to deposit a desired number of atomic layers . The ALD process allows for precise control over the thickness and composition of the deposited thin film, as the deposition of each atomic layer can be precisely controlled.

The process can also be used to deposit a wide range of materials, including metals, metal oxides, and nitrides, making it a versatile technique for thin film synthesis [136,137]. Overall, ALD is a valuable technique for creating thin films with uniform thickness, conformal coating, and excellent control over the film properties.

Atomic Layer Deposition (ALD) and Physical Vapor Deposition (PVD) are both widely used techniques for the synthesis of thin films. However, they differ in their mechanism of operation, their advantages, and their limitations.In ALD, the deposition of the material occurs through self-limiting surface reactions, resulting in precise control over the thickness and composition of the deposited film [138].

On the other hand, PVD involves the deposition of material in the form of vapor, which condenses onto the substrate surface. PVD can be carried out using several techniques, including evaporation and sputtering, resulting in a variety of film properties.

One advantage of ALD over PVD is its ability to deposit highly conformal coatings with uniform thickness and excellent control over the film properties [139].

In contrast, PVD can suffer from poor conformality and thickness control, leading to non-uniform coatings. However, PVD is generally a faster process than ALD, making it a more suitable option for industrial-scale production [140].

ALD is also capable of depositing a wide range of materials, including metals, metal oxides, and nitrides, with precise control over their composition. In contrast, PVD is limited to materials that can be evaporated or sputtered, which can be a disadvantage for some applications [141].

Overall, both ALD and PVD are valuable techniques for the synthesis of thin films, with their unique advantages and limitations. The choice between the two techniques depends on the specific requirements of the application, such as the desired film properties, the material to be deposited, and the production scale.

1.4.5. Electrodeposition

Electrodeposition is gaining popularity as a technique for the synthesis of semiconductor thin films and nanostructures, particularly chalcogenides and oxides. The electrodeposition can proceed cathodically or anodically, beginning with dissolved precursors (mostly ions).

For cathodic (anodic) processes, the reaction should proceed when the applied potential is less than (greater than) the redox potential of the reaction [142,143]. The schematic of the electrodeposition process is shown in figure 1.12 [143].

When compound semiconductors must be deposited, the reaction requires soluble precursors of all elements (2, 3 or more). Notably, the precursors for As, Te, and Se are the corresponding oxides dissolved in the solution (in this case, an acidic solution). Or it is possible to simply dissolve oxygen or nitrate ions [144,145]. One of the most commonly deposited materials on glass due to its known applications as a photocatalyst are ZnO nanotubes [146].

The electrodeposition mechanism of ZnO was shown by the next Eqs. (1.13)-(1.15) in the deposition solution:

$$NO_3^- + H_2O + 2e^- \rightarrow NO_2^- + 2OH^- \quad (1.13)$$

$$Zn^{2+} + 2OH^- + O_2 \rightarrow Zn(OH)_2 \quad (1.14)$$

$$Zn(OH)_2 \rightarrow ZnO + H_2O \quad (1.15)$$

Initially, the reduction of nitrate generates hydroxide ions at the interface, which then react immediately with Zn^{2+}. Thus, $Zn(OH)_2$ was formed, a process known as hydroxylation.

Further deposition period, zinc hydroxide dehydration produces ZnO. Also, the amounts of ZnO accumulated on the surface of the glass.

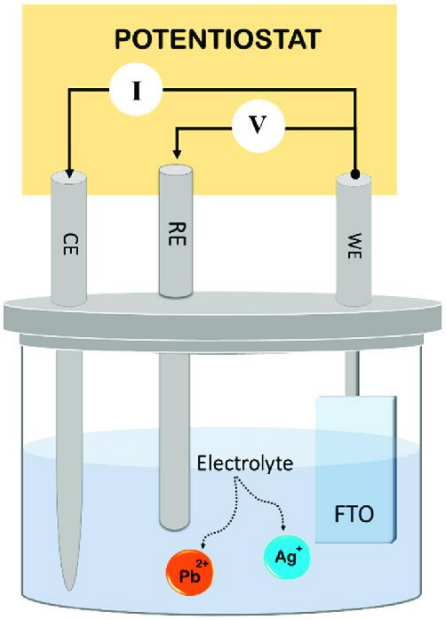

Figure 1.12 Schematic of electrodeposition process for the creation of thin films [143].

1.5. Applications of semiconductors oxide thin films

Semiconductor oxide thin films are widely utilised in diverse fields owing to their distinctive features and adaptable nature. The following are few prevalent applications of thin films composed of semiconductor oxides, in particular, applications based on the interaction of light with these thin layers of semiconductor oxides will be discussed.

For this doctoral thesis the main applications studied have been photocatalysis for environmental remediation, water purification, and the degradation of organic pollutants.

1.5.1. Photocatalysis

This chapter will commence with providing an overview of the mechanistic concepts behind semiconductor photocatalysis, followed by an examination of the fundamental characteristics of photocatalysts.

Following this, we shall delve into several significant reactions, such as the aerial oxidations of pollutants and the use of photocatalysts as agents with antibacterial and antiviral properties. There is a lack of consensus over the precise definition of the term photocatalysis.

The IUPAC (International Union of Pure and Applied Chemistry) defines photocatalysis as the alteration in the rate of a chemical reaction or its initiation when exposed to ultraviolet, visible, or infrared radiation, in the presence of a substance known as the photocatalyst [147].

This photocatalyst absorbs light and actively participates in the chemical transformation of the reaction partners. The process that satisfies this condition is referred to as photocatalytic. The provided definition encompasses the concept of photosensitization, which refers to the occurrence of a photochemical alteration in one molecular entity due to the absorption of radiation by another molecular entity known as a photosensitizer [147].

It is important to note that the substance mentioned can be either a molecular entity or a nonmolecular solid, such as an inorganic semiconductor. It should be noted that these concepts do not distinguish between heterogeneous and homogeneous systems.

Therefore, the broad domain of catalysis can be categorised into two main branches: thermal catalysis, also referred to as catalysis, and photocatalysis. Both fields encompass both homogeneous and heterogeneous reactions.

The term "photokatalytisch" is believed to have first appeared in the textbook "Photochemie," authored by Plotnikov and published in 1910 [148]. Scheme 1.5 illustrates a simplified reaction diagram for thermal catalytic (R+C) and photocatalytic (R+PC) reactions.

In contrast to an uncatalyzed photoreaction, where the absorption of light occurs without the presence of a catalyst (as seen in Figure 1.13), the photocatalyst is often responsible for absorbing the light in a general photoreaction [149].

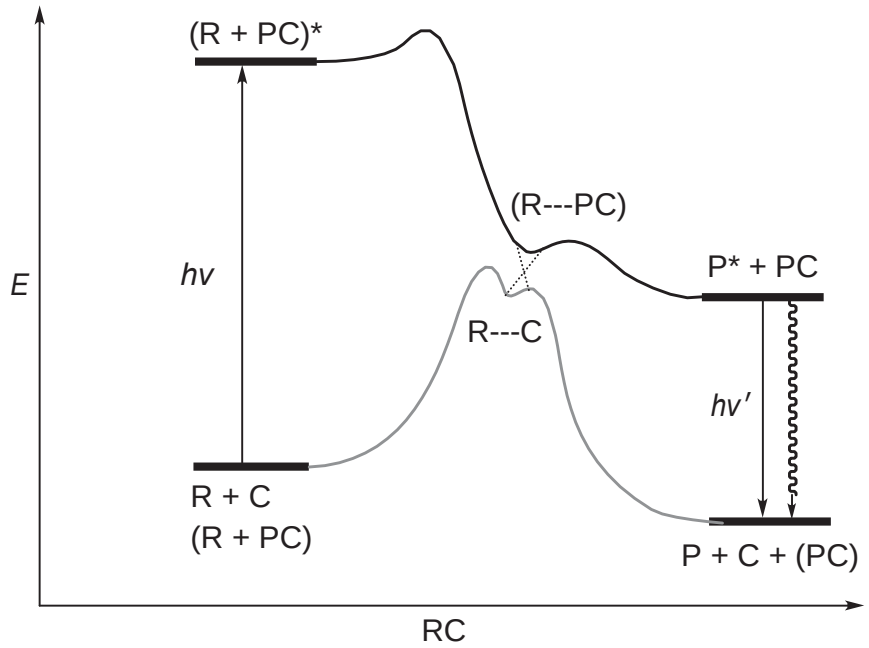

Figure 1.13 Potential energy diagram of a thermal (thin line) and photochemical (bold line) catalytic reaction of R to P. C symbolizes a thermal catalyst, and PC a photocatalyst [149].

Chemical transformations were seen in the early twentieth century when different solid-gas and solid-liquid systems including inorganic insulators (such as alumina (Al_2O_3) and silica (SiO_2)) or semiconductors (such as ZnO and ZnS) were exposed to either natural or artificial light. The initial reports documented the occurrence of many processes, including photocorrosion, photoadsorption of oxygen, and sensitization of photoconductivity, at semiconductor surfaces [150,151].

Semiconductors oxide are particularly well-suited for sensitization because to their ability to exist in several stable oxidation states and their enhanced stability under ambient conditions, which sets them apart from most organic molecules.

Regarding the photoredox reaction in general (Equation.1.16):

$$A + D \overset{hv/SC}{\longleftrightarrow} B_{ox} + C_{red} \tag{1.16}$$

where (SC) is a semiconductor oxide. The process referred to as photocatalysis involves a reaction system in which a solid photocatalyst facilitates two distinct heterogeneous redox processes concurrently [152].

As we learned in Section 1.2.3, light absorption in a semiconductor oxide generates, inter alia, reactive electron-hole pairs (e^-_{CB} and h^+_{VB}) trapped at the surface charges capable of undergoing interfacial electron transfer (IFET) reactions. The fundamental reaction steps of a photocatalyzed reaction using a semiconductor material can be succinctly described by Equations (1.17–1.19) [153].

$$SC + hv \rightarrow (e^-_{CB} + h^+_{VB}) \tag{1.17}$$

$$SC(e^-_{CB} + h^+_{VB}) \rightarrow SC + \ hv/heat \tag{1.18}$$

$$SC(e^-_{CB} + h^+_{VB}) + A + D \rightarrow SC + A^{-\bullet} + D^{+\bullet} \tag{1.19}$$

Hence, the previously described reaction scheme bears resemblance to an electrochemical reaction, whereby the reactive electron and hole are regarded as a nanocathode and nanoanode, respectively.

Given that the generation of electrical charges is facilitated by the absorption of light, the need for an external voltage application is rendered unnecessary. In a similar manner to electrochemistry, the formation of reduced and oxidised products occurs, as illustrated in Equation 1.16.

The equation provided can be used to describe the overall reaction for the majority of SC-photocatalyzed processes [154].

The illustration of type A responses has gained widespread acceptance in the literature, as illustrated in Figure 1.14. The circular shape serves as a representation of a SC particle, typically comprising a group of nanoparticles[155].

The upper and lower lines within the circle signify the boundaries of the conduction and valence band edges, respectively.

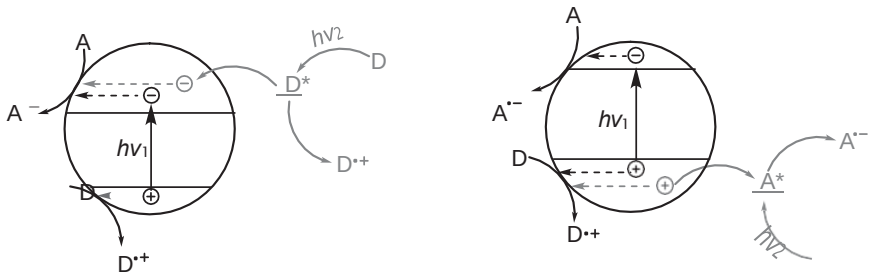

Figure 1.14 (a) Direct (via hν_1) and (b) indirect (via hν_2) semiconductor photocatalysis [155].

The thermodynamic feasibility of a reaction catalysed by a semiconductor photocatalyst is often assessed by evaluating the following properties:

- It is necessary for the reduction potentials of the substrates to fall within the bandgap range of the semiconductor [156].
- The light-absorbing species can be identified by comparing the electronic absorption spectra of the substrate with the diffuse reflectance spectrum of the semiconductor [156].

In general, the semiconductor acts as the primary light-absorbing element, although there are instances where it can also function as a substrate or form a complex with the SC-substrate surface.

The nomenclature “direct” and “indirect” semiconductor photocatalysis was suggested for the classification of these two reactions types. In the direct mechanism, the indicent light ($h\nu_1$) induces the formation of a localized electron-hole pair at the surface of the semiconductor [157].

This is subsequently followed by two interfacial electron transfer (IFET) events involving substrates A and D. While the existence of this conventional mechanism is commonly expected, it frequently lacks empirical support due to the absorption of light by the substrates or their surface charge-transfer complexes.

The analysis of the absorption spectra of the substrates and the semiconductor typically enables the determination of a preferred mechanism. When a substrate undergoes light absorption, a common occurrence in the aerial oxidation of dyes, the dye that is stimulated may introduce an electron into the conduction band (as depicted in Figure 1.15) [158].

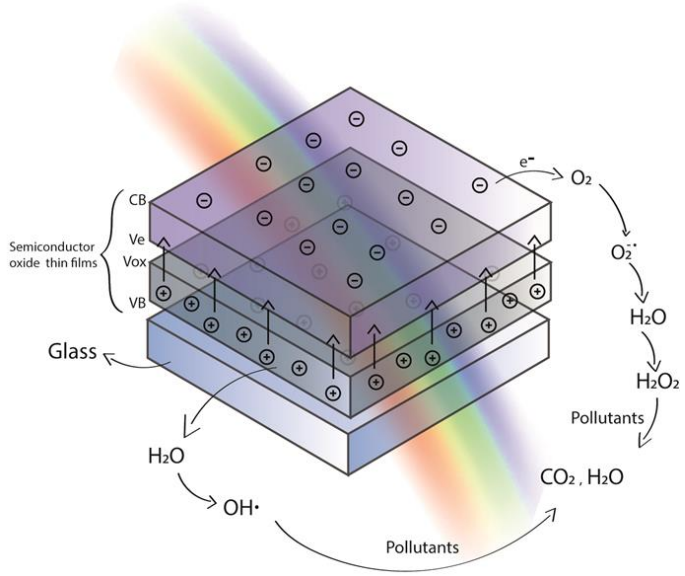

Figure 1.15 Schematic illustration of photoactivation of semiconductor oxide thin films and generation of electron-hole pairs.

Thermodynamic feasibility is contingent upon the excited state reduction potential being equivalent to or more negative than the flatband potential. The separation between the two charges that are created leads to a deceleration in the process of recombination.

In the realm of semiconductor photosensitization, the Sakata-Hashimoto-Hiramoto mechanism [157] is an alternative term used to describe this particular form of photoinduced electron transfer (PET). (as depicted in Equations (1.20-1.22):

$$D \xrightarrow{h\nu} D^* \quad (1.20)$$

$$D^* + SC \rightarrow SC(e_{CB}^-) + D^{+\bullet} \quad (1.21)$$

$$SC(e_{CB}^-) + A \rightarrow SC + A^{-\bullet} \quad (1.22)$$

In conclusion, the aforementioned discussions yield the following recommendations for the strategic planning of a reaction utilising semiconductor (SC)-photocatalysis:

- The purpose of this analysis is to compare the absorption spectra of the semiconductor, substrates, and products in order to elucidate the characteristics of the light-absorbing entities and prevent any potential interference from mutual product absorption.
- The objective is to determine the reduction potentials of substrates.
- To assess the thermodynamic feasibility of the reaction steps in the IFET (Interfacial Electron Transfer) system, it is necessary to determine the position of the flatband potential, also known as the quasi-Fermi level.

The whole process of oxidising dye deposits in polluted waterways is a well researched area within the realm of indirect photocatalysis [159]. It is important to note that within a certain mechanism, the absorption of light is solely attributed to the dye.

For this to occur, the reduction potential of the dye's excited state must be equal to or more negative than the conduction band edge, or a nearby situated vacant surface state.

In such circumstances, the injection of electrons into the conduction band could potentially take place through a process known as photoinduced electron transfer (PET) [157].

The resulting dye radical cation experiences rapid deprotonation, leading in the formation of an intermediate radical that undergoes further oxidation giving rise to degradation products (DP) or by degrading the dyes to CO_2 and water. (Equation 1.21-1.24).

$$SC + h\nu \rightarrow (e_{CB}^{-} + h_{VB}^{+}) \quad (1.21)$$

$$SC + e_{CB}^{-} + O_2 \rightarrow O_2^{-\bullet} \quad (1.22)$$

$$SC + h_{VB}^{+} + H_2O \rightarrow H^{+} + OH\bullet \quad (1.23)$$

$$Pollutants + O_2^{-\bullet} + OH\bullet \rightarrow DP + (CO_2 + H_2O + Mineral\ acid \quad (1.24)$$

In this way, as will be will be studied the photocatalytic capacity of two particular semiconducting oxides, both titanium oxide and zinc oxide in the form of thin films as a new application for the functionalisation of glasses.

1.5.2. Antimicrobial surfaces

The generation of reactive oxygen compounds at the surface of semiconductors has been found to elicit significant biological consequences, such as the eradication of bacteria and viruses [160,161].

The photochemical technique described herein has the ability to render bacteria non-viable, including those that exhibit resistance to oxidative membrane damage resulting from direct exposure to UV radiation.

The efficacy of the approach remains intact even in cases when a bacteria has been physically detached from the surface of the semiconductor [162,163].

Cellular oxidative damage occurs initially at the cell wall and persists inside the intracellular region, ultimately resulting in cellular demise [164]. Escherichia coli was frequently employed as the prototypical bacteria in several studies [165–167].

In addition, various microorganisms such as Staphylococcus aureus, Salmonella choleraesuis, Listeria monocytogenes, Streptococcus mutans, and Legionella pneumophila, as well as viral pathogens including avian influenza virus, HIV virus, and SARS coronavirus, have been observed to undergo deactivation. Furthermore, murine macrophages and cancer cells have also been found to exhibit deactivation [167–169].

It should be acknowledged that conducting a quantitative comparison of the killing efficiencies of different photocatalysts is not meaningful due to the variations in experimental settings [170].

The word "antimicrobial" is used in a broad manner in the present literature, embracing several mechanisms of action that, in some way, may contribute to the prevention of bacterial-associated infections (BAI). There are three distinct mechanisms of antimicrobial action that can be identified [171,172].

These mechanisms are categorised based on (1) surfaces that release antimicrobials, (2) surfaces that directly kill adhering bacteria upon adhesion without the release of antimicrobials (known as contact-killing), and (3) surfaces that are nonadhesive towards bacteria (referred to as non-adhesivity) [173]. (It is important to note that the term "antifouling" is deliberately avoided in this context due to its lack of specificity.)

The term "fouling" pertains to the undesired accumulation of substances on a surface, including various instances such as the presence of microbes on biomaterials, implants, and devices, as well as the attachment of barnacles and mussels in a marine setting [174,175]. On the other hand, the term "*anti*" contains all potential techniques that aim to hinder or diminish fouling. The application of local antimicrobial release, utilising substances such as gentamicin and amoxicillin, has been implemented in several medical devices including cardiovascular stents, surgical meshes, urine catheters, orthopaedic implants, and trauma devices [173].

Numerous antimicrobial surface designs for biomaterials or coatings that have been documented in scholarly publications often fail to transition into clinical application.

This is primarily due to the industry's demand for uncomplicated, durable, and cost-effective manufacturing methods for antimicrobial surface designs, while regulatory agencies necessitate expensive and often statistically unattainable large-scale clinical trials prior to permitting market release [176].

Furthermore, the process of obtaining consent for animal studies has grown increasingly challenging. In many countries, the authorization for conducting animal experiments is contingent upon providing compelling in vitro evidence of effectiveness. The significance lies in the development of appropriate in vitro assessment techniques for antimicrobial surface designs, with a focus on specific mechanisms of action [177].

To effectively evaluate the antimicrobial properties of biomaterials and coatings, it is imperative to establish a precise and comprehensive definition of the term "*antimicrobial*."

The term "*antimicrobial*" activity, as defined by ISO 20743, refers to the effectiveness of an antibacterial treatment in inhibiting or reducing the growth of bacteria, or in eliminating bacteria altogether [178]. According to the Japanese Industry Standard (JIS) Z 2801, the term "*antimicrobial*" is defined as the state in which the growth of bacteria on product surfaces is inhibited [179].

Significantly, it is noteworthy that ISO 20743 incorporates both growth inhibition and bacterial death in its description of antimicrobial activity, whereas JIS Z 2801 solely references growth inhibition. Nevertheless, their definition of antimicrobial activity fails to differentiate between the act of killing microorganisms and the act of inhibiting their proliferation.

The efficacy of antimicrobial products is assessed by both organisations by comparing the logarithmic difference in viable cell counts between the antimicrobial test products and inert controls. This assessment is conducted after incubating the samples in the presence of a bacterial inoculum (Equation 1.25) [173].

$$A = \log\left(\frac{C_t}{C_0}\right) - \log\left(\frac{T_t}{T_0}\right) \tag{1.25}$$

The challenge numbers of bacteria before incubation on the control and antimicrobial test sample are denoted as C_0 and T_0, respectively. The numbers of bacteria typically obtained after 16-24 hours of incubation from the control and test sample are denoted as C_t and T_t, respectively.

Ideally, it is desirable for C_0 and T_0 to possess equivalent numerical values, although attaining this equivalence proves challenging when assessing non-adhesive surfaces.

Under optimal circumstances, Equation (1.25) simplifies to its more widely recognised expression (Equation 1.26).

$$A = \log\left(\frac{C_t}{T_t}\right) = \log(C_t) - \log(T_t) \quad (1.26)$$

The evaluation tests that are commonly used in industry (refer to Table 1.3) primarily aim to evaluate the effectiveness of non-medical products in preventing the growth of microorganisms [173].

The efficacy of most common procedures is evaluated by assessing the antimicrobial activity value using Equation (1.26). It is important to acknowledge that the determination of antimicrobial activity is heavily influenced by the logarithmic scale used.

It is important to acknowledge, however, that the antimicrobial activity levels are heavily influenced by the bacterial challenge numbers used, as a logarithmic scale is employed. For instance, a log reduction of 2 refers to a significant decrease in the number of bacteria, particularly when transitioning from 10^8 to 10^6, as opposed to the decrease from 10^4 to 10^2.

Equation (1.26) can also be employed in its linear, similar version as indicated by previous studies [180–182], wherein it is denoted as Equation (1.27).

$$A\ (\%) = 100 - \left(\frac{T_t}{C_t}\right) \times 100 \quad (1.27)$$

The assessment of antimicrobial activity values A can be conducted only based on statistically significant differences. However, from a microbiological standpoint, it is important to consider the criteria outlined in JIS Z 2801. In this context, differences are considered substantial only when they exceed two log-units or are expressed linearly as greater than 99% [183].

Therefore, in the present thesis we will study the existence of this activity in different oxide semiconductors, more specifically TiO_2 or ZnO in powder form and in thin film form.

Table 1.3 Industrial standard evaluation tests of antimicrobial surface designs together with their intended application. (AATCC: American Association of Textile Chemists and Colorists, ASTM: American Society for Testing and Materials, EN: European Standard, ISO: International Standard Organisation, JIS: Japanese Industrial Standard, SN: Schweizerische Normen Vereinigung)[173].

Standard	Application area
AATCC 30 Antifungal Activity	Textiles/Fabrics
AATCC 90 Antibacterial Activity	Textiles/Fabrics
AATCC 100 Assessment of Antibacterial	Textiles/Fabrics
AATCC 147 Antibacterial Activity	Textiles/Fabrics

Standard	Application area
ASTM E2149 Standard Test Method for Determining the Antimicrobial Activity of Antimicrobial Agents Under Dynamic Contact Conditions	Textiles /Fabrics
ASTM E2180-07 Standard Test Method for Determining the Activity of Incorpored Antimicrobial Agents(s) In Polymeric or Hydrophobic Materials	Textiles /Fabrics
ASTM E2722 Standard Test Method for Using Seeded-Agar for the Screening Assessment of Antimicrobial Activity in Fabric and Air Filter Media	Textiles /Fabrics
ISO 20645 Textile fabrics - Determination of Antibacterial Activity	Textiles /Fabrics

Standard	Application area
ISO 22196 Plastics – Measurement of Antibacterial Activity on Plastics Surfaces	Non-porous materials
JIS L 1902 Testing for Antibacterial Activity and Efficacy on Textile Products	Textiles /Fabrics
SN 195920 Textile fabrics Determination of Antibacterial Activity -	Textiles /Fabrics
ISO 20645 Textile fabrics - Determination of Antibacterial Activity	Textiles /Fabrics

1.6. References

[1] M. Hajji, M. Ajili, N. Jebbari, A. Garcia loreiro, N.T. Kamoun, Photocatalytic performance and solar cell applications of coupled semiconductor CuO– ZnO sprayed thin films: Coupling effect between oxides, Opt. Mater. (Amst). 140 (2023) 113798. https://doi.org/10.1016/j.optmat.2023.113798.

[2] X.Y. Zhang, Q. Ren, C. Wang, L. Zhu, W.J. Ding, Y.Q. Cao, W.M. Li, D. Wu, A.D. Li, Atomic layer deposited SnO_2/ZnO composite thin film sensors with enhanced hydrogen sensing performance, Appl. Surf. Sci. 639 (2023) 1–8. https://doi.org/10.1016/j.apsusc.2023.157973.

[3] G. Tatrari, M. Ahmed, F.U. Shah, Synthesis , thermoelectric and energy storage performance of transition metal oxides composites, Coord. Chem. Rev. 498 (2024) 215470. https://doi.org/10.1016/j.ccr.2023.215470.

[4] J.A. Oke, T.C. Jen, Atomic layer deposition and other thin film deposition techniques: From principles to film properties, J. Mater. Res. Technol. 21 (2022) 2481–2514. https://doi.org/10.1016/j.jmrt.2022.10.064.

[5] F. Liang, J.R. Yang, Y. Zhao, Y. Zhou, Z. Yan, J.C. He, Q. Yuan, J. Wu, P. Liu, Z. Zhong, M. Han, A review of thin film electrolytes fabricated by physical vapor deposition for solid oxide fuel cells, Int. J. Hydrogen Energy. 47 (2022) 36926–36952. https://doi.org/10.1016/j.ijhydene.2022.08.237.

[6] C. Aparna, P.K. Shetty, M.G. Mahesha, N. Karunakara, I. Yashodhara, Structural, optical and sensitivity study of optimized indium oxide thin film for gamma sensing applications, Sensors Actuators A Phys. 345 (2022) 113785. https://doi.org/10.1016/j.sna.2022.113785.

[7] J.A. Oke, O.O. Olotu, T.C. Jen, Atomic layer deposition of chalcogenide thin films: processes, film properties, applications, and bibliometric prospect, J. Mater. Res. Technol. 20 (2022) 991–1019. https://doi.org/10.1016/j.jmrt.2022.07.098.

[8] J. Tyczkowski, R. Kapica, J. Łojewska, Thin cobalt oxide films for catalysis deposited by plasma-enhanced metal-organic chemical vapor deposition, Thin Solid Films. 515 (2007) 6590–6595. https://doi.org/10.1016/j.tsf.2006.11.056.

[9] A.R. Patil, T.D. Dongale, R.K. Kamat, K.Y. Rajpure, Binary metal oxide-based resistive switching memory devices: A status review, Mater. Today Commun. 34 (2023) 105356. https://doi.org/10.1016/j.mtcomm.2023.105356.

[10] A.K. Eessaa, A.M. El-Shamy, Review on fabrication, characterization, and applications of porous anodic aluminum oxide films with tunable pore sizes for emerging technologies, Microelectron. Eng. 279 (2023) 112061. https://doi.org/10.1016/j.mee.2023.112061.

[11] A. Abdel-Galil, M.S.A. Hussien, I.S. Yahia, Low cost preparation technique for conductive and transparent Sb doped SnO_2 nanocrystalline thin films for solar cell applications, Superlattices Microstruct. 147 (2020) 106697. https://doi.org/10.1016/j.spmi.2020.106697.

[12] W. Cui, F. Chen, Y. Li, X. Su, B. Sun, Status and perspectives of transparent conductive oxide films for silicon heterojunction solar cells, Mater. Today Nano. 22 (2023) 100329. https://doi.org/10.1016/j.mtnano.2023.100329.

[13] S. Gupta, A. Paliwal, R. Guo, A.S. Bhalla, V. Gupta, M. Tomar, Demonstration of wide frequency bandwidth electro-optic response in SBN thin film waveguide, Opt. Mater. (Amst). 85 (2018) 26–31. https://doi.org/10.1016/j.optmat.2018.08.008.

[14] S.K. Al-Hayali, A.H. Al-Janabi, All fiber-optic temperature sensor based on cladding etched no-core fiber coated with nanostructured copper oxide-polyvinyl alcohol thin film, Optik (Stuttg). 220 (2020) 165154. https://doi.org/10.1016/j.ijleo.2020.165154.

[15] M. Karuppaiah, P. Sakthivel, S. Asaithambi, V. Balaji, G. Vijayaprasath, R. Yuvakkumar, G. Ravi, In-situ deposition of amorphous Tungsten(VI) oxide thin-film for solid-state symmetric supercapacitor, Ceram. Int. 48 (2022) 2510–2521. https://doi.org/10.1016/j.ceramint.2021.10.033.

[16] A. Raza, M.K. Azeem, M.S. Nazir, I. Ahmad, Robust nonlinear control of regenerative fuel cell, supercapacitor, battery and wind based direct current microgrid, J. Energy Storage. 64 (2023) 107158. https://doi.org/10.1016/j.est.2023.107158.

[17] C.D. Lokhande, D.P. Dubal, O.S. Joo, Metal oxide thin film based supercapacitors, Curr. Appl. Phys. 11 (2011) 255–270. https://doi.org/10.1016/j.cap.2010.12.001.

[18] S. Uma, M.K. Shobana, Metal oxide semiconductor gas sensors in clinical diagnosis and environmental monitoring, Sensors Actuators A Phys. 349 (2023) 114044. https://doi.org/10.1016/j.sna.2022.114044.

[19] M. Ramya, P. Senthil Kumar, G. Rangasamy, V. Uma shankar, G. Rajesh, K. Nirmala, A. Saravanan, A. Krishnapandi, A recent advancement on the applications of nanomaterials in electrochemical sensors and biosensors, Chemosphere. 308 (2022) 136416. https://doi.org/10.1016/j.chemosphere.2022.136416.

[20] G. Divya, G. Jaishree, T. Sivarao, K.V.D. Lakshmi, RSC Advances Microwave assisted sol – gel approach for Zr doped TiO_2 as a benign photocatalyst for bismark brown, (2023) 8692–8705. https://doi.org/10.1039/d3ra00328k.

[21] A. Kudo, Y. Miseki, Heterogeneous photocatalyst materials for water splitting, Chem. Soc. Rev. 38 (2009) 253–278. https://doi.org/10.1039/b800489g.

[22] L. Liu, T. Hu, K. Dai, J. Zhang, C. Liang, A novel step-scheme $BiVO_4/Ag_3VO_4$ photocatalyst for enhanced photocatalytic degradation activity under visible light irradiation, Chinese J. Catal. 42 (2020) 46–55. https://doi.org/10.1016/S1872-2067(20)63560-4.

[23] R. Gang, Y. Xia, L. Xu, L. Zhang, S. Ju, Size controlled Ag decorated TiO_2 plasmonic photocatalysts for tetracycline degradation under visible light, Surfaces and Interfaces. (2022) 102018. https://doi.org/10.1016/j.surfin.2022.102018.

[24] R.D. Suryavanshi, S. V. Mohite, A.A. Bagade, S.K. Shaikh, J.B. Thorat, K.Y. Rajpure, Nanocrystalline immobilised ZnO photocatalyst for degradation of benzoic acid and methyl blue dye, Mater. Res. Bull. 101 (2018) 324–333. https://doi.org/10.1016/j.materresbull.2018.01.042.

[25] N. Lu, J. Cai, B. Niu, Y. Zhou, G. Zhao, Preferential Removal of Phthalic Esters by Photocatalysis on Targeting-Selective TiO_2, SSRN Electron. J. 460 (2022) 141735. https://doi.org/10.2139/ssrn.4269853.

[26] J. Singh, R.K. Soni, Fabrication of nanostructured In_2S_3 thin film with broad optical absorption for improved sunlight mediated photocatalysis application, Opt. Mater. (Amst). 122 (2021) 111748. https://doi.org/10.1016/j.optmat.2021.111748.

[27] L. Demelius, M. Blatnik, K. Unger, P. Parlanti, M. Gemmi, A.M. Coclite, Shedding light on the initial growth of ZnO during plasma-enhanced atomic layer deposition on vapor-deposited polymer thin films, Appl. Surf. Sci. 604 (2022) 154619. https://doi.org/10.1016/j.apsusc.2022.154619.

[28] J. Banas-Gac, M. Radecka, A. Czapla, E. Kusior, K. Zakrzewska, Surface and interface properties of TiO_2/CuO thin film bilayers deposited by rf reactive magnetron sputtering, Appl. Surf. Sci. 616 (2023) 156394. https://doi.org/10.1016/j.apsusc.2023.156394.

[29] P. Wang, X. Pan, N. Wang, S. Zheng, T. Zhang, Y. Liu, Y. Wang, F. Wang, G. Zhu, J. Wang, Z. Ye, Epitaxy and bonding of peelable ZnO film on graphene/ZnO substrate, J. Alloys Compd. 928 (2022) 167129. https://doi.org/10.1016/j.jallcom.2022.167129.

[30] X. Yu, T.J. Marks, A. Facchetti, Metal oxides for optoelectronic applications, Nat. Mater. 15 (2016) 383–396. https://doi.org/10.1038/nmat4599.

[31] H. Kierzkowska-Pawlak, E. Kruszczak, J. Tyczkowski, Catalytic activity of plasma-deposited Co_3O_4-based thin films for CO_2 hydration – A new approach to carbon capture applications, Appl. Catal. B Environ. 304 (2022) 120961. https://doi.org/10.1016/j.apcatb.2021.120961.

[32] G. Waldner, A. Brüger, N.S. Gaikwad, M. Neumann-Spallart, WO_3 thin films for photoelectrochemical purification of water, Chemosphere. 67 (2007) 779–784. https://doi.org/10.1016/j.chemosphere.2006.10.024.

[33] B. Sharma, A. Sharma, Enhanced surface dynamics and magnetic switching of α-Fe_2O_3 films prepared by laser assisted chemical vapor deposition, Appl. Surf. Sci. 567 (2021) 150724. https://doi.org/10.1016/j.apsusc.2021.150724.

[34] Y. Bao, C. Shi, T. Wang, X. Li, J. Ma, Microporous and Mesoporous Materials Recent progress in hollow silica : Template synthesis , morphologies and applications, Microporous Mesoporous Mater. 227 (2016) 121–136. https://doi.org/10.1016/j.micromeso.2016.02.040.

[35] S.R. Sitaaraman, M.I. Shanmugapriyan, K. Varunkumar, A.N. Grace, R. Sellappan, Materials Today : Proceedings Synthesis of heterojunction tungsten oxide
(WO_3) and Bismuth vanadate ($BiVO_4$) photoanodes by spin coating method for solar water splitting applications, Mater. Today Proc. 45 (2021) 3920–3926. https://doi.org/10.1016/j.matpr.2020.07.601.

[36] P. Narin, E. Kutlu-Narin, S. Kayral, R. Tulek, S. Gokden, A. Teke, S.B. Lisesivdin, Morphological and optical characterizations of different ZnO nanostructures grown by mist-CVD, J. Lumin. 251 (2022) 119158. https://doi.org/10.1016/j.jlumin.2022.119158.

[37] G. Wang, S. Lv, Y. Shen, W. Li, L. Lin, Z. Li, Advancements in heterojunction, cocatalyst, defect and morphology engineering of semiconductor oxide photocatalysts, J. Mater. (2023). https://doi.org/10.1016/j.jmat.2023.05.014.

[38] N. Hossain, M.H. Mobarak, M.A. Mimona, M.A. Islam, A. Hossain, F.T. Zohura, M.A. Chowdhury, Advances and significances of nanoparticles in semiconductor applications – A review, Results Eng. 19 (2023) 101347. https://doi.org/10.1016/j.rineng.2023.101347.

[39] Crystal structure of solids, in: J.S. Galsin (Ed.), Solid State Physics, Academic Press, 2019, pp. 1–36. https://doi.org/10.1016/b978-0-12-817103-5.00001-3.

[40] G. Burns, A.M. Glazer, Bravais Lattices, Sp. Groups Solid State Sci. (2013) 45–64. https://doi.org/10.1016/b978-0-12-394400-9.00003-4.

[41] Büttner, H. (1989), Electrons in solids: An introductory survey. By R. H. Bube. Academic Press Inc., San Diego 1988. xiv, 315 pp., bound, ISBN 0-12-138552-3. Adv. Mater., 1: 173-174. https://doi.org/10.1002/adma.19890010510

[42] Hummel, R.E. (2001) Electronic Properties of Materials. 3rd Edition, Springer, New York. https://doi.org/10.1007/978-1-4419-8164-6

[43] Myers, H.P. (1990). Introductory Solid State Physics (1st ed.). Taylor & Francis. https://doi.org/10.1201/9781315273303

[44] Ėvarestov R. A. (2012). Quantum chemistry of solids : lcao treatment of crystals and nanostructures (2nd ed.). Springer. https://doi.org/10.1007/978-3-642-30356-2

[45] C. Han, S. Han, J. Gwak, S.P. Khatkar, Synthesis of indium tin oxide (ITO) and fluorine-doped tin oxide (FTO) nano-powder by sol – gel combustion hybrid method, 61 (2007) 1701–1703. https://doi.org/10.1016/j.matlet.2006.07.114.

[46] T. Shirahata, T. Kawaharamura, S. Fujita, H. Orita, Transparent conductive zinc-oxide-based films grown at low temperature by mist chemical vapor deposition, Thin Solid Films. 597 (2015) 30–38. https://doi.org/10.1016/j.tsf.2015.11.006.

[47] C. F. Klingshirn, B. K. Meyer, A. Waag, A. Hoffmann and J. Geurts, “Zinc Oxide. From fundamental properties towards novel applications”, Springer Series in Materials Science120, pp. 1-359 (2010). https://doi.org/10.1007/978-3-642-10577-7

[48] Ü. Özgür, Y.I. Alivov, C. Liu, A. Teke, M.A. Reshchikov, S. Doğan, V. Avrutin, S.J. Cho, H. Morkǫ, A comprehensive review of ZnO materials and devices, J. Appl. Phys. 98 (2005) 1–103. https://doi.org/10.1063/1.1992666.

[49] C. Klingshirn, in Semiconductor Optics, Science Press, Beijing, 3rd edn., 2007, pp. 310-315. https://doi.org/https://doi.org/10.1007/978-3-540-38347-5.

[50] E. Tomzig, R. Helbig, Band-edge emission in ZnO, J. Lumin. 14 (1976) 403–415. https://doi.org/10.1016/0022-2313(76)90009-0.

[51] U.L.N.H. Senarathna, S.S.N. Fernando, T.D.C.P. Gunasekara, M.M. Weerasekera, H.G.S.P. Hewageegana, N.D.H. Arachchi, H.D. Siriwardena, P.M. Jayaweera, Enhanced antibacterial activity of TiO_2 nanoparticle surface modified with Garcinia zeylanica extract, Chem. Cent. J. 11 (2017) 1–8. https://doi.org/10.1186/s13065-017-0236-x.

[52] M.I. Khan, K.A. Bhatti, R. Qindeel, H.S. Althobaiti, N. Alonizan, Structural, electrical and optical properties of multilayer TiO_2 thin films deposited by sol–gel spin coating, Results Phys. 7 (2017) 1437–1439. https://doi.org/10.1016/j.rinp.2017.03.023.

[53] M. Balamurugan, M. Silambarasan, S. Saravanan, T. Soga, Synthesis of anatase and rutile mixed phase titanium dioxide nanoparticles using simple solution combustion method, Phys. B Condens. Matter. 638 (2022) 413843. https://doi.org/10.1016/j.physb.2022.413843.

[54] K. Nagaveni, G. Sivalingam, M.S. Hegde, G. Madras, Solar photocatalytic degradation of dyes: High activity of combustion synthesized nano TiO_2, Appl. Catal. B Environ. 48 (2004) 83–93. https://doi.org/10.1016/j.apcatb.2003.09.013.

[55] D.P. Rawski, M.S.H. Bhuiyan, Pulp and Paper: Nonfibrous Components , Ref. Modul. Mater. Sci. Mater. Eng. (2017) 1–4. https://doi.org/10.1016/b978-0-12-803581-8.10289-9.

[56] A. Crespo, J. Gallenberger, M. De Santis, V. Langlais, F. Carla, J.M. Caicedo, J. Rius, X. Torrelles, Heteroepitaxial growth of anatase (001) films on $SrTiO_3$ (001) by PLD and MBE Applied Surface Science, 632 (2023), 157586, https://doi.org/10.1016/j.apsusc.2023.157586.

[57] Z. Huang, H. Liu, Insights into the pathways, intermediates, influence factors and toxicological properties in the degradation of tetracycline by TiO_2-based photocatalysts, J. Environ. Chem. Eng. 11 (2023) 110587. https://doi.org/10.1016/j.jece.2023.110587.

[58] M. Mohsin, I.A. Bhatti, M. Zeshan, M. Yousaf, M. Iqbal, Prospects, challenges, and opportunities of the metals-modified TiO_2 based photocatalysts for hydrogen generation under solar light irradiation: A review, FlatChem. 42 (2023) 100547. https://doi.org/10.1016/j.flatc.2023.100547.

[59] D.A.H. Hanaor, C.C. Sorrell, Review of the anatase to rutile phase transformation, J. Mater. Sci. 46 (2011) 855–874. https://doi.org/10.1007/s10853-010-5113-0.

[60] N. Madkhali, C. Prasad, K. Malkappa, H.Y. Choi, V. Govinda, I. Bahadur, R.A. Abumousa, Recent update on photocatalytic degradation of pollutants in waste water using TiO_2-based heterostructured materials, Results Eng. 17 (2023) 100920. https://doi.org/10.1016/j.rineng.2023.100920.

[61] S. iti Kitazawa, Y. Choi, S. Yamamoto, T. Yamaki, Rutile and anatase mixed crystal TiO_2 thin films prepared by pulsed laser deposition, Thin Solid Films. 515 (2006) 1901–1904. https://doi.org/10.1016/j.tsf.2006.07.032.

[62] Y.R. Park, K.J. Kim, Structural and optical properties of rutile and anatase TiO_2 thin films: Effects of Co doping, Thin Solid Films. 484 (2005) 34–38. https://doi.org/10.1016/j.tsf.2005.01.039.

[63] E. Laudadio, E. Mohebbi, E. Pavoni, C. Minnelli, S. Sabbatini, P. Stipa, Density functional theory and molecular dynamics studies on electrical, mechanical, and thermal properties of TiO_2 nanoparticles interacting with poly lactic-co-glycolic acid, Colloids Surfaces A Physicochem. Eng. Asp. 667 (2023) 131388. https://doi.org/10.1016/j.colsurfa.2023.131388.

[64] S.R. Kodigala, Fabrication and Properties of Window Layers For Thin Film Solar Cells, Thin Film. Nanostructures. 35 (2010) 393–504. https://doi.org/10.1016/B978-0-12-373697-0.00007-9.

[65] E. Matei, M. Enculescu, N. Preda, I. Enculescu, ZnO morphological, structural and optical properties control by electrodeposition potential sweep rate, Mater. Chem. Phys. 134 (2012) 988–993. https://doi.org/10.1016/j.matchemphys.2012.03.101.

[66] A. Abu-Odeh, D.L. Olmsted, M. Asta, Screw dislocation mobility in a face-centered cubic solid solution with short-range order, Scr. Mater. 210 (2022) 114465. https://doi.org/10.1016/j.scriptamat.2021.114465.

[67] S. Esmizadeh, H. Haftbaradaran, A model for redistribution of oppositely charged point defects under the stress field of dislocations in nonstoichiometric ionic solids: Implications in doped ceria, J. Mech. Phys. Solids. 174 (2023) 105242. https://doi.org/10.1016/j.jmps.2023.105242.

[68] J. Yuan, Y. Huang, W. Chen, E. Pan, G. Kang, Theory of dislocation loops in multilayered anisotropic solids with magneto-electro-elastic couplings, J. Mech. Phys. Solids. 125 (2019) 440–471. https://doi.org/10.1016/j.jmps.2019.01.005.

[69] N.M. Rowley, Advanced Advanced, 9 (1994) 807–808.

[70] Q. Yu, P.A. Greaney, T.M. Evans, J.J. Kruzic, A critical dislocation velocity for serration mechanism transition in a nickel-chromium solid solution alloy, Int. J. Plast. 145 (2021) 103071. https://doi.org/10.1016/j.ijplas.2021.103071.

[71] N. Yadav, P. Roy, A. Khare, An investigation of defects, band-offset, and Schottky barrier height for boosting the performance of formamidinium mixed cation mixed halide based perovskite solar cell: Theoretical approach, Mater. Sci. Eng. B. 293 (2023) 116458. https://doi.org/10.1016/j.mseb.2023.116458.

[72] N. Anwar, R.M. Harker, M.T. Storr, M. Molinari, C.K. Skylaris, Linear-scaling density functional theory (DFT) simulations of point, Frenkel and Schottky defects in CeO_2, Comput. Mater. Sci. 229 (2023) 112396. https://doi.org/10.1016/j.commatsci.2023.112396.

[73] P. Cerisier, P. Gaune, Application of the method of mott and Littleton to $NaNO_3$ calculation of enthalpies of formation of Schottky and Frenkel defects, J. Solid State Chem. 3 (1971) 473–477. https://doi.org/10.1016/0022-4596(71)90088-0.

[74] K. Mizuno, S. Yamamoto, K. Morikawa, M. Kuga, H. Okamoto, E. Hashimoto, Vacancy generation mechanism at high temperatures in ultrahigh-purity aluminum single crystals with a low dislocation density, J. Cryst. Growth. 275 (2005) 1697–1702. https://doi.org/10.1016/j.jcrysgro.2004.11.247.

[75] A. Chatterjee, S.K. Khamari, R. Kumar, S. Porwal, A. Bose, T.K. Sharma, Role of threading dislocations and point defects in the performance of GaN-based metal-semiconductor-metal ultraviolet photodetectors, Superlattices Microstruct. 148 (2020) 106733. https://doi.org/10.1016/j.spmi.2020.106733.

[76] N. Duhan, R.U. Patil, B.K. Mishra, I. V. Singh, Y.E. Pak, Nonlinear thermo-elastic analysis of edge dislocations with Internal Heat Generation in Semiconductor Materials, Mech. Mater. 169 (2022) 104322. https://doi.org/10.1016/j.mechmat.2022.104322.

[77] D. Rodney, L. Ventelon, E. Clouet, L. Pizzagalli, F. Willaime, Ab initio modeling of dislocation core properties in metals and semiconductors, Acta Mater. 124 (2017) 633–659. https://doi.org/10.1016/j.actamat.2016.09.049.

[78] S. Xia, W. Zhang, Z. Yuan, J. Li, J. Ye, Y. Gu, Y. Miao, C. Li, Y. Deng, A. Shen, H. Lu, Y.F. Chen, A dislocation-driven laminated relaxation process in $Si_{1-x}Ge_x$ grown on Si (001) by molecular beam epitaxy, Mater. Today Nano. 16 (2021) 1–7. https://doi.org/10.1016/j.mtnano.2021.100140.

[79] A. Vilan, D. Cahen, Chemical Modification of Semiconductor Surfaces for Molecular Electronics, Chem. Rev. 117 (2017) 4624–4666. https://doi.org/10.1021/acs.chemrev.6b00746.

[80] L.K. Ono, Y. Qi, Surface and Interface Aspects of Organometal Halide Perovskite Materials and Solar Cells, J. Phys. Chem. Lett. 7 (2016) 4764–4794. https://doi.org/10.1021/acs.jpclett.6b01951.

[81] V. Katsika-Tsigourakou, A remark on the negative activation volume for defects in solids, J. Non. Cryst. Solids. 358 (2012) 2988–2989. https://doi.org/10.1016/j.jnoncrysol.2012.07.029.

[82] T. Gao, Z. Zhang, Y. Li, Y. Song, H. Rong, X. Zhang, Solid-state reaction induced defects in multi-walled carbon nanotubes for improving microwave absorption properties, J. Mater. Sci. Technol. 108 (2022) 37–45. https://doi.org/10.1016/j.jmst.2021.08.051.

[83] R.G. Hoagland, S.J. Fensin, Signatures of the effects of defects on the bulk moduli of crystalline solids, Comput. Mater. Sci. 198 (2021) 110705. https://doi.org/10.1016/j.commatsci.2021.110705.

[84] A. Dasadia, V. Bhavsar, Growth, structure, electrical and optical properties of transition metal chalcogenide crystals synthesized by improved chemical vapor transport technique for semiconductor technologies, Prog. Cryst. Growth Charact. Mater. 68 (2022) 100578. https://doi.org/10.1016/j.pcrysgrow.2022.100578.

[85] H. Salehi Najafabadi, M.A. Meier, G.A. Hallock, Charge carrier transport and electrical response by driving band gap modulation in semiconductors, Appl. Mater. Today. 29 (2022) 101608. https://doi.org/10.1016/j.apmt.2022.101608.

[86] S. Yu, C.J. Kousseff, C.B. Nielsen, n-Type semiconductors for organic electrochemical transistor applications, Synth. Met. 293 (2023) 117295. https://doi.org/10.1016/j.synthmet.2023.117295.

[87] J. Yoshinobu, Physical properties and chemical reactivity of the buckled dimer on Si(100), Prog. Surf. Sci. 77 (2004) 37–70. https://doi.org/10.1016/j.progsurf.2004.07.001.

[88] S. Abroug, F. Saadallah, N. Yacoubi, Determination of doping effects on Si and GaAs bulk samples properties by photothermal investigations, Phys. B Condens. Matter. 400 (2007) 163–167. https://doi.org/10.1016/j.physb.2007.07.003.

[89] J. Zheng, Y. Zhou, Y. Zhang, L. Li, Y. Zhang, C-V characteristics of piezotronic metal-insulator-semiconductor transistor, Sci. Bull. 65 (2020) 161–168. https://doi.org/10.1016/j.scib.2019.11.001.

[90] S. Kettemann, Towards a comprehensive theory of metal–insulator transitions in doped semiconductors, Ann. Phys. (N. Y). 456 (2023) 169306. https://doi.org/10.1016/j.aop.2023.169306.

[91] Y. Poplavko, Semiconductors, Chapter 8, 2019. https://doi.org/10.1016/B978-0-12-815780-0.00008-6.

[92] Balkanski, M. and Wallis, R.F. (2000) Semiconductor Physics and Applications. Oxford University Press, New York

[93] S.S. Rozhkov,Optical-phonon emission by electrons and envelope electromagnetic solutions in semiconductors,Physics Letters A,Volume 146, Issue 9,
(1990), 496-501,0375-9601. https://doi.org/10.1016/0375-9601(90)90393-3.

[94] Y.S. Choi, J.B. Kim, J.G. Han, Optical absorption spectroscopy of facing targets and conventional magnetron sputtering during process of Al-doped ZnO films, Surf. Coatings Technol. 254 (2014) 371–375. https://doi.org/10.1016/j.surfcoat.2014.06.046.

[95] M. Sun, H. Liu, Z. Sun, W. Li, Donor-acceptor codoping effects on tuned visible light response of TiO_2, J. Environ. Chem. Eng. 8 (2020) 104168. https://doi.org/10.1016/j.jece.2020.104168.

[96] M. Frumar, B. Frumarova, T. Wagner, Amorphous and Glassy Semiconducting Chalcogenides, Compr. Semicond. Sci. Technol. 1–6 (2011) 206–261. https://doi.org/10.1016/B978-0-44-453153-7.00122-X.

[97] I. Hassani Nia, M. Rezaei, R. Brown, S.J. Jang, A. Turay, V. Fathipour, H. Mohseni, Efficient luminescence extraction strategies and anti-reflective coatings to enhance optical refrigeration of semiconductors, J. Lumin. 170 (2016) 841–854. https://doi.org/10.1016/j.jlumin.2015.08.051.

[98] C. Lv, Q. Zhang, Y. Zhang, T. Pang, W. Xiang, Luminescence from metal-oxide-semiconductor devices with Eu^{3+}-doped CeO_2 films on silicon: From broadband to monochromatic emission, J. Lumin. 263 (2023) 119976. https://doi.org/10.1016/j.jlumin.2023.119976.

[99] T. Ohtake, S. Hijii, N. Sonoyama, T. Sakata, Electrochemical luminescence of n-type ZnO semiconductor electrodes doped with rare earth metals under the anodic polarization, Appl. Surf. Sci. 253 (2006) 1753–1757. https://doi.org/10.1016/j.apsusc.2006.03.008.

[100] Balzani, V., Credi, A., and Venturi, M.(2008) Photochemical conversion of
solar energy. ChemSusChem, 1, 26–58. https://doi.org/10.1002/cssc.200700087

[101] I.Y.Y. Bu, Sol-gel production of p-type ZnO thin film by using sodium doping, Superlattices Microstruct. 96 (2016) 59–66. https://doi.org/10.1016/j.spmi.2016.05.011.

[102] L. Fadillah, B. Soegijono, S. Budiawanti, I. Mudzakir, Fabrication and characterization of ZnO and Li doped ZnO by a sol-gel method, AIP Conf. Proc. 1862 (2017) 0–4. https://doi.org/10.1063/1.4991157.

[103] T. Chitradevi, A. Jestin Lenus, N. Victor Jaya, Structure, morphology and luminescence properties of sol-gel method synthesized pure and Ag-doped ZnO nanoparticles, Mater. Res. Express. 7 (2019). https://doi.org/10.1088/2053-1591/ab5c53.

[104] N.R. Aswathy, J.J. Varghese, S.R. Nair, R.V. Kumar, Structural, optical, and magnetic properties of Mn-doped NiO thin films prepared by sol-gel spin coating, Mater. Chem. Phys. 282 (2022) 125916. https://doi.org/10.1016/j.matchemphys.2022.125916.

[105] P. Ni, B. Chen, X. Wei, Effects of annealing temperatures on energy storage performance of sol-gel derived $(Ba_{0.95},Sr_{0.05})(Zr_{0.2},Ti_{0.8})O_3$ thin films, Ceram. Int. (2022). https://doi.org/10.1016/j.ceramint.2022.03.167.

[106] S.I. Dorovskikh, D.D. Klyamer, A.M. Makarenko, K. V. Zherikova, A.E. Turgambaeva, Y. V. Shevtsov, D.B. Kalnyi, I.K. Igumenov, N.B. Morozova, The comprehensive study of thermal properties of tris(2,2,6,6-tetramethyl-3,5-heptanedionato)cobalt(III) related to the chemical vapor deposition of Co-oxide based thin film materials, Vacuum. 199 (2022) 110969. https://doi.org/10.1016/j.vacuum.2022.110969.

[107] T.I. Alanazi, Results in Physics Current spray-coating approaches to manufacture perovskite solar cells, Results Phys. 44 (2023) 106144. https://doi.org/10.1016/j.rinp.2022.106144.

[108] L. Liu, X. Yan, L. Li, J. Su, S. Ramakrishna, Y. Long, W. Han, Preparation of high-performance graphene materials by adjusting internal micro-channels using a combined electrospray/electrospinning technique, J. Alloys Compd. 940 (2023) 168882. https://doi.org/10.1016/j.jallcom.2023.168882.

[109] N.B. Patil, A.R. Nimbalkar, M.G. Patil, ZnO thin film prepared by a sol-gel spin coating technique for NO_2 detection, Mater. Sci. Eng. B. 227 (2018) 53–60. https://doi.org/10.1016/j.mseb.2017.10.011.

[110] G.R. Khan, R.A. Dar, Smart interplay of reaction parameters in sol-gel protocols of ZnO nanocrystallites, Mater. Sci. Eng. B. 267 (2021) 115110. https://doi.org/10.1016/j.mseb.2021.115110.

[111] A. Erol, S. Okur, B. Comba, Ö. Mermer, M.Ç. Arikan, Humidity sensing properties of ZnO nanoparticles synthesized by sol-gel process, Sensors Actuators, B Chem. 145 (2010) 174–180. https://doi.org/10.1016/j.snb.2009.11.051.

[112] J. Budida, K. Srinivasan, Review of thin film deposition and techniques, Mater. Today Proc. (2023) 4–7. https://doi.org/10.1016/j.matpr.2023.05.004.

[113] I. Saoula, C. Siad, A. Ouahab, N. Allag, A. Chala, S. Rahmane, S. Marmi, N. Saheb, Synthesis and properties of alkaline earth elements (Ca, Sr, and Ba) doped SnO_2 thin films, Opt. Mater. (Amst). 145 (2023). https://doi.org/10.1016/j.optmat.2023.114372.

[114] N. Calisi, E. Galvanetto, F. Borgioli, S.M. Martinuzzi, T. Bacci, S. Caporali, Thin films deposition of fully inorganic metal halide perovskites: A review, Mater. Sci. Semicond. Process. 147 (2022) 106721. https://doi.org/10.1016/j.mssp.2022.106721.

[115] D. Perednis, L.J. Gauckler, Thin film deposition using spray pyrolysis, J. Electroceramics. 14 (2005) 103–111. https://doi.org/10.1007/s10832-005-0870-x.

[116] C. Guild, S. Biswas, Y. Meng, T. Jafari, A.M. Gaffney, S.L. Suib, Perspectives of spray pyrolysis for facile synthesis of catalysts and thin films: An introduction and summary of recent directions, Catal. Today. 238 (2014) 87–94. https://doi.org/10.1016/j.cattod.2014.03.056.

[117] E. Tovar-Martinez, J.A. Moreno-Torres, J. V. Cabrera-Salazar, M. Reyes-Reyes, L.F. Chazaro-Ruiz, R. López-Sandoval, Synthesis of carbon nano-onions doped with nitrogen using spray pyrolisis, Carbon N. Y. 140 (2018) 171–181. https://doi.org/10.1016/j.carbon.2018.08.056.

[118] G. Martínez-Saucedo, M. Ugalde-Reygadas, J.J.A. Peña, G. Lastra-Medina, J. Márquez-Marín, G. Torres-Delgado, R. Castanedo-Pérez, I.R. Chávez-Urbiola, Non-enzymatic glucose sensor using nanostructured copper oxide thin films deposited by spray pyrolysis, Surfaces and Interfaces. 37 (2023). https://doi.org/10.1016/j.surfin.2023.102702.

[119] L. Filipovic, S. Selberherr, G.C. Mutinati, E. Brunet, S. Steinhauer, A. Köck, J. Teva, J. Kraft, J. Siegert, F. Schrank, Microelectronic Engineering Methods of simulating thin film deposition using spray pyrolysis techniques, Microelectron. Eng. 117 (2014) 57–66. https://doi.org/10.1016/j.mee.2013.12.025.

[120] A. Nakaruk, C.C. Sorrell, Conceptual model for spray pyrolysis mechanism : fabrication and annealing of titania thin films, 7 (2010) 665–676. https://doi.org/10.1007/s11998-010-9245-6.

[121] F. Solis-pomar, A. Fundora, J.L. Menchaca, Study of the structural properties of nanostructured PbS thin films deposited by RF sputtering at room temperature, 2018 Mater. Res. Express, 5 ,106403, (2000). https://doi.org/0.1088/2053-1591/aadac0

[122] C.H. Ng, J. Rao, J. Nicholls, The role of PVD sputtered PTFE and Al_2O_3 thin films in the development of damage tolerant coating systems, J. Mater. Res. Technol. 9 (2020) 675–686. https://doi.org/10.1016/j.jmrt.2019.11.009.

[123] J. Gutpa, H. Shaik, K. Naveen Kumar, S.A. Sattar, PVD techniques proffering avenues for fabrication of porous tungsten oxide (WO_3) thin films: A review, Mater. Sci. Semicond. Process. 143 (2022) 106534. https://doi.org/10.1016/j.mssp.2022.106534.

[124] D.T. Gawne, Y. Bao, J. Gao, C. Zubizarreta, J. Goikoetxea, J. Barriga, Thin film performance from hybrid PVD-powder coating process, Surf. Coatings Technol. 236 (2013) 388–393. https://doi.org/10.1016/j.surfcoat.2013.10.019.

[125] S. Ferreira, P. Duarte, F.A. Almeida, R.F. Silva, Bilayered coatings of BN/diamond grown on Si_3N_4 ceramic substrates, Diam. Relat. Mater. 20 (2011) 464–467. https://doi.org/10.1016/j.diamond.2011.02.009.

[126] I. Apostol, A. Mahajan, C.J.A. Monty, K. Venkata Saravanan, Nanostructured $MgTiO_3$ thick films obtained by electrophoretic deposition from nanopowders prepared by solar PVD, Appl. Surf. Sci. 358 (2015) 641–646. https://doi.org/10.1016/j.apsusc.2015.09.060.

[127] Y. Demirhan, H. Koseoglu, F. Turkoglu, Z. Uyanik, M. Ozdemir, G. Aygun, L. Ozyuzer, The controllable deposıtıon of large area roll-to-roll sputtered ito thın fılms for photovoltaıc applıcatıons, Renew. Energy. 146 (2020) 1549–1559. https://doi.org/10.1016/j.renene.2019.07.038.

[128] D. Peeters, D.H. Taffa, M.M. Kerrigan, A. Ney, N. Jöns, D. Rogalla, S. Cwik, H.W. Becker, M. Grafen, A. Ostendorf, C.H. Winter, S. Chakraborty, M. Wark, A. Devi, Photoactive Zinc Ferrites Fabricated via Conventional CVD Approach, ACS Sustain. Chem. Eng. 5 (2017) 2917–2926. https://doi.org/10.1021/acssuschemeng.6b02233.

[129] A.M. Alotaibi, P. Promdet, G.B. Hwang, J. Li, S.P. Nair, S. Sathasivam, A. Ka, C.J. Carmalt, I.P. Parkin, Zn and N Codoped TiO_2 Thin Films: Photocatalytic and Bactericidal Activity, (2021). https://doi.org/10.1021/acsami.1c00304.

[130] A. George, D.R. A, Q. Yang, Gas sensing performance of Tungsten doped V2O5 nanorod thin-films deposited by hot filament CVD combined with DC sputtering, Sensors Actuators B Chem. 394 (2023) 134371. https://doi.org/10.1016/j.snb.2023.134371.

[131] H.Y. Liu, Y.J. Liao, H.Y. Wu, Mist CVD deposited amorphous InSnZnO thin films with different nitrogen/oxygen ratios carrier gases and their applications to thin-film transistors, Ceram. Int. 48 (2022) 28790–28799. https://doi.org/10.1016/j.ceramint.2021.12.287.

[132] R. Mauchauffé, J. Kim, D. hyun Kim, S. Lee, M. Kwon, S.Y. Moon, UV-Shielding TiO_2 thin film deposition on flexible and heat-labile substrate using an open-air hybrid CVD/Plasma method, Vacuum. 192 (2021) 1–9. https://doi.org/10.1016/j.vacuum.2021.110424.

[133] S. Das, S. Guha, R. Ghadai, A. Sharma, Influence of nitrogen gas over microstructural, vibrational and mechanical properties of CVD Titanium nitride (TiN) thin film coating, Ceram. Int. 47 (2021) 16809–16819. https://doi.org/10.1016/j.ceramint.2021.02.254.

[134] T. Imrich, R. Zazpe, H. Krýsová, Paušová, F. Dvorak, J. Rodriguez-Pereira, J. Michalicka, O. Man, J.M. Macak, M. Neumann-Spallart, J. Krýsa, Protection of hematite photoelectrodes by ALD-TiO_2 capping, J. Photochem. Photobiol. A Chem. 409 (2021). https://doi.org/10.1016/j.jphotochem.2020.113126.

[135] B. Ku, Y. Shin, Y. Lee, T. Kim, C. Choi, Applied Surface Science Improved ferroelectric characteristics of ALD lanthanum-doped hafnium oxide thin film by controlling post-cooling time, Appl. Surf. Sci. 599 (2022) 153905. https://doi.org/10.1016/j.apsusc.2022.153905.

[136] Y. Choi, H. Park, N. Lee, B. Kim, J. Lee, G. Lee, H. Jeon, Deposition of the tin sulfide thin films using ALD and a vacuum annealing process for tuning the phase transition, J. Alloys Compd. 896 (2022) 162806. https://doi.org/10.1016/j.jallcom.2021.162806.

[137] J. Rodríguez-López, R. Rangel, D. Berman-Mendoza, A. Ramos-Carrazco, J.J. Alvarado, Evaluating the response of nitrogen implantation in ZnO ALD thin films and their photocatalytic assessment, J. Photochem. Photobiol. A Chem. 433 (2022). https://doi.org/10.1016/j.jphotochem.2022.114211.

[138] J.A. Oke, T. Jen, Atomic layer deposition and other thin film deposition techniques : from principles to film properties, J. Mater. Res. Technol. 21 (2022) 2481–2514. https://doi.org/10.1016/j.jmrt.2022.10.064.

[139] N. Al-Aisaee, M. Alhabradi, X. Yang, M. Alruwaili, S. Rasul, A.A. Tahir, Fabrication of WO_3/Fe_2O_3 heterostructure photoanode by PVD for photoelectrochemical applications, Sol. Energy Mater. Sol. Cells. 263 (2023). https://doi.org/10.1016/j.solmat.2023.112561.

[140] G. Gupta, R.K. Tyagi, S.K. Rajput, P. Saxena, A. Vashisth, S. Mehndiratta, PVD based thin film deposition methods and characterization / property of different compositional coatings - A critical analysis, Mater. Today Proc. 38 (2020) 259–264. https://doi.org/10.1016/j.matpr.2020.07.132.

[141] P.C. Ricci, N. Laidani, D. Chiriu, M. Salis, C.M. Carbonaro, R. Corpino, ALD growth of metal oxide on carbon nitride polymorphs, Appl. Surf. Sci. 456 (2018) 83–94. https://doi.org/10.1016/j.apsusc.2018.06.021.

[142] D. Lincot, Electrodeposition of semiconductors, Thin Solid Films, 487 (2005) 40–48. https://doi.org/10.1016/j.tsf.2005.01.032.

[143] W. He, H. Zhang, Y. Zhang, M. Liu, X. Zhang, F. Yang, Electrodeposition and Characterization of CuTe and Cu_2Te Thin Films, Journal of Nanomaterials, 2015 (2015). https://doi.org/10.1155/2015/240525

[144] T. Yang, Y. Ding, C. Li, N. Yin, X. Liu, P. Li, Potentiostatic and galvanostatic two-step electrodeposition of semiconductor Cu_2O films and its photovoltaic application, J. Alloys Compd. 727 (2017) 14–19. https://doi.org/10.1016/j.jallcom.2017.08.123.

[145] A.W. Black, W. Zhang, Y.J. Noori, G. Reid, P.N. Bartlett, Temperature effects on the electrodeposition of semiconductors from a weakly coordinating solvent, J. Electroanal. Chem. 944 (2023) 117638. https://doi.org/10.1016/j.jelechem.2023.117638.

[146] X. Ren, C.H. Jiang, D.D. Li, L. He, Fabrication of ZnO nanotubes with ultrathin wall by electrodeposition method, Mater. Lett. 62 (2008) 3114–3116. https://doi.org/10.1016/j.matlet.2008.01.112.

[147] J. Wu, W. Zheng, Y. Chen, Definition of photocatalysis: Current understanding and perspectives, Curr. Opin. Green Sustain. Chem. 33 (2022) 100580. https://doi.org/10.1016/j.cogsc.2021.100580.

[148] S. Wang, D. Su, Y. Zhu, C. Lu, T. Zhang, Materials & Design The state-of-the-art review on rational design for cavitation assisted photocatalysis, Mater. Des. 234 (2023) 112377. https://doi.org/10.1016/j.matdes.2023.112377.

[149] B. Zeng, W. Sheng, F. Huang, K. Zhang, K. Xiong, X. Lang, Cooperative photocatalysis of hafnium-based metal–organic framework and TEMPO for selective oxidation of sulfides, Chem. Eng. J. 474 (2023) 145559. https://doi.org/10.1016/j.cej.2023.145559.

[150] T.H. Lai, K.I. Katsumata, Y.J. Hsu, In situ charge carrier dynamics of semiconductor nanostructures for advanced photoelectrochemical and photocatalytic applications, Nanophotonics. 10 (2020) 777–795. https://doi.org/10.1515/nanoph-2020-0472.

[151] Jenny Schneider, Detlef W. Bahnemann, The Journal of Physical Chemistry Letters, 2013, 4 (20), 3479-3483 ,https://doi.org/10.1021/jz4018199

[152] N. Serpone, A. V. Emeline, S. Horikoshi, V.N. Kuznetsov, V.K. Ryabchuk, On the genesis of heterogeneous photocatalysis: A brief historical perspective in the period 1910 to the mid-1980s, Photochem. Photobiol. Sci. 11 (2012) 1121–1150. https://doi.org/10.1039/c2pp25026h.

[153] M.L. Satuf, R.J. Brandi, A.E. Cassano, O.M. Alfano, Quantum efficiencies of 4-chlorophenol photocatalytic degradation and mineralization in a well-mixed slurry reactor, Ind. Eng. Chem. Res. 46 (2007) 43–51. https://doi.org/10.1021/ie0604019.

[154] M. Buchalska, P. łabuz, Ł. Bujak, G. Szewczyk, T. Sarna, S. Maćkowski, W. Macyk, New insight into singlet oxygen generation at surface modified nanocrystalline TiO_2– the effect of near-infrared irradiation, J. Chem. Soc. Dalt. Trans. 42 (2013) 9468–9475. https://doi.org/10.1039/c3dt50399b.

[155] J.P. Kuczynski, B.H. Milosavijevic, J.K. Thomas, Effect of the synthetic preparation on the photochemical behavior of colloidal CdS, J. Phys. Chem. 87 (1983) 3368–3370. https://doi.org/10.1021/j100241a003.

[156] J. Liu, S. Zhang, W. Wang, H. Zhang, Photoelectrocatalytic principles for meaningfully studying photocatalyst properties and photocatalysis processes: From fundamental theory to environmental applications, J. Energy Chem. 86 (2023) 84–117. https://doi.org/10.1016/j.jechem.2023.06.038.

[157] T. Sakata, K. Hashimoto, M. Hiramoto, New aspects of electron transfer on semiconductor surface: Dye-sensitization system, J. Phys. Chem. 94 (1990) 3040–3045. https://doi.org/10.1021/j100370a056.

[158] X. Li, H. Hao, X. Lang, Molecular design of dye-TiO_2 assemblies for green light-induced photocatalytic selective aerobic oxidation of amines, J. Colloid Interface Sci. 581 (2021) 826–835. https://doi.org/10.1016/j.jcis.2020.07.115.

[159] T. Wu, T. Lin, J. Zhao, H. Hidaka, N. Serpone, TiO_2-assisted photodegradation of dyes. 9. Photooxidation of a squarylium cyanine dye in aqueous dispersions under visible light irradiation, Environ. Sci. Technol. 33 (1999) 1379–1387. https://doi.org/10.1021/es980923i.

[160] H. Irie, K. Sunada, K. Hashimoto, Recent developments in TiO_2 photocatalysis: Novel applications to interior ecology materials and energy saving systems, Electrochemistry. 72 (2004) 807–812. https://doi.org/10.5796/electrochemistry.72.807.

[161] Hiroshi Irie, Seitaro Washizuka, Kazuhito Hashimoto, Hydrophilicity on carbon-doped TiO_2 thin films under visible light,Thin Solid Films,510, 1–2,(2006),
21-25,0040-6090. https://doi.org/10.1016/j.tsf.2005.08.374.

[162] Y. Wei, Q. Wu, H. Meng, Y. Zhang, C. Cao, Recent advances in photocatalytic self-cleaning performances of TiO_2-based building materials, RSC Adv. 13 (2023) 20584–20597. https://doi.org/10.1039/d2ra07839b.

[163] Miyauchi, M.; Sunada, K.; Hashimoto, K. Antiviral Effect of Visible Light-Sensitive Cu_xO/TiO_2 Photocatalyst. Catalysts 2020, 10, 1093. https://doi.org/10.3390/catal10091093

[164] João Lincho, Adriana Zaleska-Medynska, Rui C. Martins, João Gomes, Nanostructured photocatalysts for the abatement of contaminants by photocatalysis and photocatalytic ozonation: An overview,Science of The Total Environment,837,(2022),155776, https://doi.org/10.1016/j.scitotenv.2022.155776.

[165] G. Veréb, L. Manczinger, G. Bozsó, A. Sienkiewicz, L. Forró, K. Mogyorósi, K. Hernádi, A. Dombi, Comparison of the photocatalytic efficiencies of bare and doped rutile and anatase TiO_2 photocatalysts under visible light for phenol degradation and *E. coli* inactivation, Appl. Catal. B Environ. 129 (2013) 566–574. https://doi.org/10.1016/j.apcatb.2012.09.045.

[166] K. Sunada, T. Watanabe, K. Hashimoto, Studies on photokilling of bacteria on TiO_2 thin film, J. Photochem. Photobiol. A Chem. 156 (2003) 227–233. https://doi.org/10.1016/S1010-6030(02)00434-3.

[167] D. Mitoraj, A. Jańczyk, M. Strus, H. Kisch, G. Stochel, P.B. Heczko, W. Macyk, Visible light inactivation of bacteria and fungi by modified titanium dioxide, Photochem. Photobiol. Sci. 6 (2007) 642–648. https://doi.org/10.1039/b617043a.

[168] K.J. Shieh, M. Li, Y.H. Lee, S. Der Sheu, Y.T. Liu, Y.C. Wang, Antibacterial performance of photocatalyst thin film fabricated by defection effect in visible light, Nanomedicine Nanotechnology, Biol. Med. 2 (2006) 121–126. https://doi.org/10.1016/j.nano.2006.04.001.

[169] R. Nakano, H. Ishiguro, Y. Yao, J. Kajioka, A. Fujishima, K. Sunada, M. Minoshima, K. Hashimoto, Y. Kubota, Photocatalytic inactivation of influenza virus by titanium dioxide thin film, Photochem. Photobiol. Sci. 11 (2012) 1293–1298. https://doi.org/10.1039/c2pp05414k.

[170] J. Krýsa, E. Musilová, J. Zita, Critical assessment of suitable methods used for determination of antibacterial properties at photocatalytic surfaces, J. Hazard. Mater. 195 (2011) 100–106. https://doi.org/10.1016/j.jhazmat.2011.08.009.

[171] J.R. Johnson, M.A. Kuskowski, T.J. Wilt, Systematic review: Antimicrobial urinary catheters to prevent catheter-associated urinary tract infection in hospitalized patients, Ann. Intern. Med. 144 (2006) 116–126. https://doi.org/10.7326/0003-4819-144-2-200601170-00009.

[172] L.E. Nicolle, Infections associated with urinary catheters, Clin. Infect. Dis. Second Ed. (2015) 722–727. https://doi.org/10.1017/CBO9781139855952.122.

[173] J. Sjollema, S.A.J. Zaat, V. Fontaine, M. Ramstedt, R. Luginbuehl, K. Thevissen, J. Li, H.C. van der Mei, H.J. Busscher, In vitro methods for the evaluation of antimicrobial surface designs, Acta Biomater. 70 (2018) 12–24. https://doi.org/10.1016/j.actbio.2018.02.001.

[174] P. Wu, D.W. Grainger, Drug/device combinations for local drug therapies and infection prophylaxis, Biomaterials. 27 (2006) 2450–2467. https://doi.org/10.1016/j.biomaterials.2005.11.031.

[175] R.G. Richards, T.F. Moriarty, T. Miclau, R.T. McClellan, D.W. Grainger, Advances in biomaterials and surface technologies, J. Orthop. Trauma. 26 (2012) 703–707. https://doi.org/10.1097/BOT.0b013e31826e37a2.

[176] D.W. Grainger, H.C. van der Mei, P.C. Jutte, J.J.A.M. van den Dungen, M.J. Schultz, B.F.A.M. van der Laan, S.A.J. Zaat, H.J. Busscher, Critical factors in the translation of improved antimicrobial strategies for medical implants and devices, Biomaterials. 34 (2013) 9237–9243. https://doi.org/10.1016/j.biomaterials.2013.08.043.

[177] M. Malone, D.M. Goeres, I. Gosbell, K. Vickery, S. Jensen, P. Stoodley, Approaches to biofilm-associated infections: the need for standardized and relevant biofilm methods for clinical applications, Expert Rev. Anti. Infect. Ther. 15 (2017) 147–156. https://doi.org/10.1080/14787210.2017.1262257.

[178] U. Iso, E. Del, D.U. Iso, Textiles. Determination of antibacterial activity of textile products (ISO 20743:2021), (2022).

[179] Antibacterial products- Test for antibacterial activity and efficacy.(JIS Z 2801:2010),(2010).

[180] A. Roosjen, H.J. Busscher, W. Norde, H.C. Van der Mei, Bacterial factors influencing adhesion of Pseudomonas aeruginosa strains to a poly(ethylene oxide) brush, Microbiology. 152 (2006) 2673–2682. https://doi.org/10.1099/mic.0.29005-0.

[181] V. Humblot, J.F. Yala, P. Thebault, K. Boukerma, A. Héquet, J.M. Berjeaud, C.M. Pradier, The antibacterial activity of Magainin I immobilized onto mixed thiols Self-Assembled Monolayers, Biomaterials. 30 (2009) 3503–3512. https://doi.org/10.1016/j.biomaterials.2009.03.025.

[182] L.G. Harris, S. Tosatti, M. Wieland, M. Textor, R.G. Richards, Staphylococcus aureus adhesion to titanium oxide surfaces coated with non-functionalized and peptide-functionalized poly(L-lysine)-grafted-poly(ethylene glycol) copolymers, Biomaterials. 25 (2004) 4135–4148. https://doi.org/10.1016/j.biomaterials.2003.11.033.

[183] T.F. Moriarty, D.W. Grainger, R.G. Richards, Challenges in linking preclinical anti-microbial research strategies with clinical outcomes for device-associated infections, Eur. Cells Mater. 28 (2014) 112–128. https://doi.org/10.22203/eCM.v028a09.

CHAPTER 2

Objetives

“Energy is one of humanity's greatest challenges. We are continuously looking for innovative solutions to address this issue and make energy sources cleaner and more efficient “

Yi Cui

2.1.General Objectives

Semiconducting oxides exhibit a diverse array of uses, particularly in the realm of surface functionalization, as has been seen. The primary objective of this thesis is to explore the functionalization of transparent glass surfaces through the use of semiconducting oxides, specifically TiO_2 or ZnO. This approach aims to impart novel features to these surfaces, including the capability to generate photocatalytic or antimicrobial effects.

The expected beneficial results focusing on the following objectives are as follows:

- Synthesis of these semiconductor oxides aims to enable their application on a glass substrate while preserving the optical properties of the substrates.
- Characterize structural, morphological and optical properties of the developed materials.
- Evaluation of the adhesion properties and alterations in the optical characteristics of a glass substrate subsequent to the application of semiconducting oxides.
- Investigate the photocatalytic characteristics of the novel developed transparent semiconductor oxides on glass substrates.
- Evaluation of the antibacterial efficacy of light-irradiated transparent semiconductor oxides that were deposited onto glass substrates.

In order to accomplish these aims, the methodology entails the division of the thesis project into distinct stages, with the aim of facilitating the development of transparent semiconducting oxides on glass surfaces. This approach is intended to yield novel features for these substrates.

Stages are defined as, synthesise the powder of these semiconductors to generate transparent thin films on glass by analysing the final properties of the substrate, then evaluate the new properties obtained by the substrate such as the photocatalytic property or the bactericidal property.

These transparent semiconductor oxides must possess certain characteristics, including:

- Reduced particle size (<100 nm) and thin deposition thickness (<300 nm).
- High absorbance in the UV (<350 nm) and/or visible range (380-780 nm) and optical band gap > 3 eV.
- High transparency as a deposited layer (>80% transmittance).
- Capacity to generate reactive oxygen species (ROS) when irradiated by different types of light.
- Assess bactericidal and/or bacteriostatic properties through proliferation assays and viability analysis for different bacterial groups.

CHAPTER 3

ZnO/Ag Nanocomposites with Enhanced Antimicrobial Activity

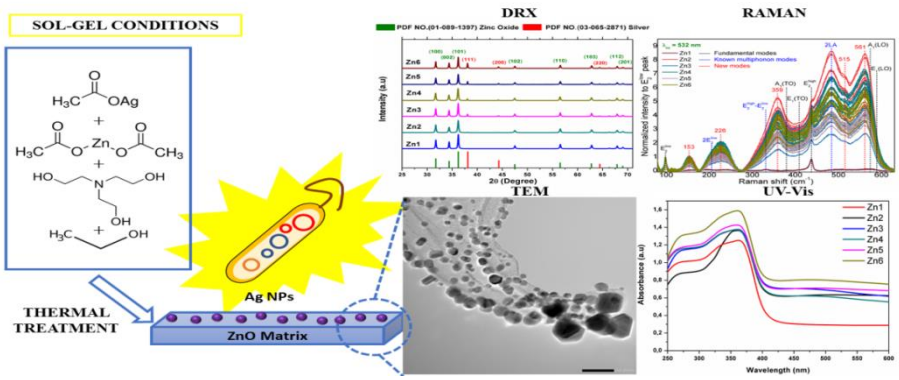

J.G. Cuadra, L. Scalschi, B. Vicedo, M. Guc, V. Izquierdo-roca, S. Porcar, D. Fraga, J.B. Carda, applied sciences ZnO / Ag Nanocomposites with Enhanced Antimicrobial Activity, (2022) 1–13. https://doi.org/10.3390/app12105023.

"There is a wide range of two-dimensional materials with astonishing properties waiting to be discovered and exploited"
"Konstantin Noselov"

Abstract: In this study, ZnO/Ag nanocomposites were synthesized using a facile chemical route involving metallic precursors of zinc acetate dehydrate and silver acetate, and dissolving the two metallic precursors in EtOH. The final concentration of the solution was 0.4 M. The different nanocomposites were synthesized using different atomic percentages of silver to compare the amount of silver nanoparticles with the bactericidal power of the nanocomposites. They were prepared at concentrations of 0, 1, 3, 5, 7, and 10 at%. The as-prepared nanocomposites were characterized using X-ray diffraction (XRD), scanning electron microscopy (SEM) and scanning transmission electron microscopy (STEM) to study their structural and morphological properties. SEM showed that there is a clear effect of Ag on the size of the ZnO particles, since when silver percentages of 1 at% are included, the grain size obtained is much smaller than that of the ZnO synthesis. The effect is maintained for 3, 5, 7, and 10 at% silver. Transmission electron microscopy (TEM) compositional mapping confirms the presence of spherical nanoparticles in the synthesized samples. The size of the nanoparticles ranges from about 10 to about 30 nm. In addition, UV-Vis and Raman spectroscopy were performed to obtain structural details. The different samples show an increase in the absorption in the visible range due to the incorporation of the silver NPs. Measurement of the antimicrobial activity was tested against *Staphylococcus aureus (S. aureus)* and *Escherichia coli (E. coli)* It is shown that zinc oxide has bactericidal power for these two groups of bacteria and also that when it is used together with silver NP, this effect improves, eliminating more than 90% of inoculated bacteria.

3.1. Introduction

Metals have been used as antimicrobial agents since ancient times. For example, mercury, silver, copper, zinc, and arsenic were used to cure infections. Zinc and copper are associated with the mechanism of pathogen killing in eukaryotes, where oxidative stress is used to kill the engulfed microbe. Metals like gold, silver and mercury are very toxic at low concentrations to bacteria and they have broad-spectrum antibacterial actions [1,2].

Safety interest related to the drug-resistant microbes and continuing emphasis on health care costs have focused on replacing the traditional antimicrobial compounds or found another alternative [3]. Nowadays, nanotechnology has become an extremely powerful and versatile nanoweapon to destroy this particular issue that has been increasing day by day. Microbes find survival extremely difficult for survival towards nanoparticles as they target large bacterial components, conversely the mechanistic action of antibiotics [4].

Besides, nano-hybrid crystals especially metal-oxide have caused special attention as they combine the properties of the constituent elements producing a more deep and synergistic effect [5]. In recent years, zinc oxide (ZnO) has been recognized as a safe material by the U.S Food and Drug Administration [(21CFR182.8991) (FDA, 2011)], and antibacterial activity of ZnO NPs has received significant interest worldwide particularly by the implementation of nanotechnology to synthesize particles in the nanometer region [6].

ZnO NPs show great photocatalytic activity as it is an n-type II-VI semiconductor with a relatively large bandgap ~3.3 eV of and high excitation binding energy (~ 60 meV) at room temperature [7], and it has good chemical stability as well as high-temperature resistance ~ 1950ºC in the hexagonal wurtzite structure [8].

ZnO holds high optical absorption in the UVA (315-400 nm) and UVB (280-315 nm) regions which is advantageous in antibacterial response because this feature significantly promotes the interaction on ZnO with bacterial [9]. ZnO is a more efficient photocatalyst than titanium dioxide (TiO_2) under visible light irradiation due to its quantum efficiency, lower cost of production and more biocompatibility than TiO_2 [10].

The photocatalytic activity can be modulated by allowing absorption in the visible range introducing different types of dopants (metals or non-metals) [11,12]. Doping ZnO with noble metals like gold (Au) and silver (Ag) has been reported to increase the photocatalytic activity of ZnO because of improved charge separation and reduction in electron-hole recombination in ZnO [13]. The optical vibration of surface plasmon in metal nanoparticles enable absorption in the visible range (380-750 nm) and improve the photocatalytic activity of these metal-semiconductor composites under visible light [14].

Ag nanoparticles have been investigated by many researchers for this important role in a wide array of pathogens, particularly multi-resistant pathogens which are difficult to treat with available antibiotics [15].

The most used bacteria to test the bactericidal effect of nanoparticles of different compositions are *S. aureus* and *E. coli* [3,16,17]. *S. aureus* is a GRAM positive bacterium, with a high content of peptidoglycan in the cell wall. It is able to survive in variable environmental conditions, such as low-pH or starvation.

It is considered an important human pathogen that can cause severe skin infections or internal infections when it breaks through the defensive barriers. *E. coli* is a GRAM negative bacterium, whose cell wall has a totally different structure from GRAM positive bacteria since it is surrounded by a lipidic membrane on the outside. It is a bacterium that indicates faecal contamination, as it is present in the intestinal microbiota.Although many strains are harmless, there are highly dangerous species such as enterotoxigenic and enterohemorrhagic varieties. Both bacteria can acquire resistance to antibiotics becoming this way more hazardous [17]. Therefore, controlling the growth of these bacteria is important for human health.

The effect that Ag NPs might have on bacteria has been studied in different works, either to enhance the effect of some antibiotics [18] or against selected Gram-negative foodborne pathogens [19] indicate that different methods of synthesis of NPs, as well as different methods to determine the antimicrobial activity, are used, hardening the comparison between the results obtained by different authors. The present work aims to determine the ability of the Ag-NP to inhibit or to reduce bacterial growth by using a novel synthesis based on sol gel methodology for the generation of silver nanoparticles on a zinc oxide surface.

3.2. Results and discussion

3.2.1. Synthesis of ZnO/Ag Nanocomposites

ZnO/Ag nanocomposites were prepared by the sol-gel method. The solutions were prepared using metallic precursors of zinc acetate dihydrate ($C_4H_6O_4Zn•2H_2O$; Sig-ma-Aldrich) and silver acetate ($C_2H_3AgO_2$, with 99% purity, Sigma-Aldrich).

These ZnO/Ag nanocomposites were prepared with concentrations of 0, 1, 3, 5, 7, and 10 at% of silver, labeled Zn1, Zn2, Zn3, Zn4, Zn5, and Zn6. The concentration of the final solutions was 0.4 M.

The first step of sol-gel synthesis is based on dissolving the two metallic precursors in 20 mL of ethanol (EtOH, Scharlau, Sentmenat, Spain) using a magnetic stirrer at room temperature (25 °C). After preparation, triethanolamine ($C_6H_{15}NO_3$, 99%, Acros Organics) was added to the solution as a reducing/precipitation agent. After approximately 30 min stirring at room temperature, a dense white gel was formed. We let it dry for 30 min at room temperature before the gel was calcined at 600 °C for 1 h in a muffle furnace to obtain white-colored nanopowders as the final product (Figure 3.1).

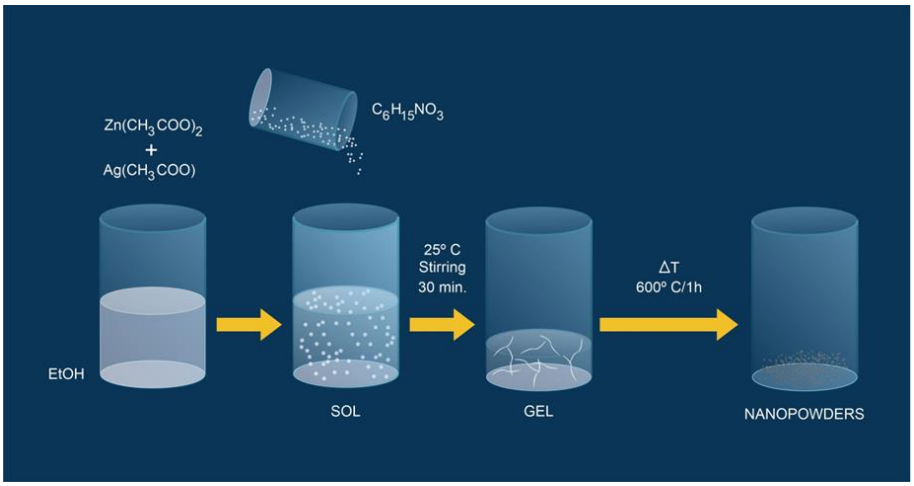

Figure 3.1 The synthesis of the antimicrobial ZnO/Ag nanocomposites.

3.2.2. Characterization

The crystal structures of the different ZnO/Ag nanocomposite samples were studied using X-ray diffraction (XRD) measurements. To do so, an X-ray diffractometer (D4 Endeavor, Burker-ASX) equipped with a Cu Kα radiation source was used. Data was collected by step-scanning from 10° to 80° with a step size of 0.05°/2θ and 5 s counting time per step.

The morphology and the size of the ZnO/Ag nanocomposites were observed using a JEOL JEM-1010 200 kV Field Emission Transmission Electron Microscope (TEM 200) equipped with a JEOL EM-24830FLASH digital camera with a CMOS sensor, offering a resolution of 2 k × 2 k. The maximum resolution achieved was 0.23 nm.

The microscope was also equipped with a STEM DF/BF image acquisition system with a resolution of 1 nm and an Aztec TEM Ultim Max microanalysis system from Oxford with a drift silicon sensor without a window of 80 mm^2 and a resolution of 127 eV for the Mn Kα line.

Raman scattering measurements were performed using a Hobiba Jobin-Yvon FHR-640 monochromator coupled with a CCD detector in backscattering configuration through a specific probe designed at the Catalonia Institute for Energy Research (IREC). The spectra were excited by gas (325 nm) with a density power of ~10 W/cm^2. Calibration of the spectral position was performed by imposing the main peak of single-crystalline Si to 520 cm^{-1}.

For each sample, the measurements were carried out at 9 points with a laser spot diameter of ~70 μm, which made it possible to exclude the local variations due to different crystalline orientations of the grains and possible inhomogeneities between specific grains. UV–visible (UV-Vis) diffuse reflectance spectroscopy of the samples was performed to study the optical properties of the ZnO/Ag nanocomposites using a CARY 500 SCAN VARIAN spectrophotometer in the 220–600 nm range. $BaSO_4$ was used as a reference

3.2.3. Bactericidal Test of ZnO/Ag Nanocomposites

The antimicrobial effect of the ZnO/Ag nanocomposites was tested against the *S. aureus* ATCC 29213 and the *E. coli* NCIMB 9484 strains, both from the Spanish Type Culture Collection (CECT).

The strains were pre-cultivated on Luria Bertani (LB) agar plates at 37 °C to obtain the inoculum. After 24 h, the bacteria were harvested in sterilized $MgSO_4$ (10 mM). LB supplemented with ZnO or ZnO/Ag nanocomposites was used in the bacterial growth assays.

The growth assays were carried out in a Multiskan FCMicroplate Photometer (Thermo Scientific, Waltham, MA, USA) with a total volume of 200 μL in microlitre wells using an initial bacterial density of 106 cfu mL^{-1} of *S. aureus* and 105 cfu mL^{-1} of *E. coli*. Bacterial growth was incubated at 37 °C with continuous agitation and monitored by measuring the optical density every 10 min with periodic shaking for 24 h. The results were printed out as growth curves.

To test whether the applied nanocomposites had an antimicrobial or bacteriostatic effect, live and dead cell quantification was used. The proportion of living vs. dead cells was quantified using the fluorescent LIVE/DEAD BacLight Bacterial Viability Kit, L13152 (Molecular Probes, Invitrogen, Paisley, UK).

For live and dead cell quantification, 50 microL of bacterial suspension was mixed with 25 microL of each of the two components of the LIVE/ DEAD BacLight kit and incubated in the dark for 20 min. Then, the ratio of live/dead cells was determined by flow cytometric analysis. Samples were analyzed on a Becton Dickinson FACScan flow cytometer using the CellQuest software, which was also used to determine the percentage of live/dead cells. SYTO9 (Live) was excited at 480 nm and fluorescence was analyzed at 500 nm, whereas Propidium Iodide (Dead) was excited at 490 nm and fluorescence analyzed at 635 nm.

Statistical analysis was carried out using a one-way analysis of variance in the Statgraphics-plus software of Windows V.5 (Statistical Graphics Corp., Rockville, MD, USA). The means were expressed with standard errors and compared using a Fisher's least-significant difference test at the 95% confidence interval. Each experiment consisted of eight technical repetitions which were repeated three times.

3.2.4. XRD Analysis

The crystalline behavior and structural properties of ZnO/Ag nanocomposites were revealed by powder XRD measurements. XRD patterns of the samples were prepared by means of concentrations of 0, 1, 3, 5, 7, and 10 at% of silver are shown in Figure 3.2. The diffraction patterns obtained were analyzed by X'Pert High Score Plus software.

The diffraction peaks are all very sharp, which reflects a polycrystalline with good crystallinity. It was observed that when the Ag at% is raised, the intensity of the diffraction peaks corresponding to the cubic structure of Ag NPs (PDF NO. 03-065-2871, a = 4.09 Å) increases the crystallinity.

The three diffraction peaks at 2θ of 38.1°, 44.3°, and 64.4° correspond to the crystal planes of (100), (200), and (220), respectively. ZnO peaks corresponding to a hexagonal wurtzite structure (PDF NO. 01-080-0074, a = 3.25 Å, c = 5.21 Å) remained stable for all the concentrations.

The eight diffraction peaks belonging to ZnO were at 2θ of 31.7°, 34.3°, 36.2°, 47.4°, 56.5°, 62.7°, 67.8°, and 68.9°, which correspond to the crystal planes of (100), (002), (101), (102), (110), (103), (112), and (201), respectively.

However, the XRD patterns indicate the formation of separate phases, a hexagonal wurtzite structure for ZnO, and a cubic structure for Ag NPs. The formation of these separate phases can be seen when the atomic percentage of silver surpassed a value of 3%. No other peaks were identified, suggesting the purity of the synthesized sample.

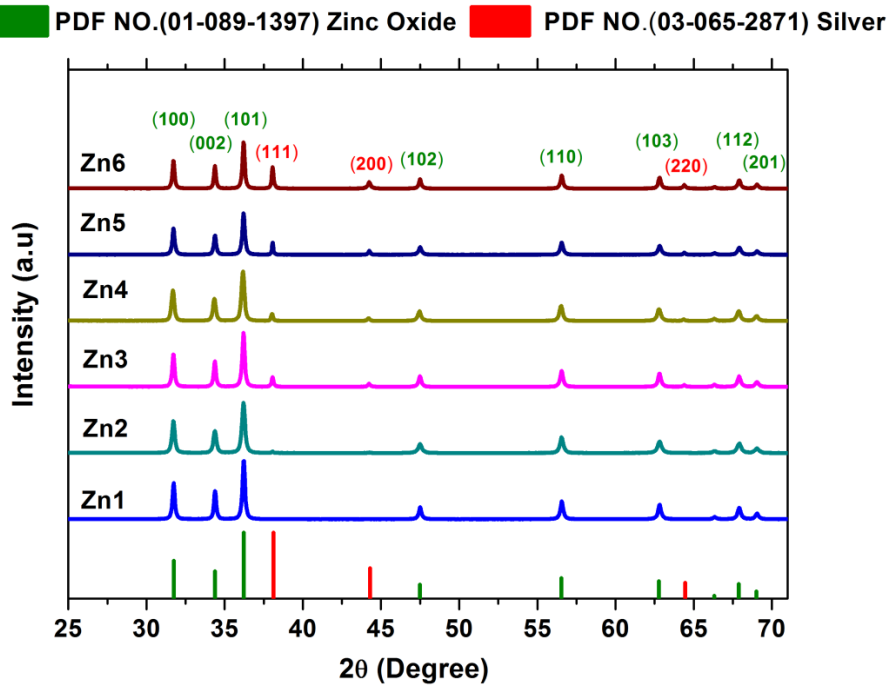

Figure 3.2 XRD patterns for the different silver concentrations of the nanocomposites (Zn1, Zn2, Zn3, Zn4, Zn5, and Zn6).

3.2.5. Morphological, Size, and Compositional Analysis of ZnO/Ag Nanocomposites

The SEM images of the synthesized ZnO/Ag nanocomposites are shown in Figure 3.3. Figure 3.3a displays the agglomerated particles of pure ZnO. Figure 3.3a–f shows the samples prepared by means of concentrations of 0, 1, 3, 5, 7, and 10 at% of silver.

The effect of Ag on the size of ZnO particles is clear. In Figure 3.3a, with 0% Ag, there are both small and big particles. After adding 1% Ag (Figure 3.3b), all the grains are small, which should be the best sample for antibacterial purposes, as they have a higher surface/volume ratio.

Increasing the amount of Ag only decreases the number of small particles, so they almost disappear in samples with 7% (Figure 3.3e) and 10% (Figure 3.3f). In this way, an increase in the amount of Ag by more than 5% varies the particle size, causing the surface/volume ratio to decrease considerably. The size of the Ag particles was very small (<30 nm), and for this reason, transmission electron microscopy (TEM) was used to evaluate the particle size and composition of the Ag nanoparticles.

TEM allows determination of the shape and particle size distribution of the silver nanoparticles and their location on the nanocomposite. Figure 3.4 shows selected STEM images and the element mapping of the ZnO/Ag nanocomposites.

The STEM image (Figure 3.4a) shows the presence of the Ag nanoparticles on the zinc oxide, thus forming the ZnO/Ag nanocomposite, which corresponds to sample Zn1 (1 at% of Ag). The Ag nanoparticles are mostly deposited in spherical form on the surface of the zinc oxide. The size of the silver nanoparticles ranged between 10 and 30 nanometers.

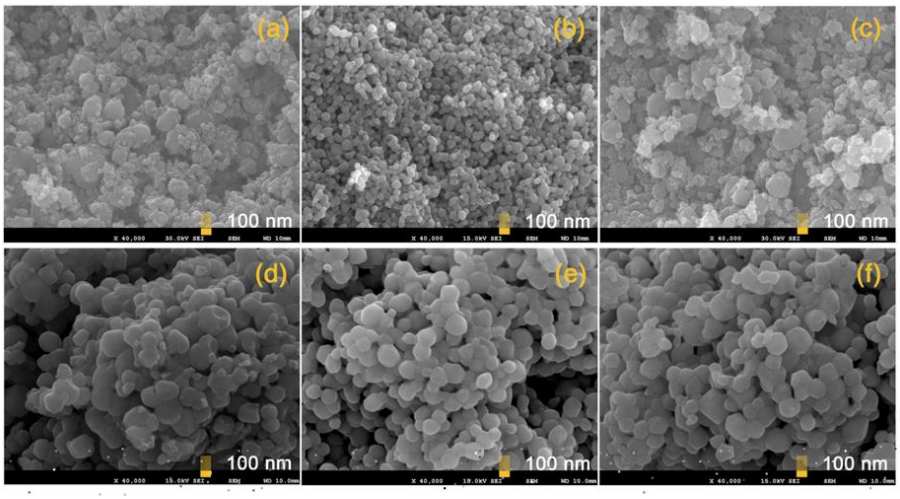

Figure 3.3 SEM images of ZnO/Ag nanocomposites: (a) Zn1, (b) Zn2, (c) Zn3, (d) Zn4, (e) Zn5, and (f) Zn6.

The distribution map of Zn (Figure 3.4b) was collected using Kα X-rays. Figure 3.4c shows the distribution map of O using Kα X-rays. The Ag map in Figure 3.4d also consists of Kα X-rays. The Ag maps can be observed even for some small particles. It is clear that in the case of the Ag nanoparticles shown here, the Ag signals are distributed in different regions as Zn signals or O signals, perfectly indicating the position of the Ag nanoparticles.

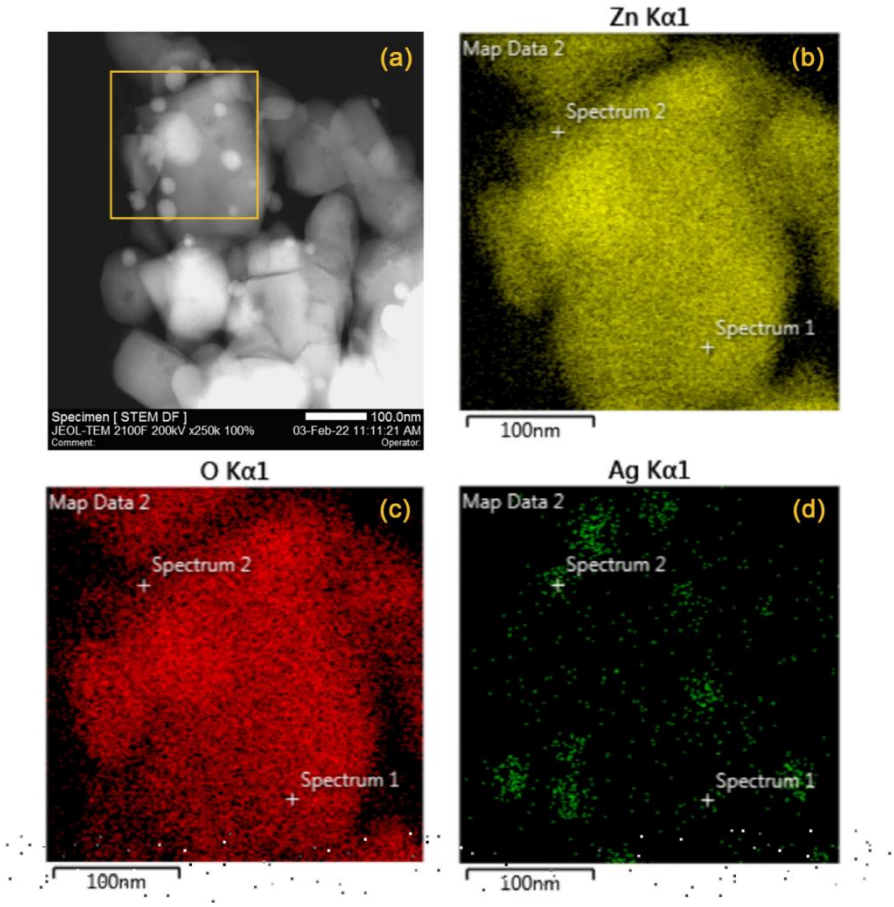

Figure 3.4 (a) STEM images of ZnO/Ag nanocomposites; (b) Elemental mapping of Zn collected using Kα X-rays, (c) Elemental mapping of O collected using Kα X-rays; (d) Elemental mapping of Ag collected using Kα X-rays.

3.2.6. UV-Vis Spectroscopy Studies

The absorption properties of ZnO/Ag nanocomposites were investigated with UV-Vis spectroscopy in the 200–650 nm range of wavelengths. Figure 3.5 shows the ab-sorption spectra for Ag nanoparticles on ZnO with different atomic contents of Ag. All the samples show strong absorption in the UV range.

Additionally, the broad exci-ton-related peak at 360–370 nm disappears, and this behavior is associated with UV absorption in zinc oxide [27]. The absorption spectrum of pure ZnO shows maximum absorption at 360 nm. Furthermore, with the Zn2 sample, the absorption edge shifted to a higher wavelength (365 nm) with respect to pure ZnO (Zn1). This shift is related to the incorporation of Ag NPs in the ZnO matrix [28].

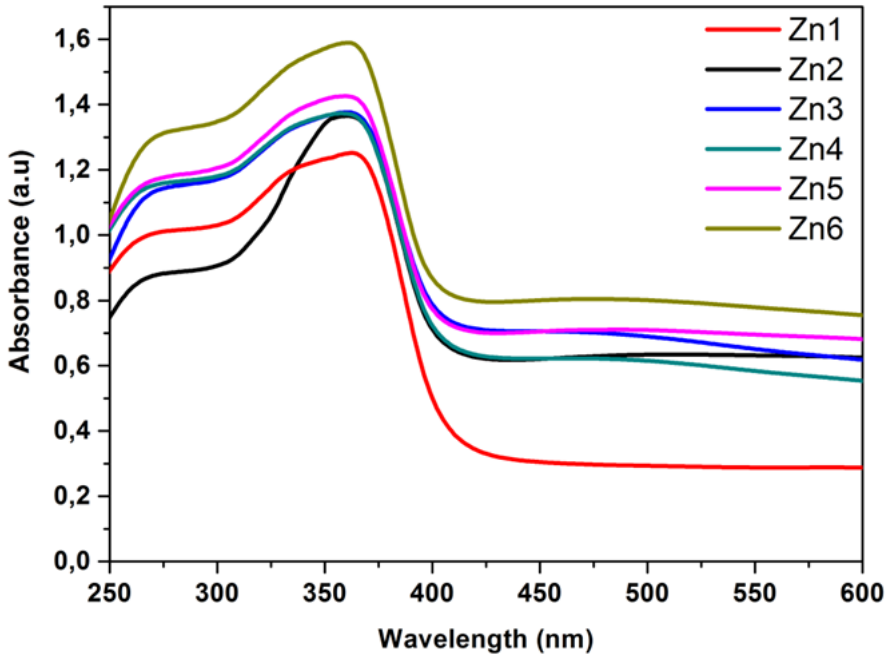

Figure 3.5 Absorption spectra of ZnO/Ag Nanocomposites: (a) Zn1, (b) Zn2, (c) Zn3, (d) Zn4, (e) Zn5, and (f) Zn6.

3.2.7. Raman Spectroscopy

Spectra measured under the 325 nm excitation wavelength are presented in Figure 3.6, which shows the typical spectra of ZnO compounds under the resonant conditions, with an intense LO peak (sum of two modes with A1 (LO) and E1 (LO) symmetry) and its second-order 2LO peak [29].

In the average spectra of each sample, additional small intensity peaks can be identified (see the vertical dashed lines in Figure 3.6). All of them are related to the fundamental or previously observed multiphonon modes of the ZnO compound [30]. No additional peaks/bands that can be associated with the presence of Ag NPs in the powders can be observed in the spectra that were measured.

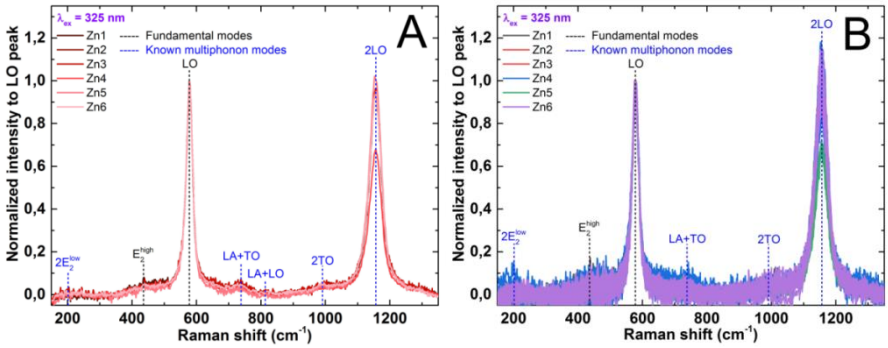

Figure 3.6 (A) Raman scattering spectra of nanocomposite samples (Zn1, Zn2, Zn3, Zn4, Zn5, and Zn6) were measured under 325 nm excitation wavelength in different points of the samples and (B) averaged per sample.

Furthermore, the homogeneity of the samples and possible correlation of the Ag atomic percentage with the intensity of additional peaks/bands were accomplished. For this different reference, the LO peak in the spectra was selected, measured under 325 nm excitation. This peak is separated from the additional bands and makes it possible to define the homogeneity or correlate the spectra evolution with the Ag content.

The homogeneity of the powders was assessed by calculating the relative integrated intensity of the 2LO peak in the spectra measured under 325 nm excitation. The ratio of intensities between the 2LO and LO peaks mainly changes due to the band gap variation in the ZnO compound, which changes the proximity to the resonant conditions.

As seen from the box plot in the left panel of Figure 3.7, the mean value of the relative integrated intensity of the 2LO peak is quite similar in all the samples, except for sample Zn4. Also, the homogeneity of the samples is different and is can be seen to be quite good for Zn2, with Zn3 being the worst. No correlation of the mean value or the inhomogeneity of the sample with the amount of Ag concentration was observed, assuming a gradual increase in the Ag NPs in the nanocomposites from sample Zn1 to sample Zn6.

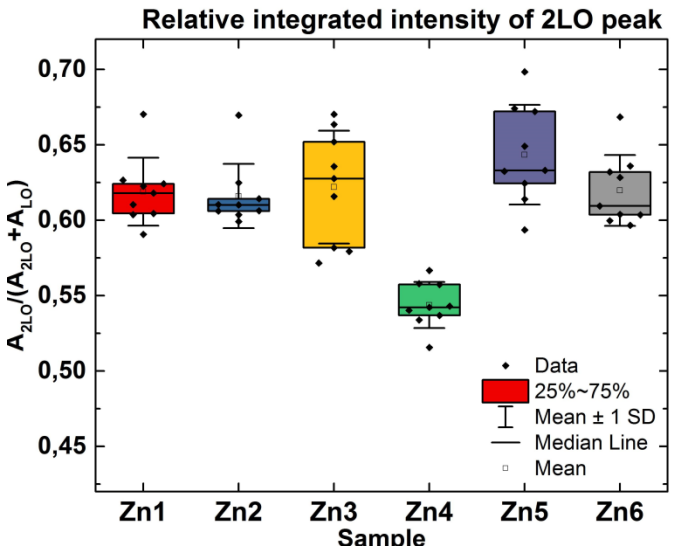

Figure 3.7. Relative integrated intensity of 2LO peak from the spectra measured under 325 nm exci-tation wavelength.

3.2.8.Antimicrobial Activity of ZnO/Ag Nanocomposites

The effect of ZnO/Ag nanocomposites at different concentrations of Ag was ana-lyzed in vitro against *S. aureus* and *E. coli*. The results showed a reduction in the growth of both bacteria in the presence of ZnO and ZnO/Ag nanocomposites when compared to controls. The antimicrobial effect of ZnO nanoparticles has been previously demon-strated, with an increase in the action of some antibiotics being observed in the presence of NP [33,34].

In the same way, there is clear evidence that the use of Ag nanoparticles increases the antimicrobial effect of certain antibiotics or defense-inducing molecules such as chitosan, which makes it difficult to analyze the effect of the nanoparticles [13,23,35–37]. Other authors have tested in vitro the effects of Ag NPs against *E. coli* and *S. aureus*, noting that Ag NPs were effective against *E. coli* but not against *S. aureus*.

However, the mechanism of action of the Ag NPs is still unknown, since it depends on the type of nanoparticle, the size, the arrangement of the ions, and their concentration [14,34,38,39] as well as the morphology of the bacteria (type of cell wall, type of metabolism, virulence mechanism, etc.) [40].

Previous studies have suggested that the action of Ag NPs on bacteria may be due to their ability to penetrate the cell [41], the production of reactive oxygen species (ROS) [42], or the formation of free radicals, as well as the inactivation of proteins in the cell by silver ions [15].

The variability of these results led us to test the effect of ZnO combined with dif-ferent concentrations of silver on *E. coli* and *S. aureus*. The novelty of our study lies in the synthesis method of the Ag NPs, which is a novel synthesis method based on sol-gel methodology, and in the fact that Ag NPs synthized in this study were able to inhibit high concentrations of both bacteria, which rarely occurs in real-life systems. The results obtained are shown in Figure 3.8

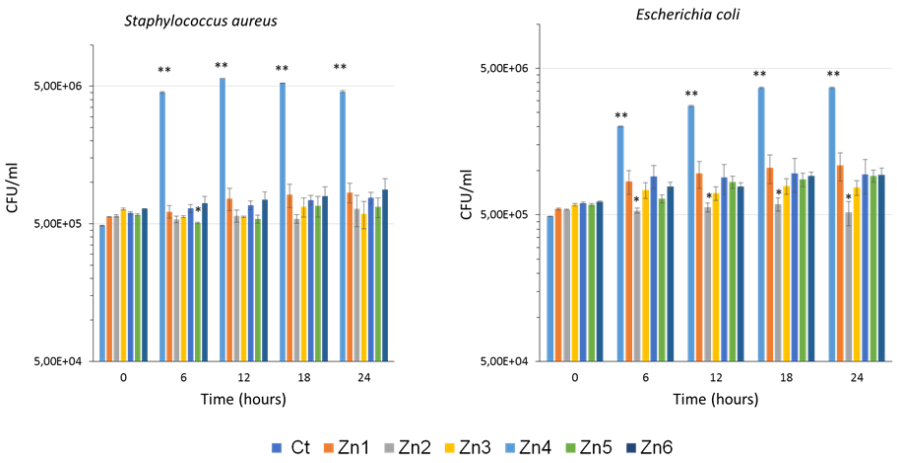

Figure 3.8 Results of the effect of the treatments on S. aureus and *E. coli* in the absence of treatment (Ct), with ZnO (Zn1) and with the ZnO/Ag nanocomposites (Zn2, Zn3, Zn4, Zn5, and Zn6). The bars on the graphs represent the standard error; the asterisks indicate significant differences.

Under our conditions, a reduction in bacterial growth was observed from 3h of inoculation in both bacteria and all treatments when compared to the control. In *S. aureus*, a similar effect in growth inhibition was observed in ZnO with or without Ag NPs; in *E. coli*, bacterial growth was greater in the absence of Ag NPs at all sampling times, although no significant differences were observed (Figure 3.9).

These results are in concordance with previous works observing that Gram-negative bacteria are more susceptible to silver nanoparticles. This may be due to the fact that the cellular wall of Gram-negative bacteria is narrower than that of Gram-positive strains, which may reduce the penetration of nanoparticles into the bacterial cells [43].

When analyzing the effect of the different concentrations of Ag against both bacteria, it can be seen that an increase in the concentration of Ag does not correlate with an increase in its effect against the bacteria. Furthermore, it seems that lower concentrations of Ag have greater efficacy against E. coli.

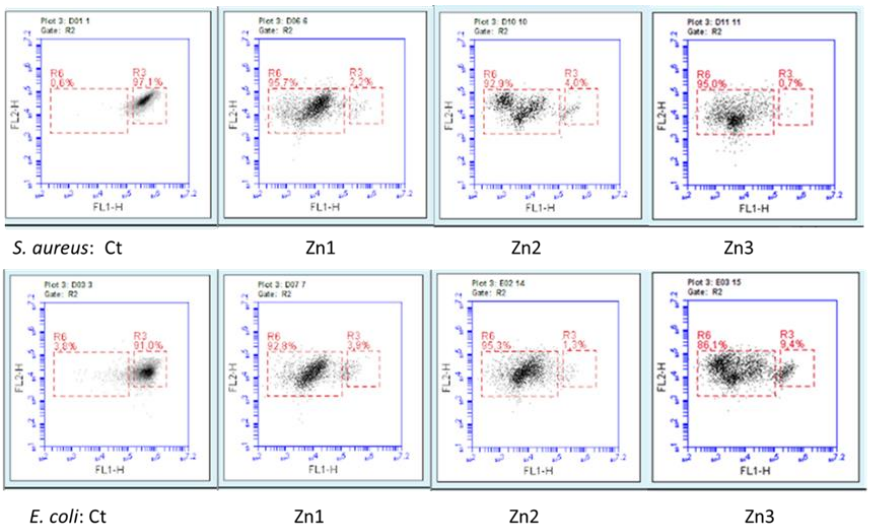

Figure 3.9. Cytometry charts showing the percentage of live and dead cells.

In order to check whether the effect of the Zn/Ag nanocomposites was bacteriostatic or bactericidal, the samples were stained with the LIVE/DEAD BacLight kit and further analyzed through flow cytometry.

All treatments showed a bactericidal effect when compared to controls, as seen in Figure 3.9. The treatments reduced the percentage of living cells by more than 90% in most cases. Table 2.1 shows the results of the percentages of live bacteria concerning the total number of cells counted, which were obtained using the flow cytometer after being stained with the live/dead kit.

Table 2.1 Percentage of live bacteria determined by using the flow-cytometer after being stained with the live/deadkit.

	Name of sample	**Ctr**	**Zn1**	**Zn2**	**Zn3**	**Zn4**	**Zn5**	**Zn6**
Percentage of live bacteria (%)	*S.aureus*	96.5	15	9	9	9	8	9
	E.Coli	91.25	12	6	6.5	9.5	5.5	4.5

The fact that increasing the silver concentration does not correlate with an increase in its antibacterial effect could be due to the arrangement of Ag in the NPs when added at higher concentrations. At higher concentrations, Ag tends to agglomerate, thereby decreasing the area of its surface in contact with the bacteria. Moreover, at higher concentrations of Ag, the size of the NPs is larger, as shown in Figure 3.2. Related to this, Ref. [44] reported that Ag NPs of smaller size could cause more toxicity to the bacteria and show better bactericidal effects compared to the larger particles as they have larger surface area.

In addition to being able to penetrate into bacterial cells, it is thought that another mechanism by which Ag NPs are killing bacteria is by releasing silver ions [45]. The efficiency of this process depends on different factors, such as intrinsic Ag NPs characteristics and surrounding media. For example, smaller silver nanoparticles are more prone to Ag release, due to their larger surface area. These findings could also support the fact that in our results, the antibacterial effect is not correlated with the concentration of Ag since Zn2 NPs containing 1% Ag are the smallest and are the most effective against the tested bacteria.

3.3. Conclusions

In summary, a soft chemical route was performed to prepare ZnO/Ag nanocomposites. The XRD patterns indicate the formation of separate phases, namely, a hexagonal wurtzite structure for ZnO and a cubic structure for Ag NPs

The formation of these separate phases can be seen when the atomic percentage of silver exceeds 3%. SEM shows that the presence of these Ag nanoparticles causes the growth of ZnO to vary, which can then affect its bactericidal power. STEM allows the morphology and sizes of the Ag NPs to be nano-spheres (~20 nm) on the wurtzite ZnO surface.

The absorption bands from the UV-Vis analysis of the samples increase due to the contribution from the surface plasmon resonance absorption of silver nanoparticles, showing significantly higher visible light absorption compared to the ZnO matrix. Raman spectroscopy showed that spectra measured in non-resonant conditions displayed a clear difference between the ZnO powder (Zn1) and nanocomposites with different Ag concentrations (Zn2–Zn6). Here, several non-fundamental peaks/bands are activated after adding Ag. In this way, it is clear that the silver is segregated in the form of NP and does not occupy positions within the zinc oxide structure. Some of them can be assigned to the previously observed multiphonon modes.

When analyzing the effect of the different concentrations of Ag against both bacteria, we can observe that an increase in the concentration of Ag does not correlate with an increase in its effect against the bacteria. Consequently, when the percentage of dopant increases, the Ag NPs tend to agglomerate, thereby decreasing both their surface area and the area of their surface in contact with the bacteria. Hence, using only 1 at% of Ag reduces the percentage of living cells by more than 90% in most cases, thus increasing their effectiveness in the destruction of bacteria by 5% compared to that of zinc oxide without Ag NPs.

3.4. References

[1] Lara, H.H.; Garza-Treviño, E.N.; Ixtepan-Turrent, L.; Singh, D.K. Silver nanoparticles are broad-spectrum bactericidal and virucidal compounds. J. Nanobiotechnol. 2011, 9, 2–9. https://doi.org/10.1186/1477-3155-9-30.

[2] Mittapally, S.; Taranum, R.; Parveen, S. Metal ions as antibacterial agents. J. Drug Deliv. Ther. 2018, 8, 411–419. https://doi.org/10.22270/jddt.v8i6-s.2063.

[3] Kim, J.S.; Kuk, E.; Yu, K.N.; Kim, J.-H.; Park, S.J.; Lee, H.J.; Kim, S.H.; Park, Y.K.; Park, Y.H.; Hwang, C.-Y.; et al. Antimicrobial effects of silver nanoparticles. Nanomed. Nanotechnol. Boil. Med. 2007, 3, 95–101. https://doi.org/10.1016/j.nano.2006.12.001.

[4] Baldino, L.; Aragón, J.; Mendoza, G.; Irusta, S.; Cardea, S.; Reverchon, E. Production, characterization and testing of antibacterial PVA membranes loaded with HA-Ag_3PO4 nanoparticles, produced by SC-CO_2 phase inversion. J. Chem. Technol. Biotechnol. 2018, 94, 98–108. https://doi.org/10.1002/jctb.5749.

[5] Huang, S.-M.; Liu, S.-M.; Ko, C.-L.; Chen, W.-C. Advances of Hydroxyapatite Hybrid Organic Composite Used as Drug or Protein Carriers for Biomedical Applications: A Review. Polymers 2022, 14, 976. https://doi.org/10.3390/polym14050976.

[6] Matai, I.; Sachdev, A.; Dubey, P.; Kumar, S.U.; Bhushan, B.; Gopinath, P. Antibacterial activity and mechanism of Ag–ZnO nanocomposite on *S. aureus* and GFP-expressing antibiotic resistant E. coli. Colloids Surf. B Biointerfaces 2014, 115, 359–367. https://doi.org/10.1016/j.colsurfb.2013.12.005.

[7] Hossain, M.K.; Khan, M.I.; El-Denglawey, A. A review on biomedical applications, prospects, and challenges of rare earth oxides. Appl. Mater. Today 2021, 24, 101104. https://doi.org/10.1016/j.apmt.2021.101104.

[8] Okeke, I.S.; Agwu, K.K.; Ubachukwu, A.A.; Ezema, F.I. Influence of transition metal doping on physiochemical and antibacterial properties of ZnO Nanoparticles: A review. Appl. Surf. Sci. Adv. 2022, 8, 100227. https://doi.org/10.1016/j.apsadv.2022.100227.

[9] Sirelkhatim, A.; Mahmud, S.; Seeni, A.; Kaus, N.H.M.; Ann, L.C.; Bakhori, S.K.M.; Hasan, H.; Mohamad, D. Review on Zinc Oxide Nanoparticles: Antibacterial Activity and Toxicity Mechanism. Nano-Micro Lett. 2015, 7, 219–242. https://doi.org/10.1007/s40820-015-0040-x.

[10] Saoud, K.; Alsoubaihi, R.; Bensalah, N.; Bora, T.; Bertino, M.; Dutta, J. Synthesis of supported silver nano-spheres on zinc oxide nanorods for visible light photocatalytic applications. Mater. Res. Bull. 2015, 63, 134–140. https://doi.org/10.1016/j.materresbull.2014.12.001.

[11] Djurišić, A.B.; Leung, Y.H. Optical Properties of ZnO Nanostructures. Small 2006, 2, 944–961. https://doi.org/10.1002/smll.200600134.

[12] Azfar, A.K.; Kasim, M.F.; Lokman, I.M.; Rafaie, H.A.; Mastuli, M.S. Comparative study on photocatalytic activity of transition metals (Ag and Ni)-doped ZnO nanomaterials synthesized via sol–gel method. R. Soc. Open Sci. 2020, 7, 191590. https://doi.org/10.1098/rsos.191590.

[13] Wolny-Koładka, K.; Lenart-Boroń, A. Antimicrobial resistance and the presence of extended-spectrum beta-lactamase genes in Escherichia coli isolated from the environment of horse riding centers. Environ. Sci. Pollut. Res. 2018, 25, 21789–21800. https://doi.org/10.1007/s11356-018-2274-x.

[14] Meier, M.J.; Dodge, A.E.; Samarajeewa, A.D.; Beaudette, L.A. Soil exposed to silver nanoparticles reveals significant changes in community structure and altered microbial transcriptional profiles. Environ. Pollut. 2020, 258, 113816. https://doi.org/10.1016/j.envpol.2019.113816.

[15] Rai, M.; Kon, K.; Ingle, A.; Duran, N.; Galdiero, S.; Galdiero, M. Broad-spectrum bioactivities of silver nanoparticles: The emerging trends and future prospects. Appl. Microbiol. Biotechnol. 2014, 98, 1951–1961. https://doi.org/10.1007/s00253-013-5473-x.

[16] Jide Zhang, "Silver-coated zinc oxide nanoantibacterial synthesis and antibacterial activity characterization," Proceedings of 2011 International Conference on Electronics and Optoelectronics, Dalian, China, 2011, pp. V3-94-V3-98, https://doi.org/10.1109/ICEOE.2011.6013309.

[17] Prashant V. Kamat, Rebecca Huehn, and Roxana Nicolaescu,The Journal of Physical Chemistry B, 2002, 106 (4), 788-794, https://doi.org/10.1021/jp013602t.

[18] Hermann, J., Tahiri, H., Ait-Ichou, Y., Lassaletta, G., Gonzalez-Elipe, A. and Fernandez, A. (1997) Characterization and Photocatalytic Activity in Aqueous Medium of TiO_2 and Ag-TiO_2 Coatings on Quartz. Applied Catalysis B: Environmental, 13, 219-228. http://.doi.org/10.1016/S0926-3373(96)00107-5.

[19] Karunakaran, C.; Rajeswari, V.; Gomathisankar, P. Enhanced photocatalytic and antibacterial activities of sol–gel synthesized ZnO and Ag-ZnO. Mater. Sci. Semicond. Process. 2011, 14, 133–138. https://doi.org/10.1016/j.mssp.2011.01.017.

[20] Merga, G.; Cass, L.C.; Chipman, D.M.; Meisel, D. Probing Silver Nanoparticles During Catalytic H_2 Evolution. J. Am. Chem. Soc. 2008, 130, 7067–7076. https://doi.org/10.1021/ja800306a.

[21] Stathatos, E.; Petrova, T.; Lianos, P. Study of the Efficiency of Visible-Light Photocatalytic Degradation of Basic Blue Adsorbed on Pure and Doped Mesoporous Titania Films. Langmuir 2001, 17, 5025–5030. https://doi.org/10.1021/la0103620.

[22] Shahverdi, A.R.; Fakhimi, A.; Shahverdi, H.R.; Minaian, S. Synthesis and effect of silver nanoparticles on the antibacterial activity of different antibiotics against Staphylococcus aureus and Escherichia coli. Nanomed. Nanotechnol. Biol. Med. 2007, 3, 168–171. https://doi.org/10.1016/j.nano.2007.02.001.

[23] Gouyau, J.; Duval, R.; Boudier, A.; Lamouroux, E. Investigation of Nanoparticle Metallic Core Antibacterial Activity: Gold and Silver Nanoparticles against Escherichia coli and Staphylococcus aureus. Int. J. Mol. Sci. 2021, 22, 1905. https://doi.org/10.3390/ijms22041905.

[24] Aymonier, C.; Schlotterbeck, U.; Antonietti, L.; Zacharias, P.; Thomann, R.; Tiller, J.C.; Mecking, S. Hybrids of silver nanoparticles with amphiphilic hyperbranched macromolecules exhibiting antimicrobial properties. Chem. Commun. 2002, 24, 3018–3019. https://doi.org/10.1039/b208575e.

[25] Loo, Y.Y.; Rukayadi, Y.; Nor-Khaizura, M.-A.; Kuan, C.H.; Chieng, B.W.; Nishibuchi, M.; Radu, S. In Vitro Antimicrobial Activity of Green Synthesized Silver Nanoparticles Against Selected Gram-negative Foodborne Pathogens. Front. Microbiol. 2018, 9, 1555. https://doi.org/10.3389/fmicb.2018.01555.

[26] Goh, E.; Xu, X.; McCormick, P. Effect of particle size on the UV absorbance of zinc oxide nanoparticles. Scr. Mater. 2014, 78–79, 49–52. https://doi.org/10.1016/j.scriptamat.2014.01.033.

[27] Singh, R.; Barman, P.B.; Sharma, D. Synthesis, structural and optical properties of Ag doped ZnO nanoparticles with enhanced photocatalytic properties by photo degradation of organic dyes. J. Mater. Sci. Mater. Electron. 2017, 28, 5705–5717. https://doi.org/10.1007/s10854-016-6242-2.

[28] Phan, T.-L.; Vincent, R.; Cherns, D.; Dan, N.H.; Yu, S.-C. Enhancement of multiple-phonon resonant Raman scattering in Co-doped ZnO nanorods. Appl. Phys. Lett. 2008, 93, 082110. https://doi.org/10.1063/1.2968307.

[29] Cuscó, R.; Alarcón-Lladó, E.; Ibáñez, J.; Artús, L.; Jiménez, J.; Wang, B.; Callahan, M.J. Temperature dependence of Raman scattering in ZnO. Phys. Rev. B 2007, 75, 165202. https://doi.org/10.1103/physrevb.75.165202.

[30] Rousset, J.; Saucedo, E.; Lincot, D. Extrinsic Doping of Electrodeposited Zinc Oxide Films by Chlorine for Transparent Conductive Oxide Applications. Chem. Mater. 2009, 21, 534–540. https://doi.org/10.1021/cm802765c.

[31] Guc, M.; Tsin, F.; Rousset, J.; Romanyuk, Y.E.; Izquierdo-Roca, V.; Pérez-Rodríguez, A. Nondestructive Raman Scattering Assessment of Solution-Processed ZnO-Doped Layers for Photovoltaic Applications. J. Phys. Chem. C 2017, 121, 3212–3218. https://doi.org/10.1021/acs.jpcc.6b11525.

[32] Banoee, M.; Seif, S.; Nazari, Z.E.; Jafari-Fesharaki, P.; Shahverdi, H.R.; Moballegh, A.; Moghaddam, K.M.; Shahverdi, A.R. ZnO nanoparticles enhanced antibacterial activity of ciprofloxacin against Staphylococcus aureus and Escherichia coli. J. Biomed. Mater. Res. Part B Appl. Biomater. 2010, 93, 557–561. https://doi.org/10.1002/jbm.b.31615.

[33] Chakraborti, S.; Mandal, A.; Sarwar, S.; Singh, P.; Chakraborty, R.; Chakrabarti, P. Bactericidal effect of polyethyleneimine capped ZnO nanoparticles on multiple antibiotic resistant bacteria harboring genes of high-pathogenicity island. Colloids Surf. B Biointerfaces 2014, 121, 44–53. https://doi.org/10.1016/j.colsurfb.2014.03.044.

[34] Fayaz, A.M.; Balaji, K.; Girilal, M.; Yadav, R.; Kalaichelvan, P.T.; Venketesan, R. Biogenic synthesis of silver nanoparticles and their synergistic effect with antibiotics: A study against gram-positive and gram-negative bacteria. Nanomed. Nanotechnol. Biol. Med. 2010, 6, 103–109. https://doi.org/10.1016/j.nano.2009.04.006.

[35] Chopade, B.A.; Singh, R.; Wagh, P.; Wadhwani, S.; Gaidhani, S.; Kumbhar, A.; Bellare, J. Synthesis, optimization, and characterization of silver nanoparticles from Acinetobacter calcoaceticus and their enhanced antibacterial activity when combined with antibiotics. Int. J. Nanomed. 2013, 8, 4277–4290. https://doi.org/10.2147/IJN.S48913.

[36] Ruddaraju, L.K.; Pammi, S.; Guntuku, G.S.; Padavala, V.S.; Kolapalli, V.R.M. A review on anti-bacterials to combat resistance: From ancient era of plants and metals to present and future perspectives of green nano technological combinations. Asian J. Pharm. Sci. 2020, 15, 42–59. https://doi.org/10.1016/j.ajps.2019.03.002.

[37] Pal, S.; Tak, Y.K.; Song, J.M. Does the Antibacterial Activity of Silver Nanoparticles Depend on the Shape of the Nanoparticle? A Study of the Gram-Negative Bacterium Escherichia coli. Appl. Environ. Microbiol. 2007, 73, 1712–1720. https://doi.org/10.1128/aem.02218-06.

[38] Martínez-Castañón, G.A.; Niño-Martínez, N.; Martínez-Gutierrez, F.; Martínez-Mendoza, J.R.; Ruiz, F. Synthesis and antibacterial activity of silver nanoparticles with different sizes. J. Nanoparticle Res. 2008, 10, 1343–1348. https://doi.org/10.1007/s11051-008-9428-6.

[39] Zhang, M.; Zhang, K.; De Gusseme, B.; Verstraete, W.; Field, R. The antibacterial and anti-biofouling performance of biogenic silver nanoparticles by Lactobacillus fermentum. Biofouling 2014, 30, 347–357. https://doi.org/10.1080/08927014.2013.873419.

[40] Sondi, I.; Salopek-Sondi, B. Silver nanoparticles as antimicrobial agent: A case study on *E. coli* as a model for Gram-negative bacteria. J. Colloid Interface Sci. 2004, 275, 177–182. https://doi.org/10.1016/j.jcis.2004.02.012.

[41] Dutta, R.; Nenavathu, B.P.; Gangishetty, M.K.; Reddy, A. Studies on antibacterial activity of ZnO nanoparticles by ROS in-duced lipid peroxidation. Colloids Surf. B Biointerfaces 2012, 94, 143–150. https://doi.org/10.1016/j.colsurfb.2012.01.046.

[42] Meikle, T.G.; Dyett, B.P.; Strachan, J.B.; White, J.; Drummond, C.J.; Conn, C.E. Preparation, Characterization, and Antimicrobial Activity of Cubosome Encapsulated Metal Nanocrystals. ACS Appl. Mater. Interfaces 2020, 12, 6944–6954. https://doi.org/10.1021/acsami.9b21783

[43] Zhang, X.-F.; Liu, Z.-G.; Shen, W.; Gurunathan, S. Silver Nanoparticles: Synthesis, Characterization, Properties, Applications, and Therapeutic Approaches. Int. J. Mol. Sci. 2016, 17, 1534. https://doi.org/10.3390/ijms17091534.

[44] Yin IX, Zhang J, Zhao IS, Mei ML, Li Q, Chu CH. The Antibacterial Mechanism of Silver Nanoparticles and Its Application in Dentistry. Int J Nanomedicine. 2020 Apr 17;15:2555-2562. https://doi.org/10.2147/IJN.S246764.

CHAPTER 4

Functional properties of transparent ZnO thin films synthetized by using spray pyrolysis for environmental and biomedical applications

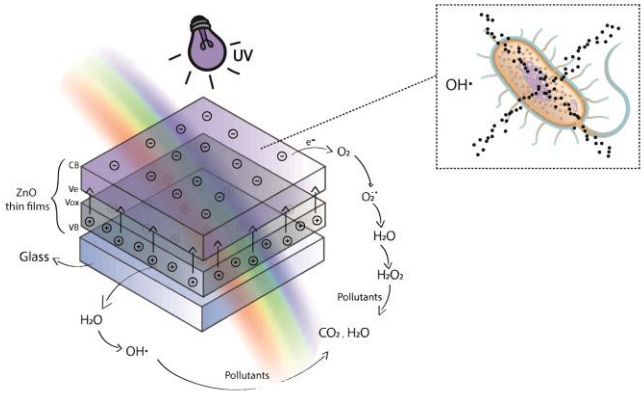

J.G. Cuadra, A.C. Estrada, C. Oliveira, L.A. Abderrahim, S. Porcar, D. Fraga, T. Trindade, M.P. Seabra, J. Labrincha, J.B. Carda, Functional properties of transparent ZnO thin films synthetized by using spray pyrolysis for environmental and biomedical applications, Ceram. Int. (2023). https://doi.org/10.1016/j.ceramint.2023.07.246.

"We are creating materials with customized properties that we could only imagine in science fiction before. Materials chemistry is taking science and engineering to new heights."

Angela Belcher

Abstract: Spray pyrolysis is a promising method for producing thin, transparent films on glass substrates. ZnO thin films synthesized by this method exhibit high crystallinity, adhesion and chemical resistance. They also possess the ability to degrade water pollutants and exhibit antibacterial properties under UV light. The crystalline structure of these films has been studied using grazing X-ray diffraction (GIXRD), atomic force microscopy (AFM) and scanning electron microscopy (SEM), while transmission electron microscopy (TEM) has been used to investigate their composition and purity. Other techniques such as X-ray photoelectron spectroscopy (XPS), Raman spectroscopy and ultraviolet-visible spectroscopy were also employed. ICP-OES was used to evaluate photocatalyst leaching. These transparent thin films have exceptional optical properties, with a transmittance of 95%. The photocatalytic degradation of 4-Nitrophenol (4-NP) by ZnO thin films showed a degradation rate of 94% in 270 minutes with a kinetic constant value of 3.1×10^{-3} mM/min. The films are also highly durable and reusable, exhibiting superior performance compared to other ZnO photocatalysts. The bactericidal activity of these transparent films was also evaluated, with a value of 60.6% being obtained using Escherichia coli after irradiating the films with UV light for 3 hour.

4.1. Introduction

In recent years, materials transparency has become a very important aspect in several fields such as optics and photonics [1,2], architecture and construction [2,3], electronics [4,5], medicine [6,7] or aerospace and defence [8,9]. Transparent materials thus play a crucial role in many areas of modern technology and industry, and their continued development and improvement are essential to advance in these fields [10].

Zinc oxide (ZnO) is among the most researched materials that become transparent, and consequently it is also one of the most widely used oxides in photocatalysis [11,12], photovoltaic cells [13,14], piezoelectrics [15,16], sensors [17,18], antibacterial agents [19,20] or fungicides [21,22]. ZnO belongs to the n-type semiconductor with an exciton binding energy of 60 meV and a direct band gap of 3.37 eV.This bandgap value indicates its high UV absorption and its transparency towards the visible range [23,24].

Reactive oxygen species (ROS) such as superoxide anion ($O_2^{-\bullet}$), hydroxyl radical (OH•) and singlet oxygen ($^1O_2$) are able to degrade different types of organisms such as gram-positive and gram-negative bacteria [25,26] and cancer cells [27] by inducing oxidative stress [28,29], as well as promoting the degradation of water pollutants [30]. Some of the substances described as water pollutants by the European Chemical Agency (ECHA) [31] are pharmaceuticals [32], pesticides [33], personal care products (PCPs) [34] or industrial by-products [35].

Moreover, there is a wide variety of morphologies thanks to the different methods of ZnO synthesis, whether in the form of nanoparticles (NPs) [36], nanotubes (NTs) [37], nanowires (NWs) [38] or thin films [39]. The use of ZnO NPs as bactericidal agents is well known, with particle size, smaller particles generally having a higher surface area-to-mass ratio, which can enhance their reactivity and potentially lead to increased ROS [40].

However, ZnO NPs and NTs used as antibacterial agents or photocatalysts for pollutants in water have serious limitations, especially when used to functionalize a surface. First, NPs tend to aggregate, leading to a decrease in their antibacterial capability [41].

Although aggregation is discussed in the context of NPs, this phenomenon also occurs in a large number of nanostructured materials, due to the strong interaction that NPs undergo in relation to their size, shape, surface charge or pH of the medium in which they are dispersed [42,43].

Another major challenge in the use of ZnO NPs is their relatively low stability in aqueous solutions, which limits their application as photocatalysts for surfaces that may come into contact with water [44–46].

For the generation of surfaces with antimicrobial properties, it is mandatory to ensure that ZnO NPs are firmly attached to the surface and that they are not released over time.

A multitude of methods are available to obtain transparent thin films, such as atomic layer deposition (ALD) [47], chemical vapour deposition (CVD) [48], electroplating [49] or sol-gel spin coating [50]. In all these techniques the adaptation to industrial applications is severely limited because they require high levels of technical sophistication or the creation of a high vacuum for the production of thin films [51].

However, the spray pyrolysis method has no such drawbacks because it is able to produce transparent thin films by simply spraying a precursor solution of the material onto the heated substrate. Moreover, it can be used on a multitude of substrates, including glass [52], metal or polymer [53], which is advantageous for industrial applications.

In this work, the deposition of ZnO on glass to form a thin transparent film has been achieved using the spray pyrolysis method. The transparent ZnO thin films exhibit high crystallinity and adhesion to glass substrates, as well as high resistance in neutral and basic aqueous media.

The study of this material as a photocatalyst was also carried out using a UV lamp, revealing that it has a high capacity for the photodegradation of a pollutant such as 4-NP. In addition, it was demonstrated that these thin films, when exposed to this type of light, can function as antibacterial surfaces.

4.2. Results and discussion

4.2.1. Chemicals

Zinc acetate ($Zn(CH_3COO)_2 \cdot 2H_2O$ ≥99.5% PanReac AppliChem, ethanol (EtOH, Scharlau), ammonia (NH_3, 30% w/w, PanReactAppliChem), 4-nitrophenol (4-NP, ≥98%, Sigma-Aldrich), sodium hydroxide (NaOH, pearls 1–2 mm, ≥98%, Labkem), hydrochloric acid (HCl, 37%, PanReactAppliChem) and deionized water, with pH 7.1 ± 0.2 and a resistivity of 17.9 MΩ-cm (Ultramatic Plus, Wasserlab, Spain) were used. Tert-butyl alcohol (t-BuOH), formic acid (HCOOH) and 1,4-Benzoquinone ($C_6H_4O_2$) (99%, purity) were purchased from Sigma-Aldrich.

4.2.2. Instrumentation

The transparent ZnO thin films were examined to determine their crystalline structure using grazing incidence X-ray diffraction (GIXRD). To conduct the analysis, a Cu K radiation source-equipped Burker-ASX X-ray diffractometer, specifically the D4 Endeavour model, was employed. The scanning process involved stepping from 10º to 90º 2θ, with a step size of 0.05º 2θ and a counting duration of 3 seconds per step.

The incident angle of the measurements, approximately 1º, was determined experimentally. For the investigation of surface characteristics, morphology, and thickness of the coatings, scanning electron microscopy (SEM) was performed using a JEOL 7001F instrument. SEM-EDS mappings were obtained using an acceleration voltage of 10 kV and a beam current of 0.6 nA.

To ensure accurate spectral recordings, drift correction was applied, with a step size of 0.3 μm and a minimal dwell time of 0.3 msec. The EDS analyses were conducted using Aztec 4.3 software developed by Oxford Instruments in the United Kingdom. To measure the thickness of the layers, micrographs of cross-sections were utilized. The crystallite sizes were determined by applying the Debye-Scherrer equation (equation 4.1) to the XRD data [52].

$$D = \frac{k\lambda}{\beta \cos \theta} \tag{4.1}$$

The Debye-Scherrer equation (equation 4.1) utilizes various parameters to determine the crystallite sizes. In the equation, the Scherrer constant (k) is typically 0.9 for spherical particles, the X-ray wavelength (λ) is 1.5405 Å, the peak width at half-maximum (β) represents the width of the peak at half of its maximum intensity, and θ corresponds to the Bragg diffraction angle [55].

To examine the surfaces of the transparent thin films, an Atomic Force Microscope (AFM) operating in contact mode was used. Specifically, a JSPM-5200 JEOL Scanning Probe Microscope was used for this purpose.

For Transmission Electron Microscopy (TEM), a JEOL JEM-1010 EM-24830 FLASH digital camera equipped with a CMOS sensor was utilized. This camera offers a resolution of 2k × 2k and facilitated the TEM analysis.

The microscope also featured an Oxford STEM DF/BF image acquisition system with a drift silicon sensor,an 80 mm^2 window and 127 eV resolution for the Mn K line. Before TEM analysis, a drop (8 μL) of a suspension of the removed thin film diluted in ethanol was deposited on a copper grid with an amorphous carbon film and allowed to dry.

The thin film's composition and purity were examined using X-ray photoelectron spectroscopy (XPS) on a Sage 150 photoelectron spectrometer, which is part of a multi-technique surface analysis system. The electron-energy detection was performed using a Mac 2 Cameca Riber double stage cylindrical mirror detector.

The X-ray source utilized was a dual anode Cameca SCX700. In all cases, a non-monochromatic Al K X-ray source (energy = 1486.6 eV) was employed for excitation. Raman scattering measurements were carried out using a Hobiba Jobin-Yvon FHR-640 monochromator coupled with a CCD detector in a backscattering configuration. Gas (325 nm) and solid-state (532 nm) lasers with respective power densities ~10 and ~50 W/cm^2 were used to excite the samples.

The spectral alignment was adjusted by setting the primary peak of a monocrystalline silicon sample to 520 cm^{-1}. Diffuse reflectance spectroscopy (DRS) was conducted on a UV-Vis spectrophotometer (JASCO U-560).

The spectra of the materials were obtained using a Bruker Optics Tensor 27 spectrometer connected to a horizontal attenuated total reflectance (ATR) cell, with 256 scans performed at a resolution of 4 cm^{-1}. To analyze the leaching of the photocatalyst, a Jobin Yvon Activa M ICP-OES instrument was utilized.

The optical bandgap value for the thin film was derived from the absorption coefficient (α) value, which was calculated using Lambert's Law in the following equation (4.2) [53]:

$$A = \frac{1}{t} \ln\left(\frac{1}{T}\right) \quad (4.2)$$

where T is the transmittance, and t is the film thickness.

The optical bandgap of thin films could be calculated by extrapolating $(\alpha h\nu)^2$ versus hν using equation (4.3).

$$\alpha h\upsilon = A\left(h\upsilon - E_g\right)^{\frac{1}{2}} \quad (4.3)$$

where A is a constant, hν is the photon energy, and Eg is the optical bandgap.

4.2.3. Preparation of transparent ZnO thin films

For the preparation of the transparent ZnO thin films, 0.5 mol of $Zn(CH_3COO)_2 \cdot 2H_2O$ were dissolved in EtOH (40 mL). This mixture of precursors was stirred for 1h to ensure the homogeneity of the solution.

Using a 100 mL capacity atomizer with a fine grade of spraying (CAT NUMBER: 34 48 51) connected to a compressed air pump at a pressure of 0.9 bar (Fig. S1), transparent thin coatings were manually deposited onto a soda-lime glass (2.5 × 2.5 cm) previously heated to 400ºC (Fig. 4.1).

Prior to heating, the glass was cleansed in a 30% (w/w) NH_3 solution followed by ultrasonication for 15 min. The deposited thin coatings were then heated to 500ºC on a hot plate under atmospheric pressure to remove any organic residue. Figure. S2 shows the appearance of the transparent ZnO thin films on the glass substrate.

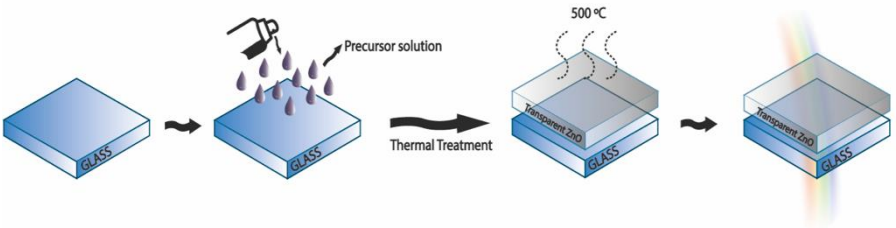

Figure 4.1 Schematic representation of the preparation of transparent ZnO thin films on glass substrates.

4.2.4. Experiments for the screening of photocatalytic activity.

The photocatalytic efficiency of the ZnO thin film was examined for its ability to degrade 4-Nitrophenol (4-NP) under UV light exposure at room temperature. In a typical procedure, the samples were immersed in a glass vessel containing 30 mL of an aqueous solution of 4-NP (6.95 mg/L). Prior to irradiation, the solution was left in darkness for 30 minutes to establish an adsorption/desorption equilibrium.

A UV light source (SUPRATECH HTC 150-211 UV, Osram) with a nominal power rating of 150 W, emitting 22 W in the UVA region (315-400 nm) and 6 W in the UVB region (280-315 nm), was employed. The light intensity measured was 0.105 W/cm^2. Refer to Figure. S3 for a depiction of the experimental setup for the photocatalysis. At regular intervals, samples of the reaction mixture were withdrawn, and a NaOH pellet was promptly added to each of them to induce the formation of 4-nitrophenolate ions, which exhibit maximum absorption at 410 nm (Figure. S4). The concentration of 4-NP was monitored using UV-Vis spectroscopy at 410 nm, employing equation (4.4):

$$\eta\ (\%) = \left(1 - \frac{C_t}{C_0}\right) \times 100 \qquad (4.4)$$

where C_0 represents the initial 4-NP concentration and Ct refers to the real-time concentrations of 4-NP, respectively. The kinetics of 4-NP were performed using the expression presented in equation (4.5):

$$k_{app} = -\frac{C - C_0}{t} \qquad (4.5)$$

where k_{app} (mM/min) represents the reaction rate constant in mM at time t (min).

To determine the stability of the as-prepared ZnO thin film, it was recovered and subjected to four additional photodegradation cycles under the same conditions.

To clarify the photocatalytic reaction mechanism, the degradation of 4-NP was carried out in the presence of 1 mM of tert-butyl alcohol (t-BuOH), formic acid (FA), and 1,4-Benzoquinone (1,4-BQ), which are known as scavenger species, for capturing hydroxyl radicals (OH•), holes (h^+) and superoxide radicals ($O_2^{-\bullet}$), respectively [54,55].

4.2.5. Determination of antibacterial activity

The antibacterial activity of ZnO thin films was evaluated using a modified version of the standard method test Jisz 2801_2000 as described previously [56]. Briefly, Escherichia coli ATCC 25922 cells were used to test for the antibacterial activity of ZnO thin films with or without irradiation of UV light for 3h. As a reference, glass samples were used. At least 2 sample pieces for each condition were used and 3 plates per sample were cultivated to determine the concentration of colony-forming units (CFU/mL) in each assayed condition.

The antibacterial rate (R) was calculated according to equation (4.6):

$$(\mathrm{R}) = (N_0 - \mathrm{N})/N_0 \times 100 \qquad (4.6)$$

where N_0 represents the average number of viable bacteria on a reference sample, and N is the average number of bacteria on tested samples.

4.2.6. Characterization of transparent ZnO thin films

The microstructure of ZnO thin films, such as crystalline orientation, crystalline structure, uniformity, and film density, was studied. The orientation and structure of ZnO crystals were analysed based on GIXRD patterns. Seven diffraction peaks were identified in the GIXRD pattern, indicating a polycrystalline structure, as shown in Figure. 4.2a.

The most intense diffraction peak (002) indicates that the crystallites are predominantly oriented perpendicular to the glass substrate on which they have been deposited. Using thin film deposition techniques, crystalline growth is predominant along the z-axis due to the reduced surface energy of the (002) plane [57].

Furthermore, the computed values for the lattice constants a and c were determined to be 3.24 Å and 5.21 Å.The ratio of c to a (c/a) was found to be 1.602, which closely approximates the c/a ratio observed in a hexagonal structure (c/a = 1.633). Hence, the values are in accordance with those indicated in the standard card (JCPDS 070-2551) for ZnO, wurtzite type.

The mean particle size (D) of the ZnO thin films, estimated to be 25.0 nm, was calculated using the Scherrer equation based on the diffraction peak at$2\theta = 34.4^{o}$ associated with the (002) reflection plane. AFM images reveal that the surface of these thin films is rough, with a root-mean-square (RMS) roughness of 29.9 nm and an average roughness (AR) of 24.4 nm.

The RMS value obtained is comparable to values obtained on SiO_2/Si substrates [60], and the average particulate size of ZnO in the layer corresponds to the value estimated by Sherrer's formula. Figure. 4.2c shows the top view, and Figure. 4.2d shows the cross-sectional view of the ZnO thin films.

The top view SEM image (Figure. 4.2c) confirms the formation of a dense layer, consisting of flawlessly sintered round grains.

In addition, the cross-sectional SEM image shows that ZnO has a dense columnar structure and that its adhesion to the glass substrate is strong and delamination-free (Figure. 4.2d). Figure. S5 shows the transmission electron microscopy of a selective area, confirming that ZnO crystals grew perpendicular to the glass.

The interplanar distance calculated from Figure. S5 is 0.26 nm, which is consistent with the interplanar distance of the (002) plane of ZnO (JCPDS 070-2551). EDS analysis shows that the transparent thin film is composed exclusively of ZnO.

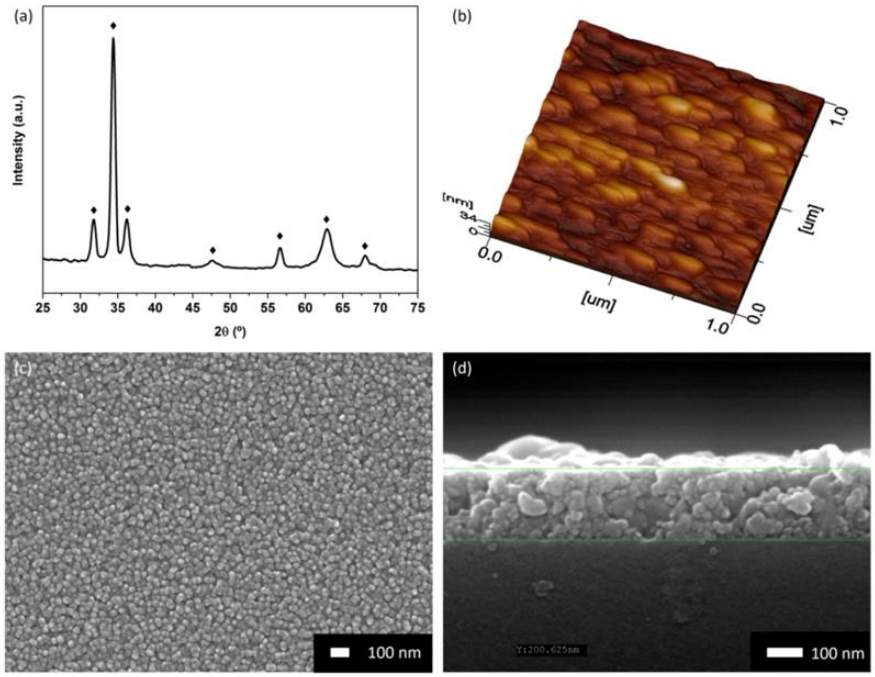

Figure 4.2 (A) GIXRD pattern, (b) AFM image, (c) top SEM image, and (d) cross-sectional SEM image of transparent ZnO thin films.

The Raman spectrum of a ZnO thin film measured under a 325 nm excitation wavelength, showing the vibrational modes, is presented in Figure. 4.3. Under resonant conditions, the intense LO peak (sum of two modes with A1(LO) and E1(LO) symmetry) and a second-order 2LO peak are observed in ZnO thin films [58].

These additional low-intensity peaks can be identified (see the vertical dashed lines in Figure. 4.3). They all are associated with the fundamental or previously identified multiphonon modes of crystalline ZnO [59]. No additional peaks/bands that could be associated with the presence of other metals or impurities were visible. XPS was used to confirm the presence of Zn, O and C.

The characteristic peaks of Zn 2p (1021 eV), O 1s (530 eV) and C 1s (285 eV) are shown in Figure. S6, quantifying the atomic content of the transparent thin film as 54.2, 42.6 and 3.3% of Zn, O and C, respectively.

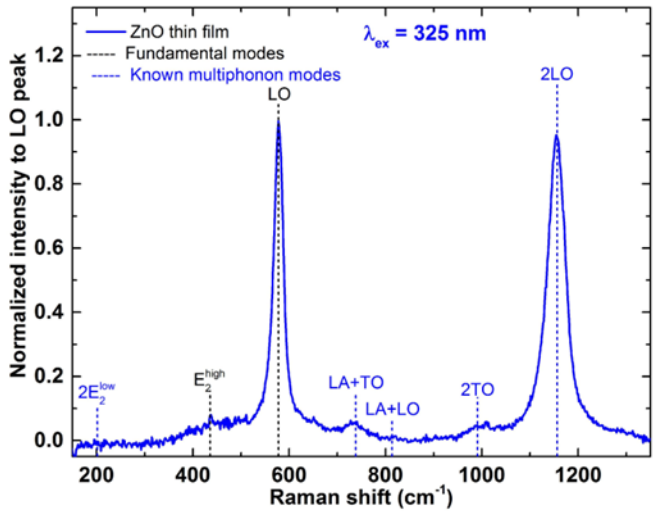

Figure 4.3 Raman spectrum of a typical ZnO thin film (laser line at 325 nm).

As shown in Figure. 4.4, the transparent ZnO thin films exhibit high absorbance below 350 nm and high transmittance, reaching approximately 95% above 350 nm, i.e. across all the visible range. Figure.S3 shows the high transparency of ZnO thin films deposited on glass.

The optical band gap value was estimated using the interpolation of the Tauc plot with with respect to the x-axis. As shown in Figure. 3b, the estimated value was 3.28 eV. The estimated values agree with the latest reported values for ZnO thin films [60,61].

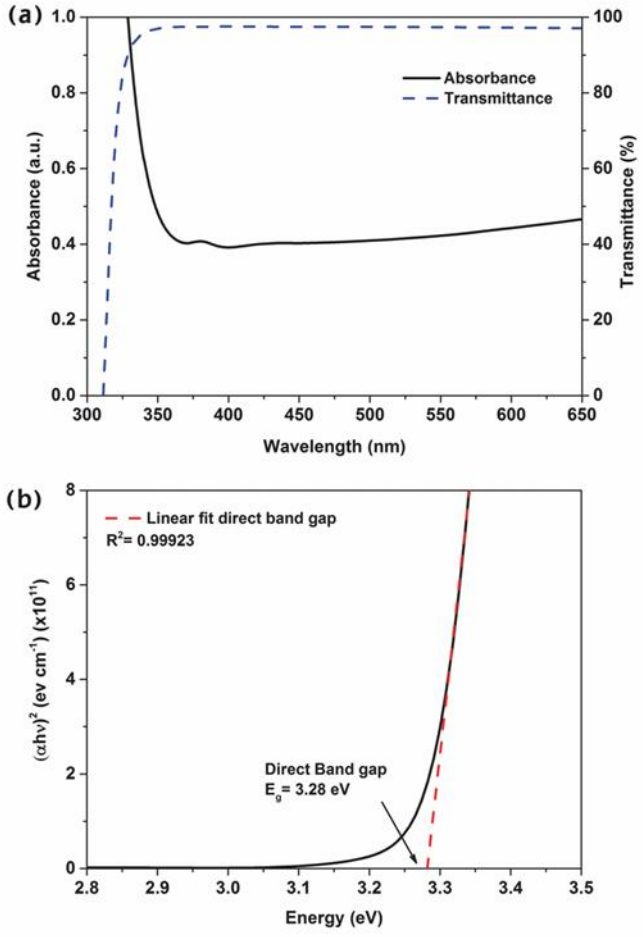

Figure 4.4 The optical characteristics of the ZnO thin film, (a) the absorbance and transmittance spectra analyzed using UV–vis spectroscopy, and (b) the determination of the energy band gap through the Tauc plot.

4.2.7. Photocatalytic degradation of 4-NP

Initially, the photodegradation of 4-NP in the absence of ZnO thin films was evaluated in two control tests: (i) under UV-light irradiation and (ii) under UV-light irradiation with an uncoated glass substrate.

The results demonstrated that only 10% of 4-NP had been degraded after 270 minutes in both experiments (i) and (ii) (Figure. S7). Furthermore, the capacity of the thin films to adsorb 4-NP molecules was also evaluated using ZnO thin films under dark conditions.

The investigation revealed that a minute quantity of 4-NP was captured by the ZnO thin films' surface (approximately 9%), and the highest level of adsorption was attained within a 30-minute interaction period, (refer to Figure. S8).

Thin films had a total weight of 0.112 mg/cm^2, which is a smaller amount of catalyst as compared to related work published in the literature [62,63].

The ZnO thin films showed high photocatalytic activity, leading to 94% 4-NP degradation after 270 minutes, as shown in Figure. 4.5(a).

Figure. 4.5(b) illustrates the difference in photodegradation efficiency by depicting the C/C_0 for the transparent ZnO thin films. The 4-NP concentration was obtained using the calibration curve presented in Figure. S9.

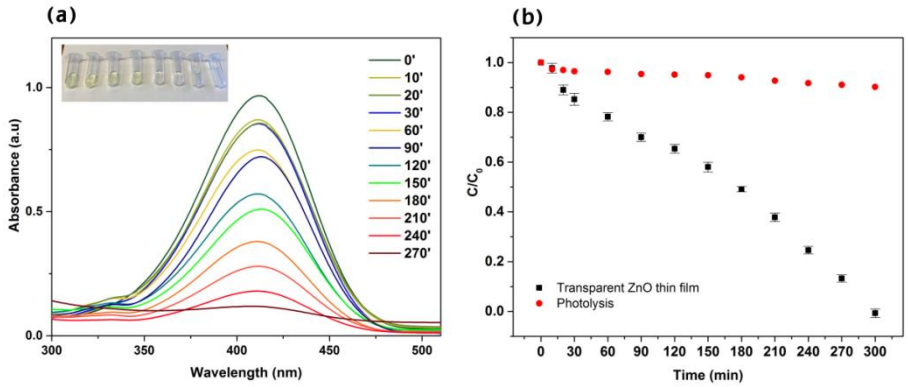

Figure 4.5 (A) UV–Vis absorption spectra of aqueous solutions of 4-NP (C_0 = 6.95 mg/L) under UV-light irradiation in the presence of transparent ZnO thin films, and (b) pseudo-zero-order decay fitted linear regression curve for 4-NP photodegradation in the presence of transparent ZnO thin films and photolysis.

The kinetic profile of 4-NP degradation using the ZnO thin film is shown in Figure. 4.5(b), which agrees with a pseudo-zero-order reaction with a kinetic rate constant of 3.1×10^{-3} mM/min. The obtained kinetic constant for the degradation of other benzoic compounds using ZnO as a photocatalyst (Table 4.1) is a significantly lower value.

On the other hand, the photocatalytic degradation rate of 4-NP decreased from 94% to 33% upon addition of hydroxyl scavenger (tert-butyl alcohol) to the reaction mixture, whereas addition of FA or 1,4-BQ only decreased the degradation rate to 62% and 55%, respectively (Figure.4. 6(a)).

The bar graph in Figure. 4.6(b) clearly illustrates the effect of the tested scavengers on the photocatalytic degradation of 4-NP over the ZnO thin film.

Figure. 4.6(a) and 4.6(b) show that h^+ and $O_2^{-\bullet}$ exert a negligible contribution to 4-NP removal, thereby confirming the crucial role of OH• in the degradation process.

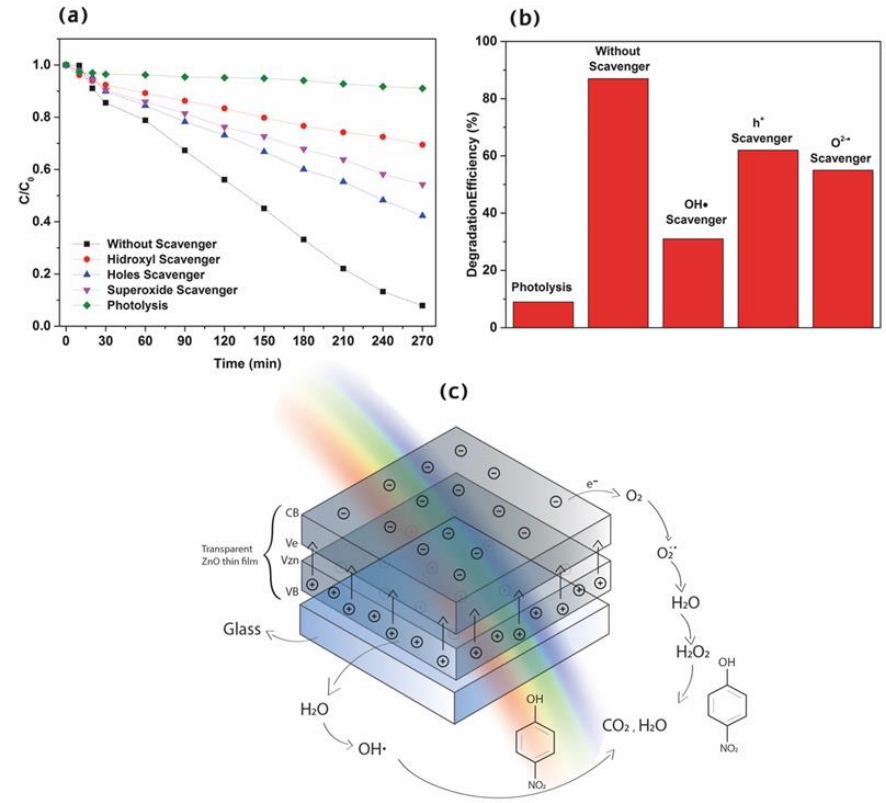

Figure 4.6 The kinetics of the photoreaction using different scavengers were studied on ZnO thin films that allow light to pass through (b) The percentage of degradation efficiency was evaluated using different scavengers on ZnO thin films that are transparent. (c) A visual representation illustrating the mechanism of degradation of 4-NP in the presence of transparent ZnO thin films.

Table 4.1 Comparison of the transparent ZnO thin films behaviour with other recently developed similar ZnO photocatalysts under UV light irradiation.

Samples	Benzoic compounds	[Pollutant] (mg/L)	Amount of photocatalyst (mg)	Removal (%)
This work	4-Nitrophenol (4-NP)	7.0	0.7	94 in 270 min
Nanocrystalline immobilized ZnO [67]	Benzoic Acid (BA)	122.1	unknown	18.3 after 400 min
ZnO powder [68]	Benzoic Acid (BA)	40.0	50	39 after 120 min
ZnO nanoparticles [69]	Tetracycline, (TC)	100.0	50	61.6 after 120 min

Hence, when exposed to UV light, ZnO can absorb photons and generate electron-hole pairs, which can then react with oxygen molecules to produce superoxide radicals ($O_2^{-\bullet}$) and hydroxyl radicals (OH•) through the following equations (4.7- 4.13) [67,68]:

$$ZnO + hv_{UV} \rightarrow ZnO + (e^- + h^+) \quad (4.7)$$

$$H_2O + hv_{UV} \rightarrow H^+ + OH^- \quad (4.8)$$

$$e_{CB}^- + O_2 \rightarrow O_2^- \quad (4.9)$$

$$O_2^- + H^+ \rightarrow HO_2 \quad (4.10)$$

$$HO_2 + e_{CB}^- \rightarrow H_2O_2 \quad (4.11)$$

$$H_2O_2 + e_{CB}^- \rightarrow OH^- + OH\bullet \quad (4.12)$$

$$OH^- + hv_{UV} \rightarrow OH\bullet \quad (4.13)$$

Hydroxyl radicals (OH•) formed in the equations above will attack 4-NP, producing organic radicals or other intermediates. NO_2 is formed and subsequently oxidized to NO_3 [69].

Ultimately, all parent compounds and intermediates will be oxidized into CO_2 according to the following equation (4.14):

$$C_6H_4OHNO_2 + 7O_2 \rightarrow 6CO_2 + H_2O + HNO_3 \quad (4.14)$$

Alternative authors propose that the breakdown of OH• and aromatic molecules occurs through electrophilic addition instead. When 4-NP is present, ortho OH• has the ability to generate 4-nitrocatechol (4-NC).

Scheme 4.1 illustrates a suggested sequence of reactions for the photooxidative deterioration of 4-NP. The combination of 4-NC and OH•, results in the production of 1,2,4-benzenetriol (1,2,4-BT). Subsequent reactions of primary intermediates with OH• lead to ring opening, the formation of oxygenated aliphatic compounds, and the generation of mineralization products. Hydroquinone (HQ), can be formed when OH• directly attacks the nitro group position.

Similar to 4-NC, HQ reacts with OH• to yield 1,2,4-BT. The degradation of 4-NP, leading to the generation of 4-NC and HQ, and its subsequent reaction with OH• to produce 1,2,4-BT, exhibits resemblances to the degradation pathway proposed for the UV/TiO_2 photocatalytic degradation of 4-NP [70,71].

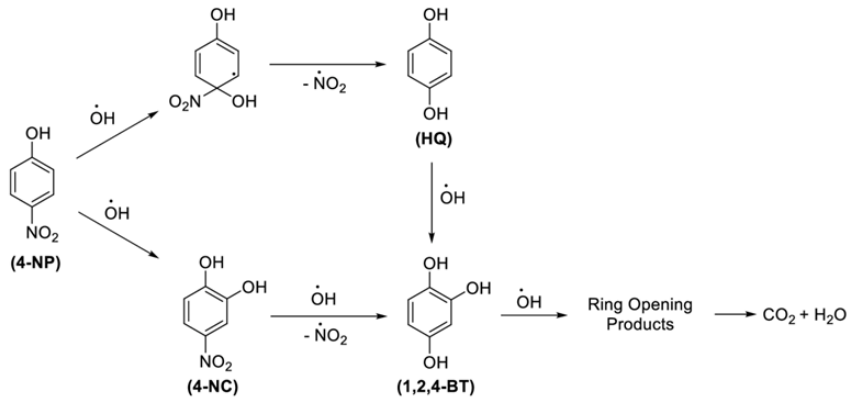

Scheme 4.1 Proposed reaction mechanisms of the 4-NP degradation of by hydroxyl radicals (OH•).

To investigate the stability and reusability of the as-prepared ZnO thin films as photocatalysts, they underwent four photocatalytic cycles (Figure. 4.7(a)).

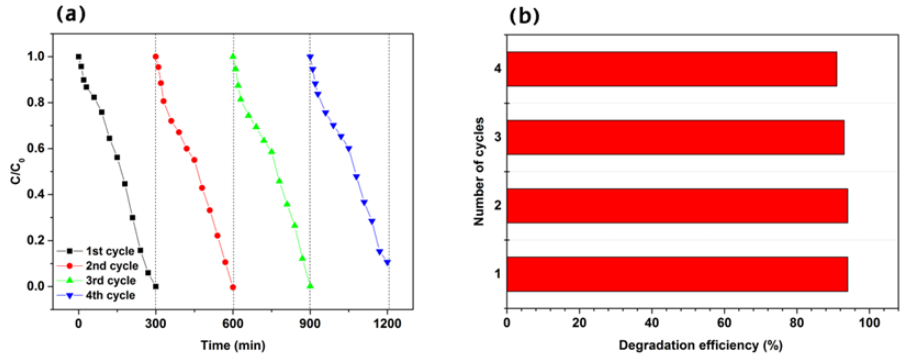

Figure 4.7 (A) Reusability of the thin films in the photocatalytic degradation of 4-NP under UV light irradiation after a total of four cycles, and (b) a bar graph illustrating the percentage of degradation efficiency over four cycles.

In fact, high 4-NP degradation values are still observed after four cycles (90%), as indicated by the bar chart presented in Figure. 4.7(b).

One of the possible explanations for this low decline is due to the adsorption of 4-NP into the active centres of the photocatalyst, which results in a slight reduction in degradation efficiency. Moreover, in order to evaluate the stability of the transparent ZnO thin films, they were immersed in different aqueous solutions at pH 1, 7 and 14 for 24h. The presence of Zn^{2+} ions has been measured by ICP-MS in accordance with the ISO 11885 internal methodology (Table 4.2).

The amount of Zn^{2+} in the supernatant solutions was 0.403 μg/L, which indicates the high stability of the transparent ZnO thin films in an aqueous medium. However, thin film would leach out and be dissolved in the reaction medium when the pH is below 6 due to the HCl, which is able to dissolve the zinc oxide [72]. The high stability of these thin films can be explained by the high adhesion to the glass substrate due to the synthesis method used as well as the high chemical resistance of ZnO [73].

Table 4.2 ICP-OES results of the amount of zinc leached after the leaching screen experiments

pH = 1				
Parameters	Test method	Analytical technique	Result	Units
Zn	Internal method based on ISO 11885	ICP-OES	4826	μg/L
pH = 7				
Zn	Internal method based on ISO 11885	ICP-OES	< 1	μg/L
pH = 14				
Zn	Internal method based on ISO 11885	ICP-OES	< 1	μg/L

4.2.8. Antibacterial activity of transparent ZnO thin films

The antibacterial activity of thin ZnO films was tested, after UV irradiation for 3h, using a standard method (JIS Z 2801_2000) developed for hard surfaces, such as glass. Glass samples were used as reference samples. Also, to evaluate the effect of UV irradiation, tests were conducted under UV light and in the dark, for the same testing time.

After counting the viable cells that were recovered from the surface of the samples, the antibacterial rates were calculated. Results are presented in Figure. 4.8. First, glass and ZnO thin films were compared for any possible antibacterial effect in the dark. Bacterial counts obtained for the two types of samples showed no significantly different antibacterial properties (Figure. 4.8.A). However, after testing the presence of UV light, a significant reduction in cell viability was observed for both samples (Figure. 4.8.A).

The samples, however, showed significantly different behaviours, with a 43.7 and 60.6% reduction in bacterial cells for glass and ZnO thin film, respectively. Results overall show that, when compared with glass surfaces, ZnO thin films make a significant addition to the antibacterial effect induced by UV irradiation of about 17% (Fig. 4.8.B).

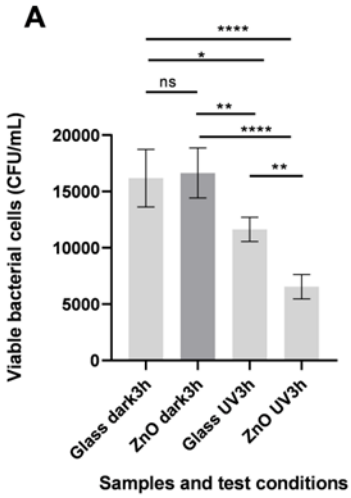

B

Samples	R (%)
Glass UV3h vs ZnO UV3h	43.7
ZnO dark3h vs ZnO UV3h	60.6

Figure 4.8 Antibacterial evaluation of ZnO thin films: (A) Results of colony-forming units per millilitre (CFU/mL) in each sample tested. The significance of the results was determined using one-way ANOVA followed by Tukey's test for multiple comparisons. (B) Antibacterial rates (R) obtained for ZnO thin films compared to glass under UV light and to ZnO samples under dark and UV light.

ZnO nanoparticles in general are described has posing noticeable antibacterial activities [74]. This activity is thought to be caused by the production of ROS, particularly in the presence of light. Also, other effects are possible, like causing membrane damage by accumulation on the cell´s surface, by cell internalization or through Zn^{+} ion release [75].

In this work, thin films produced are not expected to release Zn^{+} ions. Possible mechanism of antibacterial action must therefore come from ROS generation and cell membrane damage, through ZnO thin film contact. The fact that no significant differences were found between glass and thin films, under dark conditions, may imply that, considering the experiment conditions, cell membrane damage and ROS generation were not effective.

But, when testing the same samples after UV exposure, bacterial reduction was observed in both, but significantly greater in thin films. For glass samples, the reduction observed must be due to UV induced damages in membranes, proteins and DNA that affect general cellular processes [76].

The augmented antibacterial activity seen for ZnO thin films can be explained by the combined action with UV causing enhanced ROS generation, toxic to the cells. Synergistic effects to enhance photocatalytic activity of ZnO have already been reported [74]. To the best of our knowledge this is the first evidence obtained on ZnO transparent films holding strong promises of future applications, where additional antimicrobial properties are desired.

4.3. Conclusion

This work presents a simple method of obtaining transparent ZnO thin films on glass, exhibiting an exceptional degree of transparency – over 95%. These thin films have been fabricated to act as photocatalysts for the degradation of water pollutants and bacteria.

It is observed that their stability of these thin films is very high in neutral and basic aqueous media, thanks to the high adhesion of these films to the glass and the high chemical stability of ZnO. It has been shown that these films can generate hydroxyl radicals (OH•) when they are exposed to UV irradiation.

The thin films exhibited high photocatalytic activity with 94% of 4-NP degraded after 270 min. The same catalyst was used for 4 degradation cycles maintaining an activity of 90% in the photodegradation of 4-NP. Comparing the reduction produced by a UV lamp when irradiating normal functionalized glass with these transparent ZnO layers, it was also discovered that radicals increase bacterial cell reduction by 17%.

In future investigations, the evaluation of incorporating nanoparticles (NPs) onto the surface of these transparent thin films, along with the assessment of the films' photocatalytic activity under different light sources (such as visible light or sunlight), can be considered.

4.4 References

[1] F. Maiwald, S. Englmaier, S. Hierl, Absorber-free laser transmission welding of transparent polymers using fixed focus optics and 3D laser scanner, Procedia CIRP. 94 (2020) 686–690. https://doi.org/10.1016/j.procir.2020.09.117.

[2] Y. Ming, Y. Sun, X. Liu, X. Liu, Y. Wu, Optical evaluation of a smart transparent insulation material for window application, Energy Convers. Manag. X. 16 (2022) 100315. https://doi.org/10.1016/j.ecmx.2022.100315.

[3] M. Chutturi, S. Gillela, S.M. Yadav, E.S. Wibowo, K. Sihag, S.M. Rangppa, P. Bhuyar, S. Siengchin, P. Antov, L. Kristak, A. Sinha, A comprehensive review of the synthesis strategies, properties, and applications of transparent wood as a renewable and sustainable resource, Sci. Total Environ. 864 (2023) 161067. https://doi.org/10.1016/j.scitotenv.2022.161067.

[4] D.S. Kim, J.Y. Jung, S. Seo, J.H. Kim, Facile fabrication of multifunctional transparent electrodes via spray deposition of indium-tin-oxide nanoparticles, Appl. Surf. Sci. 611 (2023) 155756. https://doi.org/10.1016/j.apsusc.2022.155756.

[5] E.S. Park, D.Y. Kim, J.H. Lee, J.U. Hwang, Y.S. Song, K.H. Park, H.J. Choi, Optical and electrical properties of amorphous alloy metal mesh for transparent flexible electrodes, Appl. Surf. Sci. 547 (2021) 149109. https://doi.org/10.1016/j.apsusc.2021.149109.

[6] Ryo Morita, Takayuki Nonoyama, Daisuke Abo, Takeshi Soyama, Noriyuki Fujima, Tetsuaki Imai, Hiroyuki Hamaguchi, Takuto Kameda, Osamu Sugita, Bunya Takahashi, Naoya Kinota, Kohsuke Kudo,Mechanical Properties of a 3 Dimensional–Printed Transparent Flexible Resin Used for Vascular Model Simulation Compared with Those of Porcine Arteries,Journal of Vascular and Interventional Radiology,Volume 34, Issue 5,2023,Pages 871-878.e3,ISSN 1051-0443. https://doi.org/10.1016/j.jvir.2023.01.008.

[7] Hashuro MSS, Tupin S, Putra NK, Daibo K, Inoue K, Ishii T, Kosukegawa H, Funamoto K, Hayase T, Ohta M. Development of Ultrasound Phantom Made of Transparent Material: Feasibility of Optical Particle Image Velocimetry. Ultrasound Med Biol. 2023 Jun;49(6):1385-1394. https://doi.org/10.1016/j.ultrasmedbio.2022.12.020

[8] M.S. Kim, Y. Ahn, B.G. Kim, Improvement of scratch resistance in transparent hard surfaces through layer-by-layer coating, Prog. Org. Coatings. 170 (2022) 106991. https://doi.org/10.1016/j.porgcoat.2022.106991.

[9] W. Gao, F. Ma, Y. Yin, J. Li, Robust and durable transparent superhydrophobic F-TNTs/TiN coating fabricated by structure tuning on surface of TiN hard coating, Appl. Surf. Sci. 613 (2023) 155967. https://doi.org/10.1016/j.apsusc.2022.155967.

[10] O.J. Akinribide, G.N. Mekgwe, S.O. Akinwamide, F. Gamaoun, C. Abeykoon, O.T. Johnson, P.A. Olubambi, A review on optical properties and application of transparent ceramics, J. Mater. Res. Technol. 21 (2022) 712–738. https://doi.org/10.1016/j.jmrt.2022.09.027.

[11] A. Macková, A. Jagerová, O. Lalik, R. Mikšová, D. Poustka, J. Mistrík, V. Holý, J.D. Schutter, U. Kentsch, P. Marvan, A. Azarov, A. Galeckas,Combined Au/Ag nanoparticle creation in ZnO nanopillars by ion implantation for optical response modulation and photocatalysis,Applied Surface Science,Volume 610,2023,155556,ISSN 0169-4332. https://doi.org/10.1016/j.apsusc.2022.155556.

[12] Z.S. Shaymardanov, B.N. Rustamova, R. Jalolov, S.Z. Urolov, Influence of the Nature of Defects in Zno Nanocrystals Synthesized by Chemical Bath Deposition on Photocatalytic Activity, SSRN Electron. J. 649 (2022) 414444. https://doi.org/10.2139/ssrn.4211253.

[13] A. Bakour, A. Saadoune, I. Bouchama, F. Dhiabi, S. Boudour, M.A. Saeed, Effect and optimization of ZnO layer on the performance of GaInP/GaAs tandem solar cell, Micro and Nanostructures. 168 (2022) 207294. https://doi.org/10.1016/j.micrna.2022.207294.

[14] S. Yang, H. Yu, The modification of ZnO surface with natural antioxidants to fabricate highly efficient and stable inverted organic solar cells, Chem. Eng. J. 452 (2023) 139658. https://doi.org/10.1016/j.cej.2022.139658.

[15] N.L. Marana, S. Casassa, J.R. Sambrano, Piezoelectricity induced by gaseous molecules adsorbed on ZnO nanotubes, Mater. Sci. Eng. B Solid-State Mater. Adv. Technol. 281 (2022) 115729. https://doi.org/10.1016/j.mseb.2022.115729.

[16] S. Cao, H. Zou, B. Jiang, M. Li, Q. Yuan, Incorporation of ZnO encapsulated MoS_2 to fabricate flexible piezoelectric nanogenerator and sensor, Nano Energy. 102 (2022) 107635. https://doi.org/10.1016/j.nanoen.2022.107635.

[17] S. Ananthi, M. Kavitha, E. Ranjith Kumar, T. Prakash, R. Vandamar Poonguzhali, B. Ranjithkumar, A. Balamurugan, Ch. Srinivas, D.L. Sastry,Investigation of physicochemical properties of ZnO nanoparticles for gas sensor applications,Inorganic Chemistry Communications,Volume 146,2022,110152,ISSN 1387-7003. https://doi.org/10.1016/j.inoche.2022.110152.

[18] H. Zhang, Z. Li, A. Yu, S. Nie, J. Yi, Detection of 2-ethyl hexanol and dioctyl phthalate with potentiometric sensor based on ordered ZnO nanorods sensing electrode, Mater. Lett. 330 (2023) 133330. https://doi.org/10.1016/j.matlet.2022.133330.

[19] D.J. da Silva, A. Duran, A.D. Cabral, F.L.A. Fonseca, R.F. Bueno, D.S. Rosa, Questioning ZnO, Ag, and Ag/ZnO nanoparticles as antimicrobial agents for textiles: Do they guarantee total protection against bacteria and SARS-CoV-2?, J. Photochem. Photobiol. B Biol. 234 (2022) 112538. https://doi.org/10.1016/j.jphotobiol.2022.112538.

[20] Z. Sayyar, H. Jafarizadeh-Malmiri, N. Beheshtizadeh, A study on the anticancer and antimicrobial activity of Curcumin nanodispersion and synthesized ZnO nanoparticles, Process Biochem. 121 (2022) 18–25. https://doi.org/10.1016/j.procbio.2022.06.033.

[21] Luiza A. Gusmão, Diego A. Peixoto, Juliane Z. Marinho, Fernanda C. Romeiro, Rosana F. Gonçalves, Elson Longo, Carlos A. de Oliveira, Renata C. Lima,Alkali influence on ZnO and Ag-doped ZnO nanostructures formation using the microwave-assisted hydrothermal method for fungicidal inhibition,Journal of Physics and Chemistry of Solids,Volume 158,2021,110234,ISSN 0022-3697. https://doi.org/10.1016/j.jpcs.2021.110234.

[22] M. Ali, X. Wang, U. Haroon, H.J. Chaudhary, A. Kamal, Q. Ali, M.H. Saleem, K. Usman, A. Alatawi, S. Ali, M.F. Hussain Munis, Antifungal activity of Zinc nitrate derived nano Zno fungicide synthesized from Trachyspermum ammi to control fruit rot disease of grapefruit, Ecotoxicol. Environ. Saf. 233 (2022) 113311. https://doi.org/10.1016/j.ecoenv.2022.113311.

[23] K.H. Park, G.D. Han, K.C. Neoh, T.S. Kim, J.H. Shim, H.D. Park, Antibacterial activity of the thin ZnO film formed by atomic layer deposition under UV-A light, Chem. Eng. J. 328 (2017) 988–996. https://doi.org/10.1016/j.cej.2017.07.112.

[24] D. Sudha, E. Ranjith Kumar, S. Shanjitha, Alaa M. Munshi, Gamil A.A. Al-Hazmi, Nashwa M. El-Metwaly, S. Jone Kirubavathy,Structural, optical, morphological and electrochemical properties of ZnO and graphene oxide blended ZnO nanocomposites,Ceramics International,Volume 49, Issue 5,2023,Pages 7284-7288,ISSN 0272-8842. https://doi.org/10.1016/j.ceramint.2022.10.192.

[25] Shabbir Awan S, Taj Khan R, Mehmood A, Hafeez M, Rizwan Abass S, Nazir M, Raffi M. Ailanthus altissima leaf extract mediated green production of zinc oxide (ZnO) nanoparticles for antibacterial and antioxidant activity. Saudi J Biol Sci. 2023 Jan;30(1):103487. https://doi.org/10.1016/j.sjbs.2022.103487.

[26] Žigon J, Centa UG, Remškar M, Humar M. Application and characterization of a novel PVDF-HFP/PVP polymer composite with MoO_3 nanowires as a protective coating for wood. Sci Rep. 2023 Mar 1;13(1):3429. https://doi.org/10.1038/s41598-023-30622-y.

[27] Y. Tu, X. Xiao, Y. Dong, J. Li, Y. Liu, Q. Zong, Y. Yuan, Cinnamaldehyde-based poly(thioacetal): A ROS-awakened self-amplifying degradable polymer for enhanced cancer immunotherapy, Biomaterials. 289 (2022) 121795. https://doi.org/10.1016/j.biomaterials.2022.121795.

[28] Y. Zhang, M. Zhou, H. Cheng, S. Luo, Q. Sun, Insight into the substrate-dependent anti-aflatoxigenic effects of nanosized ZnO film: Electron transfer directed oxidative stress mechanisms, Colloids Surfaces B Biointerfaces. 207 (2021) 111997. https://doi.org/10.1016/j.colsurfb.2021.111997.

[29] H. Hong, Z. Liu, S. Li, D. Wu, L. Jiang, P. Li, Z. Wu, J. Xu, A. Jiang, Y. Zhang, Z. Wei, Z. Yang, Zinc oxide nanoparticles (ZnO-NPs) exhibit immune toxicity to crucian carp (Carassius carassius) by neutrophil extracellular traps (NETs) release and oxidative stress, Fish Shellfish Immunol. 129 (2022) 22–29. https://doi.org/10.1016/j.fsi.2022.07.025.

[30] M. Mancinelli, C. Stevanin, M. Ardit, T. Chenet, L. Pasti, A. Martucci, PFAS as emerging pollutants in the environment: A challenge with FAU type and silver-FAU exchanged zeolites for their removal from water, J. Environ. Chem. Eng. 10 (2022) 108026. https://doi.org/10.1016/j.jece.2022.108026.

[31] European Chemicals Agency,ECHA (The European Chemicals Agency), Editor(s):PhilipWexler, Encyclopedia of Toxicology (ThirdEdition), AcademicPress,2014,Pages 263-264, ISBN 9780123864550. https://doi.org/10.1016/B978-0-12-386454-3.00551-0.

[32] J.B. Feng, Y. yuan Li, Y. Zhang, Y. yin Xu, X.W. Cheng, Adsorptive removal of indomethacin and diclofenac from water by polypyrrole doped-GO/COF-300 nanocomposites, Chem. Eng. J. 429 (2022) 132499. https://doi.org/10.1016/j.cej.2021.132499.

[33] J. Mcginley, M.G. Healy, P.C. Ryan, H.O. Driscoll, P. Mellander, L. Morrison, A. Siggins, Science of the Total Environment Impact of historical legacy pesticides on achieving legislative goals in Europe, Sci. Total Environ. 873 (2023) 162312. https://doi.org/10.1016/j.scitotenv.2023.162312.

[34] K. Nozaki, R. Tanoue, T. Kunisue, N.M. Tue, S. Fujii, N. Sudo, T. Isobe, K. Nakayama, A. Sudaryanto, A. Subramanian, K.A. Bulbule, P. Parthasarathy, L.H. Tuyen, P.H. Viet, M. Kondo, S. Tanabe, K. Nomiyama, Pharmaceuticals and personal care products (PPCPs) in surface water and fish from three Asian countries: Species-specific bioaccumulation and potential ecological risks, Sci. Total Environ. 866 (2023) 161258. https://doi.org/10.1016/j.scitotenv.2022.161258.

[35] L.B.B. Ndong, M.P. Ibondou, Z. Miao, X. Gu, S. Lu, Z. Qiu, Q. Sui, S.M. Mbadinga, Efficient dechlorination of chlorinated solvent pollutants under UV irradiation by using the synthesized TiO_2 nano-sheets in aqueous phase, J. Environ. Sci. (China). 26 (2014) 1188–1194. https://doi.org/10.1016/S1001-0742(13)60541-0.

[36] A.A. Essawy, I.B. Abdel-Farid, Hybrid solvothermal/sonochemical-mediated synthesis of ZnO NPs generative of OH radicals: Photoluminescent approach to evaluate [rad]OH scavenging activity of Egyptian and Yemeni Punica granatum arils extract, Ultrason. Sonochem. 89 (2022) 106152. https://doi.org/10.1016/j.ultsonch.2022.106152.

[37] M.N. Rezaie, S. Mohammadnejad, S. Ahadzadeh, The impact of ZnO nanotube on the performance of hybrid inorganic/organic light-emitting diode as a single-mode ring-core UV waveguide, Surfaces and Interfaces. 28 (2022) 101666. https://doi.org/10.1016/j.surfin.2021.101666.

[38] B.J. Lee, S. Il Jo, S.G. Heo, W.Y. Lee, G.H. Jeong, Structure-controllable synthesis of ZnO nanowires using water vapor in an atmospheric-pressure microwave plasma system, Curr. Appl. Phys. 28 (2021) 52–58. https://doi.org/10.1016/j.cap.2021.05.004.

[39] L. Demelius, M. Blatnik, K. Unger, P. Parlanti, M. Gemmi, A.M. Coclite, Shedding light on the initial growth of ZnO during plasma-enhanced atomic layer deposition on vapor-deposited polymer thin films, Appl. Surf. Sci. 604 (2022) 154619. https://doi.org/10.1016/j.apsusc.2022.154619.

[40] P.P. Fu, Q. Xia, H.M. Hwang, P.C. Ray, H. Yu, Mechanisms of nanotoxicity: Generation of reactive oxygen species, J. Food Drug Anal. 22 (2014) 64–75. https://doi.org/10.1016/j.jfda.2014.01.005.

[41] Cuadra, J.G.; Scalschi, L.; Vicedo, B.; Guc, M.; Izquierdo-Roca, V.; Porcar, S.; Fraga, D.; Carda, J.B. ZnO/Ag Nanocomposites with Enhanced Antimicrobial Activity. Appl. Sci. 2022, 12, 5023. https://doi.org/10.3390/app12105023

[42] Jaleh B, Hamzehi S, Sepahvand R, Azizian S, Eslamipanah M, Golbedaghi R, Meidanchi A, Fausto R. Preparation of Polycarbonate-ZnO Nanocomposite Films: Surface Investigation after UV Irradiation. Molecules. 2022 Jul 12;27(14):4448. https://doi.org/10.3390/molecules27144448.

[43] Ammar Nayfeh, Nazek El-Atab,Chapter 6 - Agglomeration-based nanoparticle fabrication,In Micro and Nano Technologies,Nanomaterials-Based Charge Trapping Memory Devices,Elsevier,2020,Pages 133-153,ISBN 9780128223420. https://doi.org/10.1016/B978-0-12-822342-0.00006-7.

[44] Alfina Grasso, Margherita Ferrante, Antonio Moreda-Piñeiro, Giovanni Arena, Riccardo Magarini, Gea Oliveri Conti, Antonio Cristaldi, Chiara Copat,Dietary exposure of zinc oxide nanoparticles (ZnO-NPs) from canned seafood by single particle ICP-MS: Balancing of risks and benefits for human health,Ecotoxicology and Environmental Safety,Volume 231,2022,113217,ISSN 0147-6513. https://doi.org/10.1016/j.ecoenv.2022.113217.

[45] L. Liu, H. Nian, T. Lian, Plants and rhizospheric environment: Affected by zinc oxide nanoparticles (ZnO NPs). A review, Plant Physiol. Biochem. 185 (2022) 91–100. https://doi.org/10.1016/j.plaphy.2022.05.032.

[46] S.W. Bian, I.A. Mudunkotuwa, T. Rupasinghe, V.H. Grassian, Aggregation and dissolution of 4 nm ZnO nanoparticles in aqueous environments: Influence of pH, ionic strength, size, and adsorption of humic acid, Langmuir. 27 (2011) 6059–6068. https://doi.org/10.1021/la200570n.

[47] S.Y. Lee, D. Park, B.S. Yoon, Y.S. Lee, Y. Il Park, C.H. Ko, Atomic layer deposition-based synthesis of TiO_2 and Al_2O_3 thin-film coatings on nanoparticle powders for sodium-ion batteries with enhanced cyclic stability, J. Alloys Compd. 897 (2022) 163113. https://doi.org/10.1016/j.jallcom.2021.163113.

[48] S.I. Dorovskikh, D.D. Klyamer, A.M. Makarenko, K. V. Zherikova, A.E. Turgambaeva, Y. V. Shevtsov, D.B. Kal'nyi, I.K. Igumenov, N.B. Morozova, The comprehensive study of thermal properties of tris(2,2,6,6-tetramethyl-3,5-heptanedionato)cobalt(III) related to the chemical vapor deposition of Co-oxide based thin film materials, Vacuum. 199 (2022) 110969. https://doi.org/10.1016/j.vacuum.2022.110969.

[49] V.T. Lukong, R.T. Mouchou, G.C. Enebe, K. Ukoba, T.C. Jen, Deposition and characterization of self-cleaning TiO_2 thin films for photovoltaic application, Mater. Today Proc. (2022). https://doi.org/10.1016/j.matpr.2022.02.089.

[50] R.S. Santiago, L.C.D. Silva, F.D. Origo, C. Stegemann, I.L. Graff, R.G. Delatorre, D.A. Duarte,Target power influence on optical and electrical properties of amorphous titanium oxide deposited by reactive grid-assisted magnetron sputtering,Thin Solid Films,Volume 700,2020,137917,ISSN0040-6090. https://doi.org/10.1016/j.tsf.2020.137917.

[51] K. Vijayan, S.P. Vijayachamundeeswari, K. Sivaperuman, N. Ahsan, T. Logu, Y. Okada, A review on advancements, challenges, and prospective of copper and non-copper based thin-film solar cells using facile spray pyrolysis technique, Sol. Energy. 234 (2022) 81–102. https://doi.org/10.1016/j.solener.2022.01.070.

[52] A.L. Patterson, The scherrer formula for X-ray particle size determination, Phys. Rev. 56 (1939) 978–982. https://doi.org/10.1103/PhysRev.56.978.

[53] T. Ratana, P. Amornpitoksuk, T. Ratana, S. Suwanboon, The wide band gap of highly oriented nanocrystalline Al doped ZnO thin films from sol-gel dip coating, J. Alloys Compd. 470 (2009) 408–412. https://doi.org/10.1016/j.jallcom.2008.02.081.

[54] J.T. Schneider, D.S. Firak, R.R. Ribeiro, P. Peralta-Zamora, Use of scavenger agents in heterogeneous photocatalysis: truths, half-truths, and misinterpretations, Phys. Chem. Chem. Phys. 22 (2020) 15723–15733. https://doi.org/10.1039/d0cp02411b.

[55] T. Liu, L. Wang, X. Lu, J. Fan, X. Cai, B. Gao, R. Miao, J. Wang, Y. Lv, Comparative study of the photocatalytic performance for the degradation of different dyes by $ZnIn_2S_4$: adsorption, active species, and pathways, RSC Adv. 7 (2017) 12292–12300. https://doi.org/10.1039/c7ra00199a.

[56] J.G. Cuadra, S. Molina-Prados, G. Mínguez-Vega, A.C. Estrada, T. Trindade, C. Oliveira, M.P. Seabra, J. Labrincha, S. Porcar, R. Cadena, D. Fraga, J.B. Carda, Multifunctional Silver-Coated Transparent TiO_2 Thin Films for Photocatalytic and Antimicrobial Applications, Appl. Surf. Sci. 617 (2023) 156519. https://doi.org/10.1016/j.apsusc.2023.156519.

[57] X. Bai, B. Sun, X. Wang, T. Zhang, Q. Hao, B.J. Ni, R. Zong, Z. Zhang, X. Zhang, H. Li, Defective crystal plane-oriented induced lattice polarization for the photocatalytic enhancement of ZnO, CrystEngComm. 22 (2020) 2709–2717. https://doi.org/10.1039/c9ce01966a.

[58] S.H. Ribut, C.A. Che Abdullah, M.Z. Mohammad Yusoff, Investigations of structural and optical properties of zinc oxide thin films growth on various substrates, Results Phys. 13 (2019) 102146. https://doi.org/10.1016/j.rinp.2019.02.082.

[59] R. Cuscó, E. Alarcón-Lladó, J. Ibáñez, L. Artús, J. Jiménez, B. Wang, M.J. Callahan, Temperature dependence of Raman scattering in ZnO, Phys. Rev. B - Condens. Matter Mater. Phys. 75 (2007) 1–11. https://doi.org/10.1103/PhysRevB.75.165202.

[60] H. Ali, A.M. Alsmadi, B. Salameh, M. Mathai, M. Shatnawi, N.M.A. Hadia, E.M.M. Ibrahim, Influence of nickel doping on the energy band gap, luminescence, and magnetic order of spray deposited nanostructured ZnO thin films, J. Alloys Compd. 816 (2020) 152538. https://doi.org/10.1016/j.jallcom.2019.152538.

[61] M.R. Al Hassan, Asrafuzzaman, M.A. Islam, K. Salam, K.F. Amin, M.K. Hasan, Synthesis of spray deposited transition metals doped (Cr, Mn, Fe, Ni, and Cu) compositionally complex ZnO thin films with enhanced band gap and magnetism, Results Mater. 13 (2022). https://doi.org/10.1016/j.rinma.2022.100263.

[62] C. Jin, X. Yang, X. Zhai, S. Wang, W. Zhang, Applied Surface Science ZnO / Sn_3O_4 amorphous-crystalline heterojunctions for Cr(VI) visible photocatalysis : Simple synthesis with excellent performance, Appl. Surf. Sci. 608 (2023) 155263. https://doi.org/10.1016/j.apsusc.2022.155263.

[63] L. Zhang, B. Liang, H. Zhao, J. Yang, M. Jiao, Y. Liu, Core-shell structured ZnO homojunction for enhanced photocatalysis, Inorg. Chem. Commun. 148 (2023) 110281. https://doi.org/10.1016/j.inoche.2022.110281.

[64] R.D. Suryavanshi, S.V. Mohite, A.A. Bagade, S.K. Shaikh, J.B. Thorat, K.Y. Rajpure,Nanocrystalline immobilised ZnO photocatalyst for degradation of benzoic acid and methyl blue dye,Materials Research Bulletin,Volume 101,2018,Pages324-333,ISSN:0025-5408. https://doi.org/10.1016/j.materresbull.2018.01.042.

[65] A. Fertier, A. Montarnal, S. Truptil, F. Bénaben, Decis. Support Syst. (2020) 113260. https://doi.org/10.1016/j.ceramint.2023.03.024.

[66] Y. Hu, L. Sun, Z. Liu, T. Liu, Controlled solvothermal synthesis of ZnO nanoparticles using non-destructive Mg-based channel templates for enhanced photocatalytic performance, Mater. Chem. Phys. 299 (2023) 127525. https://doi.org/10.1016/j.matchemphys.2023.127525.

[67] J. Zheng, Z.J. Ã, Q.K. Ã, Z. Xie, R. Huang, L. Zheng, Journal of Solid State Chemistry Shape-controlled fabrication of porous ZnO architectures and their photocatalytic properties, 182 (2009) 115–121. https://doi.org/10.1016/j.jssc.2008.10.009.

[68] Subrata Naskar, S. Arumugom Pillay, Manas Chanda,Photocatalytic degradation of organic dyes in aqueous solution with TiO_2 nanoparticles immobilized on foamed polyethylene sheet,Journal of Photochemistry and Photobiology A: Chemistry,Volume 113, Issue 3,1998,Pages 257-264,ISSN 1010-6030. https://doi.org/10.1016/S1010-6030(97)00258-X.

[69] Dingwang Chen, Ajay K. Ray,Photodegradation kinetics of 4-nitrophenol in TiO_2 suspension,Water Research,Volume 32, Issue 11,1998,Pages 3223-3234,ISSN 0043-1354. https://doi.org/10.1016/S0043-1354(98)00118-3.

[70] N. Daneshvar, M.A. Behnajady, Y. Zorriyeh Asghar, Photooxidative degradation of 4-nitrophenol (4-NP) in UV/H_2O_2 process: Influence of operational parameters and reaction mechanism, J. Hazard. Mater. 139 (2007) 275–279. https://doi.org/10.1016/j.jhazmat.2006.06.045.

[71] Guanhua Zhang, Jieyi Yang, Zhiling Huang, Guoxiang Pan, Bo Xie, Zheming Ni, Shengjie Xia,Construction dual vacancies to regulate the energy band structure of $ZnIn_2S_4$ for enhanced visible light-driven photodegradation of 4-NP,Journal of Hazardous Materials,Volume 441,2023,129916,ISSN 0304-3894. https://doi.org/10.1016/j.jhazmat.2022.129916.

[72] G. Brunner, Chapter 3: properties of mixtures with water, Supercrit. Fluid Sci. Technol. (2014), pp. 95–225. https://doi.org/10.1016/B978-0-444-59413-6.000030.

[73] R. Saidi, K. Raeissi, F. Ashrafizadeh, M. Kharaziha, The effect of zinc oxide coating morphology on corrosion performance of Ti-6Al-4 V alloys, J. Alloys Compd. 883 (2021) 160771. https://doi.org/10.1016/j.jallcom.2021.160771.

[74] K. Qi, B. Cheng, J. Yu, W. Ho, Review on the improvement of the photocatalytic and antibacterial activities of ZnO, J. Alloys Compd. 727 (2017) 792–820. https://doi.org/10.1016/j.jallcom.2017.08.142.

[75] A.B. Djurišić, X. Chen, Y.H. Leung, A. Man Ching Ng, ZnO nanostructures: Growth, properties and applications, J. Mater. Chem. 22 (2012) 6526–6535. https://doi.org/10.1039/c2jm15548f.

[76] F. Vatansever, C. Ferraresi, M.V.P. de Sousa, R. Yin, A. Rineh, S.K. Sharma, M.R. Hamblin, Can biowarfare agents be defeated with light?, Virulence. 4 (2013) 796–825. https://doi.org/10.4161/viru.26475.

CHAPTER 5

Multifunctional Silver-Coated Transparent TiO_2 Thin Films for Photocatalytic and Antimicrobial Applications

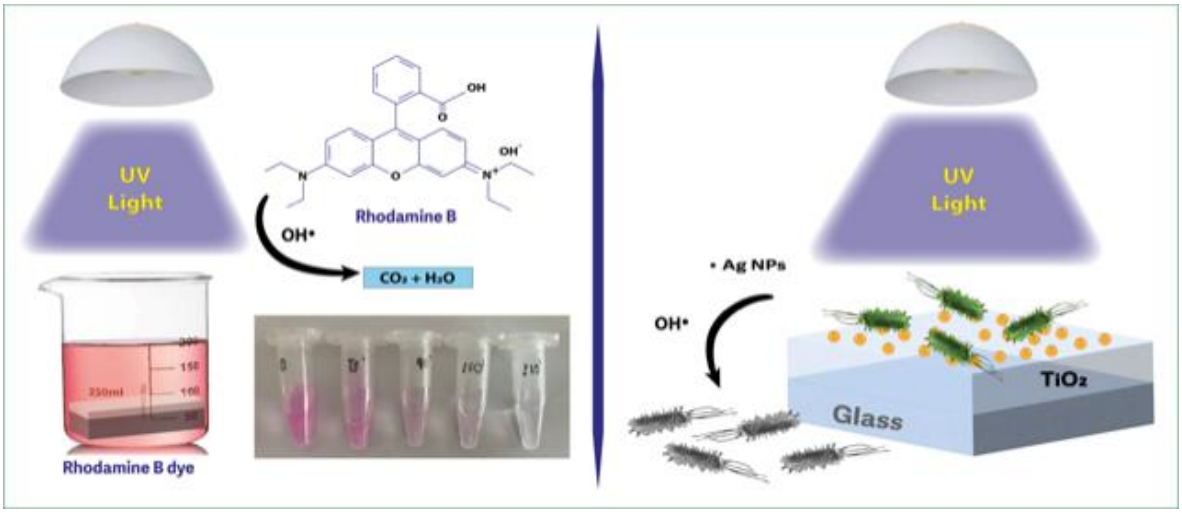

J.G. Cuadra, S. Molina-Prados, G. Mínguez-Vega, A.C. Estrada, T. Trindade, C. Oliveira, M.P. Seabra, J. Labrincha, S. Porcar, R. Cadena, D. Fraga, J.B. Carda, Multifunctional Silver-Coated Transparent TiO_2 Thin Films for Photocatalytic and Antimicrobial Applications, Appl. Surf. Sci. 617 (2023) 156519. https://doi.org/10.1016/j.apsusc.2023.156519.

"We stand on the threshold that offers exciting opportunities to solve problems that once seemed unsolvable"

Chistopher L. Henly

Abstract: Transparent TiO_2 thin films coated with Ag NPs were synthesized using two industrially applicable techniques,pulsed laser ablation (PLAL) and spray pyrolysis without using high vacuum. These transparent thin films were deposited on glass in order to generate glass materials with photocatalytic and antimicrobial properties and a minimum loss of transparency. The structural, morphological and optical properties of the thin films were examined using Grazing incidence X-ray diffraction (GIXRD), Raman spectroscopy, Scanning electron microscopy (SEM) and ultraviolet-visible spectroscopy. Transmission electron microscopy (TEM) was used to identify the NPs on the TiO_2 surface. The transmittance value for the thin films was greater than 80%. The thin films thus synthesized were then assessed to determine their photocatalytic capacity by monitoring the degradation of Rhodamine B (RhB) under UV light irradiation. Ag NPs on the TiO_2 surface ensures an improvement in the photocatalytic properties, with a 99% degradation of RhB in 210 minutes under UV light. In addition, these transparent thin films showed high antimicrobial activity on Gram-negative bacteria when irradiated by UV light for 4 hours, killing 93% of these bacteria.

5.1. Introdution

Over the past few years, the interest in thin film technology has grown greatly due to its wide range of applications such as photovoltaic solar cells [1], gas sensors [2], energy storage [3], heterogeneous photocatalysis for water splitting processes [4] or antimicrobial action [5].

In addition, as a consequence of the COVID-19 pandemic, the development of antivirus and antimicrobial materials has become increasingly relevant all over the world. Accordingly, the possibility of being able to functionalize diverse types of surfaces without changing their optical properties has become a priority. There are many methods to obtain thin films including electroplating [6], anodic treatment [7], chemical vapor deposition (CVD) [8], atomic layer deposition (ALD) , or spin coating [9].

All of them are difficult to adapt to industry due to the fact that they are techniques that need a high vacuum or are technically very sophisticated. The spray pyrolysis method is the most readily applicable to industry because it offers an easy way to make films with any material in any quantity by simply adding it to the spray precursor solution.

Moreover, it does not need a vacuum to be applied or eminence targets and quality substrates, which could be a fine advantage if the method is to be scaled up [10].

One of the most widely studied materials in thin films is titanium oxide (TiO_2) because it shows tunable behavior depending on the preparation method used [11]. By changing the preparation conditions, distinct structural polymorphs and different degrees of crystallinity [12] or amorphousness [13] can be obtained.

When it is in its crystalline form, the crystal size take on special importance, and even more so if photocatalysis is being studied. On the other hand, the different polymorphic phases of TiO_2 (rutile, anatase) are of great importance in the application of the material. The anatase-rutile transition occurs at high temperatures (600ºC-700ºC). The absorption in the diverse phases is different, and hence the value of the band gap for anatase is 3.2-3.9 eV [14] and the value of the band gap for the rutile phase is 3.0-3.57 eV [15].

However, the anatase phase only absorbs in the ultraviolet spectrum (UV), and thus strategies to red-shift the absorbance range have been explored, namely by varying the morphology of the crystals [16], introducing transition metals as dopants [17] or generating nanocomposites [18].

In this context, the binding of metal nanoparticles to semiconductors such as ZnO or TiO_2 to form Schottky Barriers due to the excellent photoelectric response it exhibited has already been reported by other authors [19,20]. Furthermore, Ag is a well-known antimicrobial agent and consequently its presence on the surface of thin films of metal oxides improves the antimicrobial activity [21].

Although there are many protocols available for nanoparticle synthesis, Pulsed Laser Ablation in Liquids (PLAL) was selected due to the simplicity of the technique [22–24]. In PLAL, the interaction of the laser radiation with a target immersed in a liquid promotes the extraction of material from the surface of the target through the formation of nanoparticles that are collected in the liquid as colloids.

The technique allows synthesis of nanoparticles from a broad library of available materials and provides nanomaterials with a high degree of purity, since only the solvent and desired material are required, thereby avoiding the presence and generation of toxic or hazardous adducts and byproducts, and providing electrostatically stabilized colloids for noble metals.

In the framework of the cost-effective and green development of nanotechnologies this synthesis route provides key advantages, such as as running at room temperature and ambient pressure [25] and a high production (grams per hour) compatible with industrial applications [26].

Moreover, different techniques have been adopted to adapt the beam delivery system to improve the efficiency of the process [27,28].

Additionally, to the best of the authors' knowledge the combination of these two techniques for the formation of transparent layers with nanoparticles has not been previously reported.

In this work, a facile synthesis method was used to prepare transparent TiO_2 and TiO_2-Ag NPs thin films where Ag NPs were placed on the surface of TiO_2 thin films with the aim of improving the photocatalytic and antimicrobial properties.

5.2. Experimental section

5.2.1 Materials

Titanium(IV) bis(acetylacetonate) diisopropoxide ($[(CH_3)_2CHO]_2Ti(C_5H_7O_2)_2$ 75 wt. % in isopropanol, Sigma-Aldrich), ethanol (EtOH, Scharlau), Ammonia 30% (w/w) (NH_3, PanReactAppliChem) and deionized water with pH of 6.9 ± 0.2.

The dye (purchased through Fraga Lab, Mexico) used to test the photocatalytic activity of the TiO_2 was Rhodamine B (RhB), with an Mw of 479.01 g/mol, and a purity of 95%.

Milli-Q deionized water with a resistivity of 18.2 MΩ-cm (Ultramatic Plus, Wasserlab, Spain) and ultrapure silver foil (Silver, Aldrich Chemistry) were used for colloid synthesis.

Tert-butyl alcohol (t-BuOH), formic acid (HCOOH) and 1,4-Benzoquinone ($C_6H_4O_2$) (99%, purity) were acquired from Sigma-Aldrich.The dye (purchased through Fraga Lab, Mexico) used to test the photocatalytic activity of the TiO_2 was Rhodamine B (RhB), with an Mw of 479.01 g/mol, and a purity of 95%.

Milli-Q deionized water with a resistivity of 18.2 MΩ-cm (Ultramatic Plus, Wasserlab, Spain) and ultrapure silver foil (Silver, Aldrich Chemistry) were used for colloid synthesis. Tert-butyl alcohol (t-BuOH), formic acid (HCOOH) and 1,4-Benzoquinone ($C_6H_4O_2$) (99%, purity) were acquired from Sigma-Aldrich.

5.2.2 Methods

The crystalline structure of transparent thin films composed of TiO_2 and TiO_2-Ag NPs was studied using Grazing incidence X-ray diffraction (GIXRD) measurements. An X-ray diffractometer (D4 Endeavor, Burker-ASX) armed with a Cu Kα radiation source was used. Data were obtained by step-scanning from 20º to 80º with a step size of 0.05º 2θ and 3s counting time per step.

The measurements were accomplished at a grazing-incident angle greater than the so-called critical angle for total external reflection at which X-rays penetrate the sample. The critical angle (around 1º) was determined through testing.

Scanning Electron Microscopy (SEM), performed on JEOL 7001F equipment, was engaged to study the surface, the sectional morphology and the thickness of the films. SEM-EDS mappings were recorded at an acceleration voltage of 12 kV and a moderate beam current of 0.8 nA. Spectra were recorded at a step size of 0.3 μm and a low dwell time of 0.3 msec using drift correction. The software package Aztec 4.3 (Oxford Instruments, UK) was used to record the EDS analyses.

The layer thickness was determined from cross-section micrographs. Transmission electron microscopy (TEM) was performed using a Hitachi H-9000 TEM microscope (Chiyoda, Tokyo, Japan) carried out at an accelerating voltage of 300 kV.

The thin layer was removed with a micro-blade and then dispersed in EtOH. A drop (10 µL) of a suspension of the removed thin film dispersed in ethanol was placed on a copper grid with a lacey amorphous carbon film and left to dry before TEM analysis.

Raman studies were conducted using a combined Raman–AFM-SNOM confocal microscope WiTec alpha300 RAS + with an Nd:YAG laser operating at 532 nm (35 mW) and a He:Ne laser operating at 633 nm (25 mW) as excitation sources.

Ultraviolet-visible diffuse reflectance spectroscopy (DRS) was measured using a UV-Vis spectrophotometer (JASCO U-560 UV-Vis spectrophotometer).

Fourier transform infrared (FTIR) spectra of the particles were measured in the solid state. The spectra of the materials were collected using a Bruker Optics Tensor 27 spectrometer coupled to a horizontal attenuated total reflectance (ATR) cell using 256 scans at a resolution of 4 cm^{-1}. For the photocatalyst leaching study an ICP-OES Jobin Yvon Activa M was used.

5.2.3 Synthesis of transparent TiO_2-Ag NPs thin films.

Synthesis of transparent TiO_2 thin films: 2.6 mL of titanium (IV) bis(acetylacetonate) diisopropoxide (75 w.t % in isopropanol) was mixed with 20 mL of EtOH. This mixture of precursors was agited for 1h to ensure the homogeneity of the solution. The concentration of the final solution was 0.2 M.

After mixing for 30 min the solution was applied by hand using a dual action gravity feed airbrush with a flow rate of 5.75 mL/min was used to apply the solution onto a soda-lime glass substrate (Figure.S1) previously heated to 450ºC.

Prior to heating, it was cleaned by introducing the glass into a 30% (w/w) NH_3 solution and placing them in an ultrasonic bath for 20 min.

The thin films thus deposited were then heated to 550ºC under atmospheric pressure on a hot plate to increase their crystallinity and remove any organic residue from the transparent thin film.

Synthesis of Ag NPs: Colloidal NPs were synthesized using the PLAL technique [23,24]. The experimental setup is shown in Figure. S1 and it is based on a home made semi-batch configuration. The main elements are the pulsed laser, the irradiation zone, and the peristaltic pump.

The laser irradiation was carried out using the second harmonic of an Nd:YAG pulsed laser (Brilliant, Quantel), with a pulse width of 4 ns full width at half maximum at a fundamental wavelength of 1064 nm and a repetition rate of 10 Hz.

A 650 mW mean power laser beam is focused with a 75 mm focal lens (Figure.S2). The irradiation zone is formed by a plastic vessel containing Milli-Q water in which the ultrapure silver foil was immersed. The vessel was attached to a two-dimensional motion-controlled stage moving at a constant speed of 2.5 mm/s in the focus plane perpendicular to the laser beam, where the silver foil was placed, in a raster scanning pattern.

To remove nanoparticles and bubbles from the ablation area, and thus enhance productivity, a peristaltic pump (Watson Marlow 323) was used at 60 rpm for the circulation of the 350 mL of water. The irradiation time was of 4 hours. This process allowed us to obtain a productivity of 3.1 mg/h. After the fabrication, the concentration of the silver colloid was measured by means of a UV-Vis spectroscopy [29] providing a concentration of 11.52 mg/L, which is optimal for use on transparent TiO_2 thin films.

In the fabrication of transparent TiO_2-Ag NPs thin films, a physical assembly was applied to load Ag NPs onto TiO_2 thin films. 2 mL of the water solution of Ag NPs was mixed with 15 mL of EtOH. After mixing the solution for 30 min, it was applied by airbrush. In order to calculate the stabilisation of the Ag NPs, the Zeta Potential technique was used.

The Zeta Potential and the stability of Ag NPs vary depending on the pH of the solution where the colloid is prepared. In this case, for a water solution with a pH of 6.9, the ±30 mV is an important limit for the colloid stability [30]. As can be seen in Figure.S3, the maximum value obtained by this technique was -31.2 mV.

This value exceeds the limit established to determine the stability of the NPs. This allows us to ensure that the stability of the Ag NPs colloid is correct. The flow rate was 5.75 mL/min on a soda-lime glass substrate (2.5 × 2.5 cm) previously heated to 250ºC to remove the dispersant and improve the adhesion of NPs on the TiO_2 thin film. The appearance of the transparent TiO_2 and TiO_2-Ag NPs thin films are shown in Figure.S4. The total amount of silver on the surface of the film was 0.0251 mg.

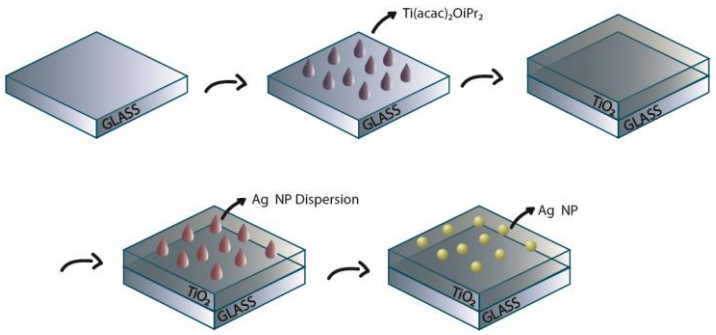

Figure 5.1 Formation process of transparent TiO_2-Ag NPs thin films on soda-lime glass.

5.2.4 Photocatalytic screening experiments

The RhB photodegradation experiments were performed under illumination using UV light illumination to evaluate the photocatalytic properties of the transparent thin film samples. The prepared thin films (2.5 × 2.5 cm) were immersed in a glass reactor with a 30 mL RhB solution (5 mg/L) and stirred in the dark for 30 min to ensure an dsorption/desorption equilibrium was accomplished.

The samples were then placed under UV light lamp (SUPRATECH HTC 150-211 UV, Osram) with a power of 22W for the UVA wavelength (315-400 nm) and 6W for the UVB wavelength (280-315 nm).

Nominal power was 150W and light intensity is 0.105 W/cm^2. The experimental set-up of the photocatalysis is shown in Figure.S5. Measurements of the degradation of pollutants exposed to UV light were analyzed every 10 min for the first 30 min and every 30 min afterwards, and the concentration of RhB was monitored by UV-Vis spectroscopy at 554 nm, using the following equation (5.1):

$$\eta\ (\%) = \left(1 - \frac{C_t}{C_0}\right) \times 100 \qquad (5.1)$$

where C_0 represents the initial RhB concentration and Ct refers to the real time concentrations of RhB, respectively.

The reusability test of the transparent TiO_2 and TiO_2-Ag NPs thin film catalyst was investigated, despite the possibility of the thin film being separated from the glass or leaching of the material into the RhB solution to be photodegraded.

For this purpose, the same photodegradation study was carry out with the 5 mg/L solution of RhB using the same catalyst for four and its degradation efficiency (%) was studied.

5.2.5 In situ capture experiment

In situ capture experiments were carried out to investigate the active species generated during the photocatalytic process of TiO_2 and TiO_2-Ag NPs. Tert-butyl alcohol (t-BuOH), formic acid (FA), and 1,4-Benzoquinone (1,4-BQ) were used to capture hydroxyl radicals (OH•), holes (h^+) and superoxide radicals ($O_2^{-\bullet}$), respectively [19,20]. The concentration of the formic acid, 2,4-benzoquinone and tert-butyl alcohol were 1mmol L^{-1} in 30 mL reaction solution.

5.2.6 Determination of antibacterial activity

The antibacterial activity of the transparent TiO_2 and TiO_2-Ag NPs thin films was evaluated in accordance with the standard method test Jisz 2801_2000, with modifications. Escherichia coli ATCC 25922 was used as the reference bacterial strain.

Fresh bacterial cells were grown overnight at 37ºC in LB (Luria broth) culture media. A cell suspension (100µl) of approximately 4×105 cells/mL was placed over each sample and carefully covered with a film.

Reference samples were glass, and TiO_2 treated samples. Samples were then placed under UV light, with an intensity of 0.05 mW/cm^2 for 4 hours and viable bacterial cells were quantified by the spread plate method. Two samples of each were tested and three plates were prepared for bacterial counts.

Also, as a reference, cell suspension was placed over glass sample, covered with film, and immediately retrieved and plated using the same bacterial cell counts.

Plates were incubated for 16h at 37ºC and colony forming units (CFU) counted.The antibacterial rate (R) was calculated according to equation (5.2):

$$(\mathrm{R}) = (N_0 - \mathrm{N})/N_0 \times 100 \qquad (5.2)$$

where N_0 represents the average number of viable bacteria on a reference sample, and N is the average number of bacteria on samples treated with TiO_2-Ag NPs.

5.3. Results and discussion

5.3.1 Characterization of transparent TiO_2-Ag NPs thin films

GIXRD analyses of TiO_2 and TiO_2-Ag NPs are shown in Figure. 2. The 2θ values at 25.3, 48.0, 52.8, 55.0, 62.6, and 75.0^0 are those of the crystalline planes (101), (200), (105), (211), (204) and (215) of the anatase polymorph, based on the file 01-071-1166 of the JCPDS [31,32].

Moreover, the peak observed at 44.3^0 represents to the Ag cubic crystalline phase associated with the crystalline plane (200) based on the file 03-065-2871 of the JCPDS.

The peaks corresponding to the silver oxide are also observed at 32.1^0 and 53.8^0, corresponding to the (111) and (220) crystalline planes, based on the file 01-076-1489 of the JCPDS. The partial oxidation of some of the Ag NPs is due to the temperature of the substrate when deposited onto the TiO_2 thin films [33].

The GIXRD results showed that the bulk structure of the anatase was not affected by the Ag NPs, since they were located only on its TiO_2 surface [34].

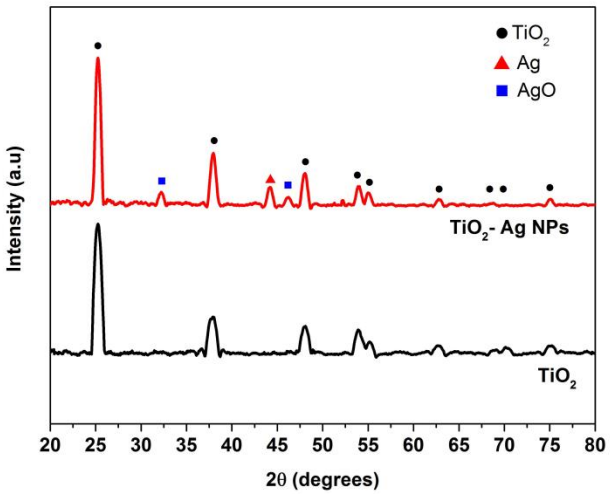

Figure 5.2 GIXRD pattern of transparent TiO_2 and TiO_2-Ag NPs thin films

Figure. 5.3(a) and Figure. 5.3(b) show cross-section images of the transparent TiO_2 and TiO_2 Ag NPs thin films. The thickness is the same in both cases, i.e, around 300 nm.

The layers formed in them are compact and dense. Figure. 5.3(c) shows the top surface texture of the TiO_2 films, revealing their continuity.

Figure. 5.3(d) shows EDS spectra for the TiO_2 thin films as well as the composition of the glass on which they are deposited. Elements from the soda-lime glass substrate (Si,Ca,Mg) were also detected.

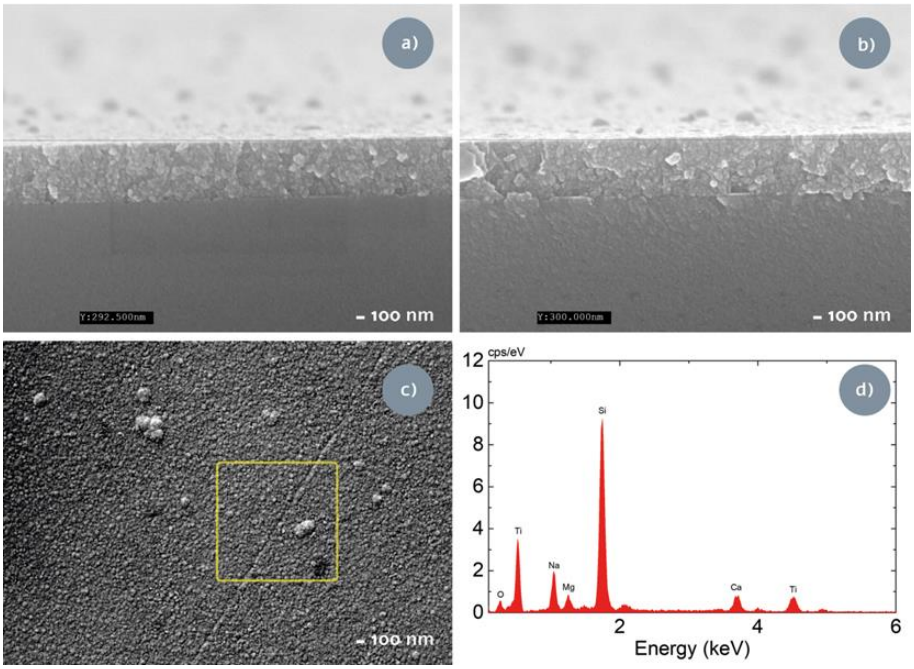

Figure 5.3 SEM images for the cross section of(a) TiO_2 transparent thin films, (b) TiO_2-Ag NPs, (c) top surface of TiO_2, and (d) EDS spectra for the surface of TiO_2.

The TEM images clearly show that the the Ag NPs have been successfully deposited on the transparent TiO_2 thin films. Figure. 5.4(a) shows conventional TEM images of the NPs obtained by the nanosecond laser before deposition on the TiO_2 thin film.

Figure. 5.4(b) shows the size distribution of the Ag NPs, resulting in a mean size dispersion value of about 10 nm. In Figure. 5.4(c), we can observe in TEM-SE mode the morphology of the layer once it has been removed from the glass substrate, as well as the great homogeneity and continuity throughout it.

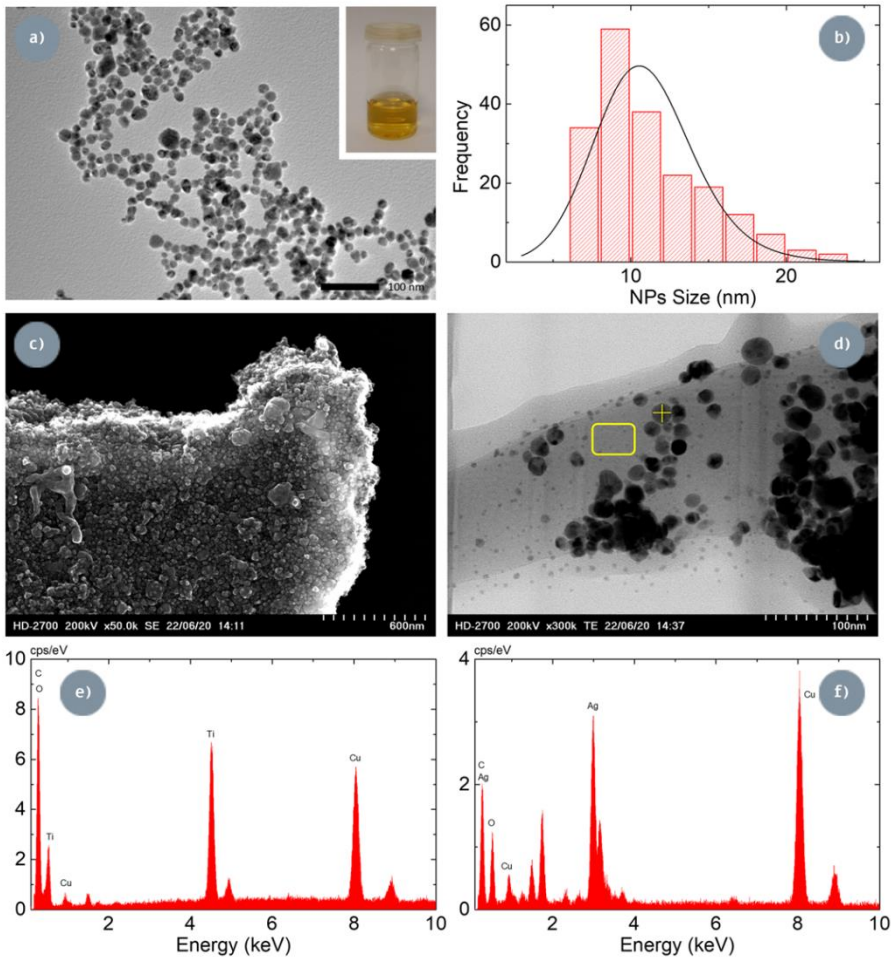

Figure 5.4 (a) Conventional TEM image of the Ag NPs before deposition,(b) size distribution of the Ag NPs (c) TEM-SE image of the transparent TiO_2-Ag NPs thin film, (d) Conventional TEM image of the transparent TiO_2-Ag NPs thin film and (e) EDS spectra of the surface of TiO_2 and (f) EDS spectra of the Ag NPs on the surface of TiO_2.

Figure. 5.4(d) shows the deposition of the Ag NPs on the TiO_2 thin film without affecting the macrophology of the NPs, which remain mainly spherical, and the agglomeration can also be observed once they adhere to the TiO_2 surface.

Figure. 5.4(f) show the corresponding EDS spectra for the areas where only Ag NPs are present and the area where only the TiO_2 layer is present. The Cu and C that appear in the spectrum come from the grids where the material to be analyzed has been deposited.

Raman spectroscopy was utilized to further study the structure of the transparent thin films. The Raman spectra of the samples confirmed anatase as the only TiO_2 phase present in the surfaces of the thin films'.

The normalized (over the most intense band at approx. 138 cm^{-1}) average spectra of the particular clusters are presented in Figure. 5.5.

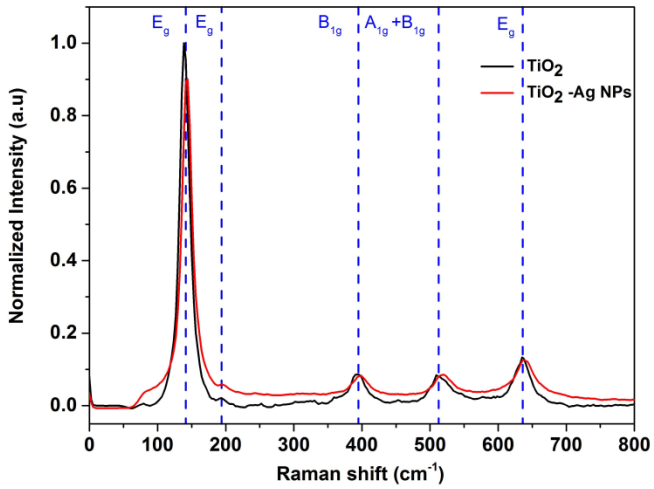

Fig. 5.5 Raman average spectra of the TiO_2 and TiO_2-Ag NPs transparent thin films.

While detailed assignments of the bands are shown in Table 5.1.

Table 5.1 Raman spectra of thin film TiO_2 and TiO_2-Ag NPs normalized to the most intense peak (144 cm^{-1}).

Band Mode	E_g	E_g	B_{1g}	$A_{1g} + B_{1g}$	E_g
		Raman shift (cm^{-1})			
TiO_2	138	190	393	509	635
TiO_2-Ag NPs	144	196	398	520	637
TiO_2 (Anatase) [34]	144	197	399	519	639

5.3.2 Optical spectral properties of TiO_2 and TiO_2- Ag NPs transparent thin films

The results of the optical properties of the transparent thin films were characterized using UV-Vis absorption spectroscopy. As shown in Figure. 5.6(a), the thin films have a high transmittance of up to 85% in the case of TiO_2 and 80% when loaded with Ag NPs.

The oscillations observed in the transmittance spectrum are due to interferences between the interface of the glass with the thin film and the thin film with the air [36].

Figure. 5.6(b) shows the absorption spectra for the transparent TiO_2 and TiO_2-Ag thin films with the maximum absorption occurring in the UV. Bandgap values for each film were also obtained,from the transmittance results (see Figure. 5(c)).

To do so, first, the absorption coefficient (α) values were calculated using Lambert's Law as the following equation (3) [37]:

$$A = \frac{1}{t} \ln\left(\frac{1}{T}\right) \quad (5.3)$$

where T is the transmittance, and t is the film thickness. An optical bandgap of thin films was estimated using equation (4) by the extrapolation of $(\alpha h\nu)^2$ vs. hν.

$$\alpha h\upsilon = A\left(h\upsilon - E_g\right)^{\frac{1}{2}} \quad (5.4)$$

where A is a constant, hν is the photon energy, and Eg is the optical bandgap.

The optical bandgap of transparent TiO_2 and TiO_2-Ag NPs thin films was determined by extrapolating the region of the plot to the energy axis where $\alpha^2 = 0$, and was found to have a value of 2.

The band gap value for the TiO_2 thin films was 3.758 eV, whereas for the TiO_2-Ag NPs it showed a small decrease with a band gap value of 3.708 eV.

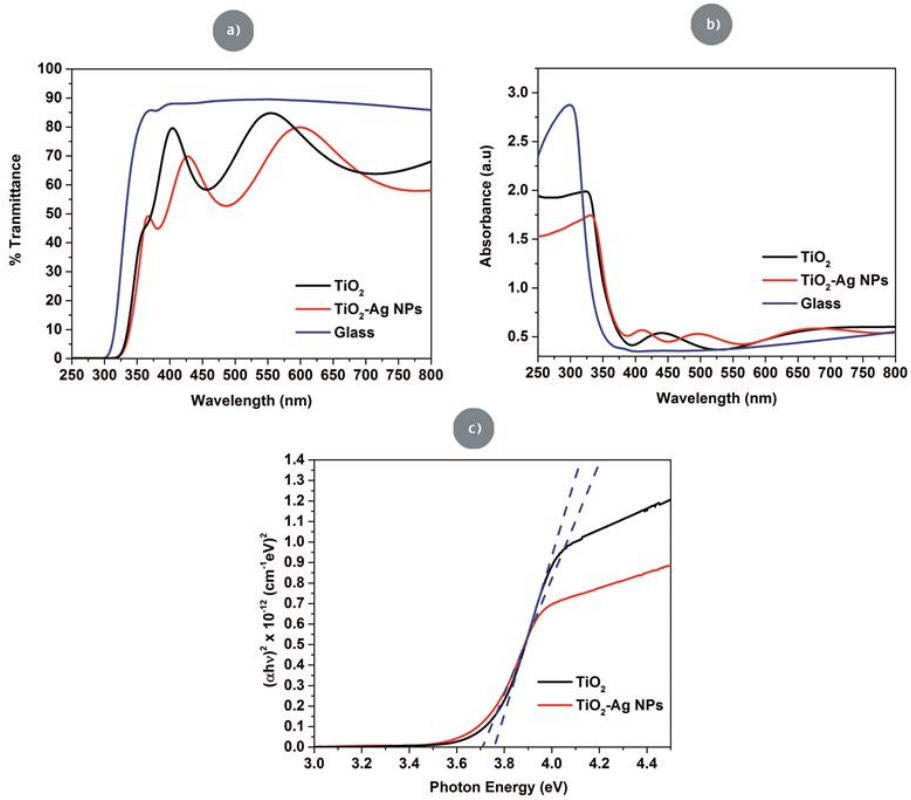

Figure 5.6 (a) The transmittance, (b) the absorbance and (c) the optical band gap of transparent TiO_2 and TiO_2-Ag NPs thin films.

This small variation was due to the fact that the NPs were on the surface of the TiO_2 thin film and not inserted/doped into the TiO_2 structure, where considerable changes in the band gap value should be expected [38]. Moreover, this variation may also be due to changes in grain size, a specific surface area or the microstructure of the thin films [39]. Thickness is also a variable but in this case both TiO_2 and TiO_2-Ag thin films had very similar thicknesses.

5.3.3 Applications of transparent TiO_2 and TiO_2- Ag NPs thin films

Compared to other transparent thin films, TiO_2-Ag NPs show very high optical properties. By taking advantage of other thin film layers, several applications including photocatalysis and antimicrobial surfaces were performed with TiO_2-Ag NPs.

5.3.4. Photocatalytic degradation of RhB

The photocatalytic activity of the thin films was assessed initially by monitoring the degradation of RhB solutions irradiated with UV light. A series of experiments were then conduced to evaluate the photocatalytic degradation of transparent TiO_2 and TiO_2-Ag NPs thin films. First, the photodegradation of RhB in the absence of the thin films was evaluated in two control assays: (i) under UV-light radiation, and (ii) under UV-light irradiation and the presence of a glass substrate.

The results showed that 16% and 15.6% of RhB were degraded after 330 minutes in the blank experiments (i) and (ii), respectively (Figure.S7). Moreover, the capacity of thin films to adsorb RhB molecules was also evaluated, using TiO_2 and TiO_2-Ag NPs thin films under dark conditions.

It was found that a very low amount of RhB was adsorbed on the surface of the thin films (about 14%) (Figure.S6), reaching the maximum plateau at 30 minutes.

The total weight was 0.9 mg for both TiO_2 and TiO_2-Ag NPs thin films. In addition, the amount of catalyst was much smaller than similar work published in the literature [40,41]. UV-Vis absorption spectra of RhB dye degradation using TiO_2 are shown in Figure.S8.

The thin films of TiO_2 degraded 85.3% in 210 minutes whereas TiO_2-Ag NPs thin films were able to degrade 99.4% in the same time as shown in Fig.7(a). Fig. 7(b) also clearly shows the difference in photodegradation efficiency by representing the C/C_0 for the transparent of TiO_2 and TiO_2-Ag NPs thin films, together the experimental points obtained and the mathematical fit to an exponential.

The calibration line used to obtain the concentration values is shown in Figure.S9. This difference in the photodegradation between TiO_2 thin films and TiO_2-Ag NPs is due to the fact that Ag NPs on the TiO_2 surface cause an equilibrium of the Fermi energy level that leads to the bending of the semiconductor's CB, thereby generating a Schottky junction.

This in turn promotes the transfer of photo-excited electrons from the CB of TiO_2 to Ag, thus preventing the recombination of electron-hole pairs (e^-/h^+) in the TiO_2 matrix. These electrons can be combined with oxygen to generate the superoxide radicals, which can further combine with holes to yield higher hydroxyl radicals (than when it occurs only on the TiO_2 surface) [42,43].

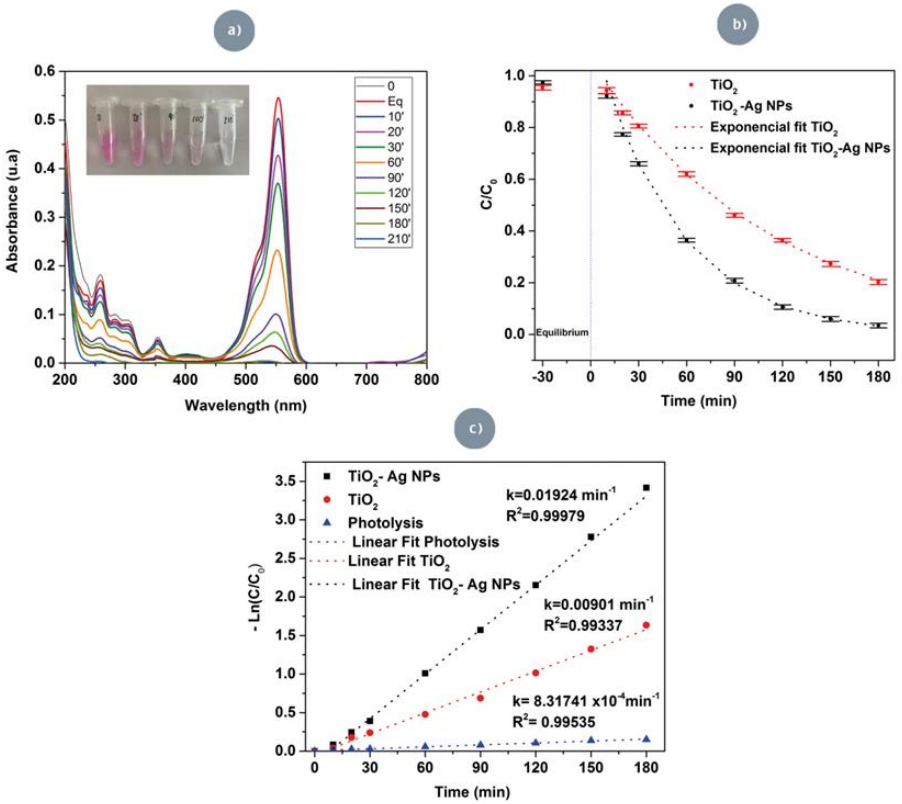

Figure 5.7 (a) UV-Vis absorption spectra of aqueous solutions of RhB (C_0=5 mg/L) under UV-light irradiation in the presence of TiO_2-Ag NPs thin films; (b) Photodegradation performance and (c) respective Curve of pseudo-first-order decay fitted linear regression, for RhB photodegradation in the presence of TiO_2-Ag NPs and TiO_2 thin films.

The kinetics of RhB decontamination was performed using the expression presented in equation (5.5):

$$k_{app} = \frac{-\ln\left(\frac{C}{C_0}\right)}{t} \qquad (5.5)$$

where k_{app} (min^{-1}) represents the reaction rate constant in min^{-1} at time t (min).

As can be seen in Figure. 5.7(c), when TiO_2 thin film is in contact with Ag NPs the kinetic costant is twice as high as when the reaction takes place with TiO_2 alone.

The value of the constant for the TiO_2 is 9.01×10^{-3} while the value for the TiO_2-Ag NPs thin films is 19.14×10^{-3} min^{-1}.This kinetic constant value is much higher than the costant values obtained for the degradation of differents dye concentrations by different compounds also in thin films as shown in Table 5.2 [33-36].

Table 5.2 Comparison of the transparent TiO_2-Ag NPs thin films with other recent similar photocatalytic thin films under UV light

Samples	Dye concentration (mg/L)	Removal	Kapp (10^{-3} min^{-1})
This work	5.0 RhB	99.7% after 3.5h	19.1
Cu doped-ZnO [43]	3.2 Metylene Blue (MB)	74.0 % after 2h	5.6
TiO_2 [44]	10.0 MB	53.06% after 2h	4.1
$0.05Fe_2O_3/TiO_2$ [45]	4.79 RhB	60% afte 5h	-
Ag loaded TiO_2-ZnO [46]	10.0 MB	70% after 2 h	9.92

As shown in Figure. 5.8(a), after adding tert-butyl alcohol to the reaction solution, the photocatalytic degradation rate of the RhB solution decreased from 99.70% to 55.8%.,while adding FA or 1,4-BQ only decreased the degradation rate to 82.45% and 71.77% respectively.

Figure. 5.8(b) shows a bar graph representing the photocatalytic degradation using each of the radical scavengers. Figure. 5.8(a) and 5.8(b) indicate that the holes (h+) make a limited contribution to RhB removal and also reveal that $O^{2-\bullet}$ played an insignificant role through the degradation process, thus confirming that OH• played a crucial role in the process. The schematic representation of the photo-generated charge transfer process in transparent TiO_2-Ag NPs thin films under UV is illustrated in Figure. 8(c) and Eqs. (5.6)–(5.14) [48–50].

$$TiO_2 + hv_{UV} \rightarrow TiO_2 + (e^- + h^+) \quad (5.6)$$

$$h_{UV} + H_2O \rightarrow H^+ + OH^- \quad (5.7)$$

$$e^-_{CB} + O_2 \rightarrow O_2^- \quad (5.8)$$

$$O_2^- + H^+ \rightarrow HO_2 \quad (5.9)$$

$$HO_2 + e^-_{CB} \rightarrow H_2O_2 \quad (5.10)$$

$$H_2O_2 + e^-_{CB} \rightarrow OH^- + OH\bullet \quad (5.11)$$

$$OH^- + hv_{UV} \rightarrow OH\bullet \quad (5.12)$$

$$Ag + e^-_{CB-TiO_2} \rightarrow Ag + e^-_{CB} \quad (5.13)$$

$$O_2 + H_2O + e^-_{CB} \rightarrow OH\bullet \quad (5.14)$$

This mechanism explains how**,** under UV irradiation, hole-electron pairs are photogenerated in TiO_2 thin film. The CB level of TiO_2 is higher than the Fermi energy level of Ag NPs, so the photoexcited electrons from TiO_2 are transferred to the Ag NPs, acting as electron scavengers for TiO_2 [197].

In this way**,** the recombination of electrons and photoinduced holes is reduced and the lifetime is prolonged. This explains the results obtained, the photodegradation of RhB is much faster as the hydroxyl radical species have a longer lifetime due to the Ag NPs, thus achieving a faster photodegradation of the dye.

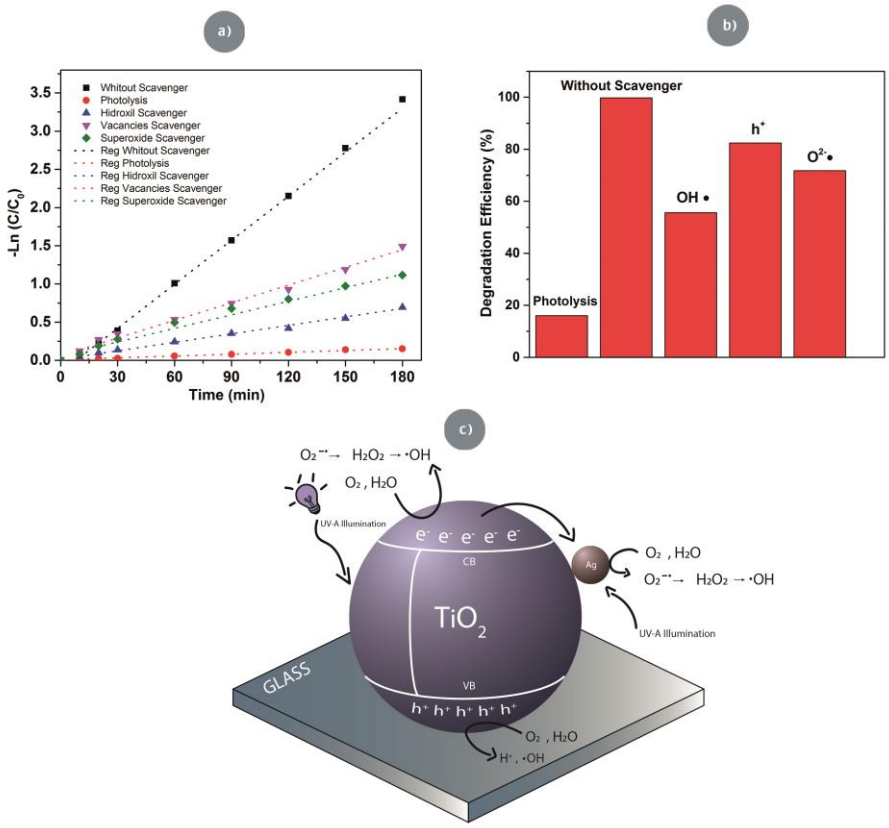

Figure 5.8 Reaction kinetics of the photoreaction with various scavengers on TiO_2-Ag NPs; (b) Degradation Efficiency (%) with various scavengers on TiO_2-Ag NPs ;(c) The degradation mechanism of transparent TiO_2-Ag NPs thin films.

In order to study the durability and reusability of these thin films as photocatalysts, they were subjected to cyclic tests, that were run four times. Figure. 5.9(a) shows the photocatalytic degeneration of RhB on these thin films after four cycles. After four cycles the TiO_2-Ag NPs photocatalyst had only lost an efficiency from 99.77% to 87.16% as can be seen in the bar chart in Figure. 5.9(b).

This decrease in efficiency is due to the fact that RhB is adsorbed after cycling on the active centers of the photocatalyst causing a slight decrease in degradation efficiency as can be seen in the FTIR spectra (Figure.S.10) where after four cycles we can see the characteristic bands of RhB (3385 cm^{-1}, 2922 cm^{-1}, 2850 cm^{-1} and 1635 cm^{-1}) on the photocatalyst.

For the stability study of the photocatalyst, the possible presence of Ag and Ti was also measured during the photocatalysis tests in the RhB solution using an internal method based on ISO 11885.

The results obtained for 0, 210 and 300 minutes show that the amount of Ag and Ti was always below the detection limit of the technique (Table S.3), thus confirming that there was no leaching of metals into the RhB solution.

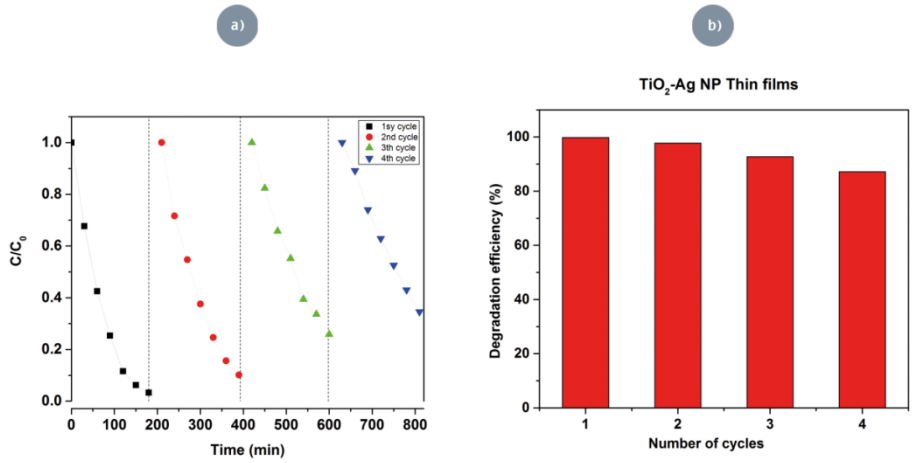

Figure 5.9. Reusability of the transparent TiO_2-Ag NPs thin films in the photocatalytic degradation of RhB under UV light irradiation after four cycles, and (b) bar graph of the percentage of degradation efficiency over four cycles.

5.3.5 *Antibacterial activity of transparent TiO_2-Ag NPs thin films.*

The antibacterial activity of transparent TiO_2-Ag NPs thin films was determined in accordance with standard tests JISZ 2801_2000 after exposure to UV light for 4 hours. Glass, TiO_2 and TiO_2-Ag NPs samples were used as a reference and suspended Gram-negative *E. coli* ATCC 25922 cells were placed on each sample. After counting viable cells recovered from the surface of the materials, antibacterial rates were calculated.

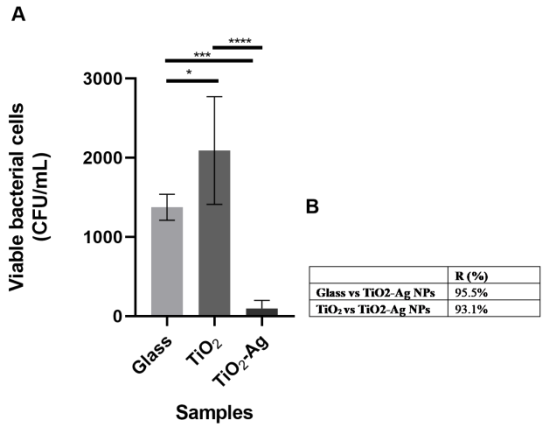

Figure 5.10 Antibacterial assay of transparent TiO_2-Ag NPs thin films (a) Results of colony forming units/mL (CFU/mL) in each sample tested. Significance (*) of the results was verified using one-way ANOVA then Sidak's multiple comparisons test was used to determine statistical significance. (b) Antibacterial rates (%) obtained for TiO_2-Ag NPs

Results are presented in Figure. 5.10 and clearly show a strong antibacterial action of TiO_2-Ag NPs, when compared with glass and with TiO_2 samples,with values of 95.5% and 93.1%, respectively. Results are significantly different are marked with (*) in Figure. 10.

The differences observed for both controls, glass and TiO_2 samples, are probably due to slightly different material performances in the complete recovery of treated bacterial cells form the surface of materials. These differences do not preclude the strong antibacterial action observed.

5.4. Conclusion

Pure and TiO_2-Ag NPs transparent thin films with Ag NPs synthesized by nanosecond laser, with excellent photocatalytic activities being obtained for the degradation of RhB using UV light for a very small amount of catalyst, maintaining a very high degree of glass transparency of more than 80%.

Thanks to the Ag NPs, it was observed that the production of radicals (OH•) increased ,as did the lifetime, which made the degradation of the dye much faster and up to 99.7% of the dye could be degraded in 210 min. The removal efficiency for RhB reached 99.7%, which was twice than that of pure TiO_2.

Furthermore, the reuse of the catalyst for four cycles was also studied, observing that the degradation efficiency decreased by 10%. These results are very interesting due to the fact that the catalyst is synthesized on glass by using methodologies, that are widely applicable in industry the result being a catalyst with a high degradation efficiency for pollutants and dyes such as RhB.

Also, the films that were developed, after addition of Ag NPs to the surface, showed strong antibacterial activities, as measured using a gram-negative bacterium as reference strain. The reduction in the number of bacteria reached 93% after irradiation under UV-light for 4 hours.

Further research could measure the antimicrobial power of these transparent thin films by the addition of Ag NPs to the surface as well as the photocatalytic action of the films using different types of light (visible light or sunlight).

Additionally, the combination of these two techniques would allow an the easy synthesis of a multitude of compounds that can be functionalized with metal NPs.

5.5. References

[1] C. Doroody, K.S. Rahman, T.S. Kiong, N. Amin, Optoelectrical impact of alternative window layer composition in CdTe thin film solar cells performance, Sol. Energy. 233 (2022) 523–530. https://doi.org/10.1016/j.solener.2022.01.049.

[2] S. Tyagi, A. Kumar, A. Kumar, Y.K. Gautam, V. Kumar, Y. Kumar, B.P. Singh, Enhancement in the sensitivity and selectivity of Cu functionalized MoS_2 nanoworm thin films for nitrogen dioxide gas sensor, Mater. Res. Bull. 150 (2022) 111784. https://doi.org/10.1016/j.materresbull.2022.111784.

[3] P. Ni, B. Chen, X. Wei, Effects of annealing temperatures on energy storage performance of sol-gel derived ($Ba_{0.95}$, $Sr_{0.05}$) ($Zr_{0.2}$, $Ti_{0.8}$) O_3 thin films, Ceram. Int. (2022). https://doi.org/10.1016/j.ceramint.2022.03.167.

[4] S.A. Khalate, S.A. Kadam, Y.R. Ma, S.B. Kulkarni, V.G. Parale, U.M. Patil, Binder free cobalt iron phosphate thin films as efficient electrocatalysts for overall water splitting, J. Colloid Interface Sci. 613 (2022) 720–732. https://doi.org/10.1016/j.jcis.2022.01.015.

[5] N. Kalangadan, A.S. Mary, R.H. Jyothi, S. Punniyakoti, S. Sundaresan, R.K. Alagarsamy, K. Rajaram, Characterization and antimicrobial evaluation of green synthesized silver nanoparticle thin films with reusable applications, Mater. Lett. 314 (2022) 131923. https://doi.org/10.1016/j.matlet.2022.131923.

[6] S. Chen, T. Liang, N. Wen, F.H. Liu, C.C. Tsao, C.Y. Hsu, Electro-less plating nickel-phosphorus of low carbon steel using various pretreatments and an external magnetic field, J. Saudi Chem. Soc. 24 (2020) 704–714. https://doi.org/10.1016/j.jscs.2020.07.008.

[7] A.C. Alves, F. Wenger, P. Ponthiaux, J.P. Celis, A.M. Pinto, L.A. Rocha, J.C.S. Fernandes, Corrosion mechanisms in titanium oxide-based films produced by anodic treatment, Electrochim. Acta. 234 (2017) 16–27. https://doi.org/10.1016/j.electacta.2017.03.011.

[8] S.I. Dorovskikh, D.D. Klyamer, A.M. Makarenko, K. V. Zherikova, A.E. Turgambaeva, Y. V. Shevtsov, D.B. Kal'nyi, I.K. Igumenov, N.B. Morozova, The comprehensive study of thermal properties of tris(2,2,6,6-tetramethyl-3,5-heptanedionato)cobalt(III) related to the chemical vapor deposition of Co-oxide based thin film materials, Vacuum. 199 (2022) 110969. https://doi.org/10.1016/j.vacuum.2022.110969.

[9] N.R. Aswathy, J.J. Varghese, S.R. Nair, R.V. Kumar, Structural, optical, and magnetic properties of Mn-doped NiO thin films prepared by sol-gel spin coating, Mater. Chem. Phys. 282 (2022) 125916. https://doi.org/10.1016/j.matchemphys.2022.125916.

[10] K. Vijayan, S.P. Vijayachamundeeswari, K. Sivaperuman, N. Ahsan, T. Logu, Y. Okada, A review on advancements, challenges, and prospective of copper and non-copper based thin-film solar cells using facile spray pyrolysis technique, Sol. Energy. 234 (2022) 81–102. https://doi.org/10.1016/j.solener.2022.01.070.

[11] S.A. Tepe, M. Danışman, N. Cansever, Crystallization of TiO_2 on sputter deposited amorphous titanium thin films, Mater. Chem. Phys. 282 (2022). https://doi.org/10.1016/j.matchemphys.2022.125965.

[12] C. Zhang, T. Uchikoshi, T. Ishigaki, Effect of crystalline orientation on photocatalytic performance for Nb-doped TiO_2 nanoparticles, Adv. Powder Technol. 32 (2021) 4149–4154. https://doi.org/10.1016/j.apt.2021.09.019.

[13] R.S. Santiago, L.C.D. Silva, F.D. Origo, C. Stegemann, I.L. Graff, R.G. Delatorre, D.A. Duarte, Target power influence on optical and electrical properties of amorphous titanium oxide deposited by reactive grid-assisted magnetron sputtering, Thin Solid Films. 700 (2020). https://doi.org/10.1016/j.tsf.2020.137917.

[14] S. Na-Phattalung, D.J. Harding, P. Pattanasattayavong, H. Kim, J. Lee, D.W. Hwang, T.D. Chung, J. Yu, Band gap narrowing of TiO_2 nanoparticles: A passivated Co-doping approach for enhanced photocatalytic activity, J. Phys. Chem. Solids. 162 (2022) 110503. https://doi.org/10.1016/j.jpcs.2021.110503.

[15] M. Balamurugan, M. Silambarasan, S. Saravanan, T. Soga, Synthesis of anatase and rutile mixed phase titanium dioxide nanoparticles using simple solution combustion method, Phys. B Condens. Matter. 638 (2022) 413843. https://doi.org/10.1016/j.physb.2022.413843.

[16] A.H. Shah, M.A. Rather, Effect of calcination temperature on the crystallite size, particle size and zeta potential of TiO_2 nanoparticles synthesized via polyol-mediated method, Mater. Today Proc. 44 (2021) 482–488. https://doi.org/10.1016/j.matpr.2020.10.199.

[17] H. Peng, S. Xie, P. Niu, Z. Zhang, T. Yuan, Z. Ren, X. Wang, Y. Zhao, R. Li, Jornal Proof, J. Alloys Compd. (2020) 158286. https://doi.org/10.1016/j.ijleo.2022.169231.

[18] C. Pragathiswaran, C. Smitha, B.M. Abbubakkar, P. Govindhan, N.A. Krishnan, Synthesis and characterization of TiO_2/ZnO-Ag nanocomposite for photocatalytic degradation of dyes and anti-microbial activity, Mater. Today Proc. 45 (2021) 3357–3364. https://doi.org/10.1016/j.matpr.2020.12.664.

[19] T. Liu, L. Wang, X. Lu, J. Fan, X. Cai, B. Gao, R. Miao, J. Wang, Y. Lv, Comparative study of the photocatalytic performance for the degradation of different dyes by $ZnIn_2S_4$: adsorption, active species, and pathways, RSC Adv 7 (2017) 12292–12300. https://doi.org/10.1039/c7ra00199a

[20] J.T. Schneider, D.S. Firak, R.R. Ribeiro, P. Peralta-Zamora, Use of scavenger agents in heterogeneous photocatalysis: truths, half-truths, and misinterpretations, Phys. Chem. Chem. Phys. 22 (2020) 15723–15733. https://doi.org/10.1039/d0cp02411b.

[21] Y. Hou, A. Mushtaq, Z. Tang, E. Dempsey, Y. Wu, Y. Lu, C. Tian, J. Farheen, X. Kong, M.Z. Iqbal, ROS-responsive Ag-TiO_2 hybrid nanorods for enhanced photodynamic therapy of breast cancer and antimicrobial applications, J. Sci. Adv. Mater. Devices. 7 (2022) 100417. https://doi.org/10.1016/j.jsamd.2022.100417.

[22] S. Barcikowski, V. Amendola, G. Marzun, C. Rehbock, S. Reichenberger, D. Zhang, B. Gökce, Handbook of Laser Synthesis of Colloids, 2016. https://doi.org/10.17185/duepublico/41087.

[23] R.C. Forsythe, C.P. Cox, M.K. Wilsey, A.M. Müller, Pulsed Laser in Liquids Made Nanomaterials for Catalysis, Chem. Rev. 121 (2021) 7568–7637. https://doi.org/10.1021/acs.chemrev.0c01069.

[24] D. Zhang, B. Gökce, S. Barcikowski, Laser Synthesis and Processing of Colloids: Fundamentals and Applications, Chem. Rev. 117 (2017) 3990–4103. https://doi.org/10.1021/acs.chemrev.6b00468.

[25] V. Amendola, D. Amans, Y. Ishikawa, N. Koshizaki, G. Compagnini, S. Reichenberger, S. Barcikowski, Room-Temperature Laser Synthesis in Liquid of Oxide , Metal-Oxide Core-Shells , and Doped Oxide Nanoparticles, (n.d.). https://doi.org/10.1002/chem.202000686.

[26] R. Streubel, S. Barcikowski, B. Gökce, Continuous multigram nanoparticle synthesis by high-power, high-repetition-rate ultrafast laser ablation in liquids, Opt. Lett. 41 (2016) 1486. https://doi.org/10.1364/ol.41.001486.

[27] C. Don, R. Torres-mendieta, A. Pyatenko, E. Falomir, M. Ferna, M. Gladys, Fabrication by Laser Irradiation in a Continuous Flow Jet of Carbon Quantum Dots for Fluorescence Imaging, (2018). https://doi.org/10.1021/acsomega.7b02082.

[28] C. Doñate-buendía, M. Fernández-alonso, J. Lancis, G. Mínguez-vega, Overcoming the barrier of nanoparticle production by femtosecond laser ablation in liquids using simultaneous spatial and temporal focusing, Photonics Res. 7 (2019) 1249. https://doi.org/10.1364/PRJ.7.001249.

[29] M. Sikder, J.R. Lead, G.T. Chandler, M. Baalousha, Science of the Total Environment A rapid approach for measuring silver nanoparticle concentration and dissolution in seawater by UV –Vis, Sci. Total Environ. 618 (2018) 597–607. https://doi.org/10.1016/j.scitotenv.2017.04.055.

[30] C.V. Restrepo, C.C. Villa, Synthesis of silver nanoparticles, influence of capping agents, and dependence on size and shape: A review, Environ. Nanotechnology, Monit. Manag. 15 (2021). https://doi.org/10.1016/j.enmm.2021.100428.

[31] A.S. AlShammari, M.M. Halim, F.K. Yam, N.H.M. Kaus, Synthesis of Titanium Dioxide (TiO_2)/Reduced Graphene Oxide (rGO) thin film composite by spray pyrolysis technique and its physical properties, Mater. Sci. Semicond. Process. 116 (2020) 105140. https://doi.org/10.1016/j.mssp.2020.105140.

[32] Xi Zhang, Mohammadreza Kamali, Timon Uleners, Jasper Symus, Siyu Zhang, Ze Liu, Maria Elisabete V. Costa, Lise Appels, Deirdre Cabooter, Raf Dewil,UV/TiO_2/periodate system for the degradation of organic pollutants – Kinetics, mechanisms and toxicity study,Chemical Engineering Journal, 449, (2022),13768. https://doi.org/10.1016/j.cej.2022.137680.

[33] N. Fleitas-Salazar, E. Silva-Campa, S. Pedroso-Santana, J. Tanori, M.R. Pedroza-Montero, R. Riera, Effect of temperature on the synthesis of silver nanoparticles with polyethylene glycol: new insights into the reduction mechanism, J. Nanoparticle Res. 19 (2017). https://doi.org/10.1007/s11051-017-3780-3.

[34] R. Lu, J. Sha, W. Xia, Y. Fang, L. Gu, Y. Wang, A 3D-SERS substrate with high stability: Silicon nanowire arrays decorated by silver nanoparticles, CrystEngComm. 15 (2013) 6207. https://doi.org/10.1039/c3ce40788h.

[35] Lubas M, Jasinski JJ, Sitarz M, Kurpaska L, Podsiad P, Jasinski J. Raman spectroscopy of TiO_2 thin films formed by hybrid treatment for biomedical applications. Spectrochim Acta A Mol Biomol Spectrosc. 2014 Dec 10;133:867-71. https://doi.org/10.1016/j.saa.2014.05.045.

[36] D. Komaraiah, E. Radha, J. Sivakumar, M.V. Ramana Reddy, R. Sayanna, Structural, optical properties and photocatalytic activity of Fe^{3+} doped TiO_2 thin films deposited by sol-gel spin coating, Surfaces and Interfaces. 17 (2019) 100368. https://doi.org/10.1016/j.surfin.2019.100368.

[37] T. Ratana, P. Amornpitoksuk, T. Ratana, S. Suwanboon, The wide band gap of highly oriented nanocrystalline Al doped ZnO thin films from sol-gel dip coating,J.Alloys Compd. 470 (2009) 408–412. https://doi.org/10.1016/j.jallcom.2008.02.081.

[38] D. Komaraiah, E. Radha, J. Sivakumar, M. V. Ramana Reddy, R. Sayanna, Photoluminescence and photocatalytic activity of spin coated Ag^{+} doped anatase TiO_2 thin films, Opt. Mater. (Amst). 108 (2020) 110401. https://doi.org/10.1016/j.optmat.2020.110401.

[39] S. Ahadi, N.S. Moalej, S. Sheibani, Characteristics and photocatalytic
behavior of Fe and Cu doped TiO_2 prepared by combined sol-gel and mechanical alloying, Solid State Sci. 96 (2019) 105975. https://doi.org/10.1016/j.solidstatesciences.2019.105975.

[40] B. Xing, C. Shi, C. Zhang, G. Yi, L. Chen, H. Guo, G. Huang, J. Cao, Preparation of TiO_2/Activated Carbon Composites for Photocatalytic Degradation of RhB under UV Light Irradiation, J. Nanomater. 2016 (2016). https://doi.org/10.1155/2016/8393648.

[41] T. Wang, T. Tang, Y. Gao, Q. Chen, Z. Zhang, H. Bian, Hydrothermal preparation of Ag-TiO_2-reduced graphene oxide ternary microspheres structure composite for enhancing photocatalytic activity, Phys. E Low-Dimensional Syst. Nanostructures.112(2019) 128–136. https://doi.org/10.1016/j.physe.2018.10.033.

[42] D.S. Liu, J. Wu, Y. Wang, H. Ji, L. Gao, X. Tong, M. Usman, P. Yu, Z. Wang, Tailored performance of layered transition metal dichalcogenides via integration with low dimensional nanostructures, RSC Adv. 7 (2017) 11987–11997. https://doi.org/10.1039/c7ra01363a.

[43] F. Mo, Q. Zhou, Y. He, Nano–Ag: Environmental applications and perspectives, Sci. Total Environ. 829 (2022) 154644. https://doi.org/10.1016/j.scitotenv.2022.154644.

[44] F.Z. Nouasria, D. Selloum, A. Henni, S. Tingry, J. Hrbac, Improvement of the photocatalytic performance of ZnO thin films in the UV and sunlight range by Cu doping and additional coupling with Cu_2O, Ceram. Int. 48 (2022) 13283–13294. https://doi.org/10.1016/j.ceramint.2022.01.207.

[45] A. Kumar, V.K. Saxena, R. Thangavel, B. Kumar, A dual effect of surface roughness and photocatalysis of crystalline TiO_2 - thin film for self-cleaning application on a photovoltaic covering glass, Mater. Chem. Phys. 289 (2022) 126427. https://doi.org/10.1016/j.matchemphys.2022.126427.

[46] S. Wannapop, A. Somdee, T. Bovornratanaraks, Experimental study of thin film Fe_2O_3/TiO_2 for photocatalytic Rhodamine B degradation, Inorg. Chem. Commun. 128 (2021) 108585. https://doi.org/10.1016/j.inoche.2021.108585.

[47] M. Pérez-González, S.A. Tomás, J. Santoyo-Salazar, S. Gallardo-Hernández, M.M. Tellez-Cruz, O. Solorza-Feria, Sol-gel synthesis of Ag-loaded TiO_2-ZnO thin films with enhanced photocatalytic activity, J. Alloys Compd. 779 (2019) 908–917. https://doi.org/10.1016/j.jallcom.2018.11.302.

[48] H. Liu, Y. Hu, Z. Zhang, X. Liu, H. Jia, B. Xu, Synthesis of spherical Ag/ZnO heterostructural composites with excellent photocatalytic activity under visible light and UV irradiation, Appl. Surf. Sci. 355 (2015) 644–652. https://doi.org/10.1016/j.apsusc.2015.07.012.

[49] J. Zhang, J.K. Cha, G. Fu, E.J. Cho, H.S. Kim, S.H. Kim, Aerosol processing of Ag/TiO_2 composite nanoparticles for enhanced photocatalytic water treatment under UV and visible light irradiation, Ceram. Int. 48 (2022) 9434–9441. https://doi.org/10.1016/j.ceramint.2021.12.140.

[50] C. Chen, W. Ma, J. Zhao, Semiconductor-mediated photodegradation of pollutants under visible-light irradiation, Chem. Soc. Rev. 39 (2010) 4206–4219. https://doi.org/10.1039/b921692h.

CHAPTER 6

General conclusions

"The next industrial revolution is focusing on the ability to control matter at the nanoscale."

Chad A. Mirkin

1. General Conclusions

This PhD thesis emphasises the potential multifunctionality of oxide semiconductors, specifically ZnO and TiO_2, and their significance in several scientific disciplines, particularly in the realm of solid state chemistry and photocatalysis. Nevertheless, via the utilisation of various methodology, it has been established that the most effective strategy for achieving functionalization of glass surfaces is the application of high temperature deposition methods, specifically spray pyrolysis, onto the glass substrate.

Therefore, it is possible to draw the subsequent general conclusions:

- Transparent thin films of titanium dioxide (TiO_2) and zinc oxide (ZnO) were successfully synthesised using the spray pyrolysis process, while maintaining the optical properties of the glass substrate.

- The thin films that have been synthesised exhibit exceptional transparency, as seen by both TiO_2 and ZnO displaying a transmittance over 80%.

- The efficacy of the spray pyrolysis approach in producing transparent thin films has been well-established, making it a highly suitable method for application in both the ceramic and glass industries.

- The synthesised thin films have demonstrated their potential for multifunctionality in the field of photocatalysis, specifically in the degradation of pollutants and bacteria. A key requirement in these applications is the ability to generate reactive oxygen species (ROS) through light-induced processes, enabling the degradation of both organic molecules and pathogenic organisms.

- Extensive research has been conducted to investigate the processes involved in the production of reactive oxygen species (ROS) by the irradiation of semiconductors in solution. Additionally, the degradation of several modern contaminants, including organic dyes and chemicals utilised in pharmaceutical manufacture, has been examined.

- It has been observed that the incorporation of silver nanoparticles into transparent TiO_2 layers increases the generation of reactive oxygen species (ROS) during the ROS production mechanism. Consequently, this enhancement leads to an increase in the photocatalytic degradative efficiency of TiO_2 and ZnO thin films.

- It has been shown that the irradiation of thin films leads to the creation of reactive oxygen species (ROS), which in turn induces deterioration in several bacterial species. Notably, the ROS generated through this process have been found to inflict substantial harm on bacteria associated with faecal contamination, including Escherichia coli (*E. coli*).

In summary, the findings presented in this doctoral thesis illustrate the versatile nature of transparent thin films composed of TiO_2 and ZnO. These films exhibit a variety of highly favourable characteristics, rendering them potentially valuable in various domains. Specifically, they show promise in the realm of photocatalysis for pollutant degradation, as well as in the realm of safeguarding environments requiring bacterial sterility. Consequently, glass can be regarded not only as a transparent material, but also as a material with considerable practical applications.

In future research, as an extension of the present doctoral thesis, the aim is to synthesise transparent semiconducting oxides with a reduced band gap compared to ZnO and TiO_2. This goal can be achieved by employing the optimised synthesis technique of these transparent semiconducting oxides using spray pyrolysis on a glass substrate. Specifically, the oxides of interest for this study include copper (I) oxide (Cu_2O), copper (II) oxide (CuO), tungsten trioxide (WO_3), bismuth vanadate ($BiVO_4$) and iron (III) oxide (Fe_2O_3), all of which will be deposited as thin transparent layers.

In this particular scenario, the aim is to explore the potential of photocatalytic reactions in the degradation of gas pollutants. It is important to note that this thesis does not specifically investigate this aspect, but rather emphasises its significance due to its wide range of applications, including air and water cleaning.

Photocatalytic reactions have the ability to facilitate the decomposition of volatile organic compounds (VOCs) and nitrogen oxides (NO_x). Certain types of photocatalysts have the capability to generate hydrogen (H_2) by utilising visible light and either water vapour or liquid water. Additionally, these photocatalysts can facilitate the conversion of carbon dioxide (CO_2) into valuable hydrocarbons or other chemicals through the utilisation of renewable energy sources.

Annexes

"We are transforming the way we interact with the world through the new materials we create, opening the door to manufacturing more efficient and sustainable devices."

George M. Whitesides

Appendix I: Supplementary figures

Advances in Transparent Materials: ZnO Thin films for Photocatalytic and Antibacterial Applications

J.G. Cuadra[1], Ana C. Estrada[2], C. Oliveira[3], L.A. Abderrahim[1], S. Porcar[1], D. Fraga[1], T. Trindade[2], P. Seabra[4], J. Labrincha[4], J.B. Carda[1]

[1] Department of Inorganic and Organic Chemistry, University Jaume I, Avda. Sos Baynat s/n, Castellon, 12071, Spain

[2] Department of Chemistry, CICECO-Aveiro Institute of Materials, University of Aveiro, 3810-193 Aveiro, Portugal

[3]Department of Biology, CESAM, University of Aveiro, Campus Universitário de Santiago,3810-193, Aveiro, Portugal

[4]Materials and Ceramic Engineering Department, CICECO, University of Aveiro, Campus Universitário de Santiago, 3810-193 Aveiro, Portugal

[1] These authors contributed equally

* Corresponding authors Jaime González Cuadra

Department of Inorganic and Organic Chemistry, University Jaume I, Avda. Sos Baynat s/n, Castellon, 12071, Spain

Phone: + 964-728-234, E-mail: jcuadra@uji.es

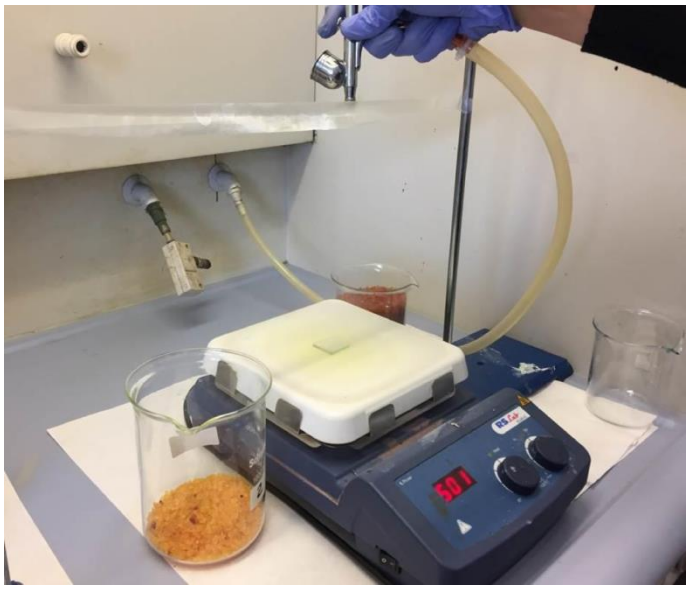

Fig. S1. Experimental setup for the preparation of ZnO thin films by spray pyrolysis on glass

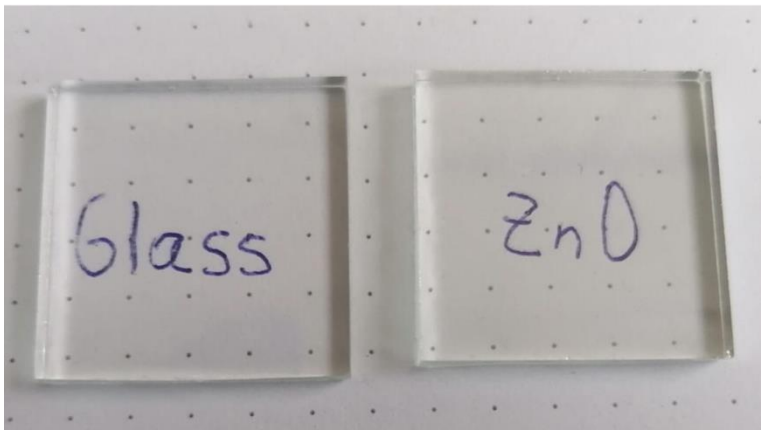

Fig. S2 Image of a ZnO transparent thin film on a glass substrate; the latter is also shown for comparison.

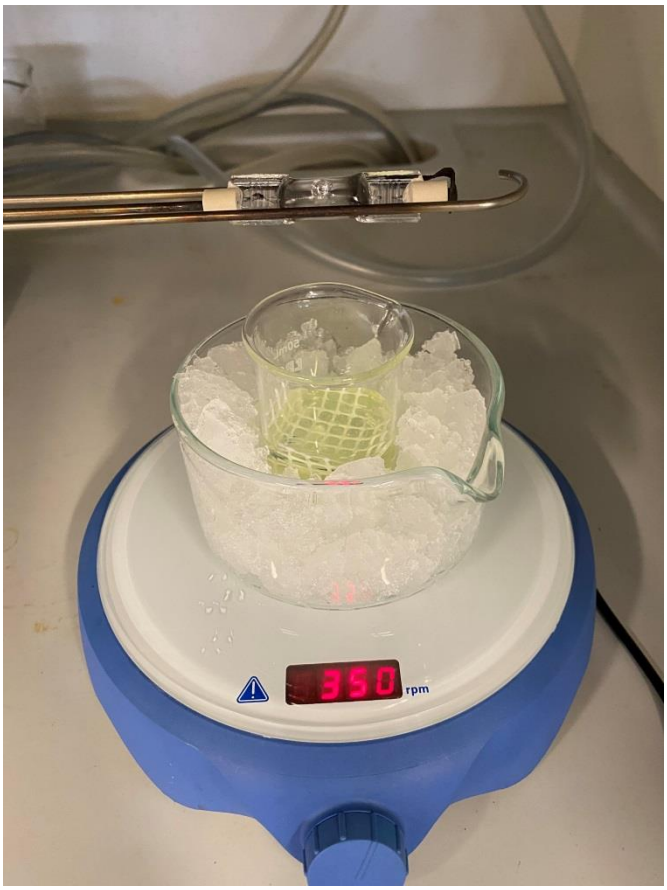

Fig. S3 Photocatalysis testing set up system

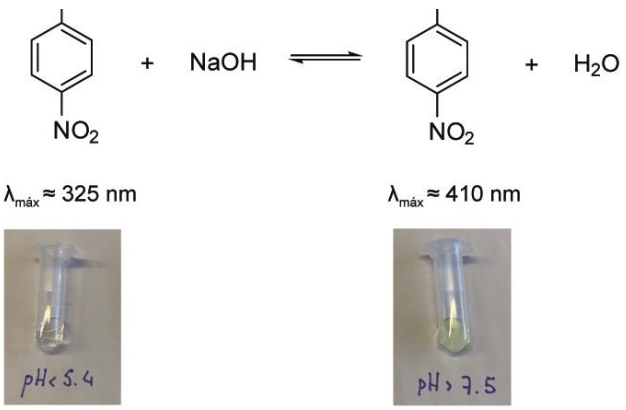

Fig. S4 Enolate formation reaction of 4-nitrophenol in basic medium

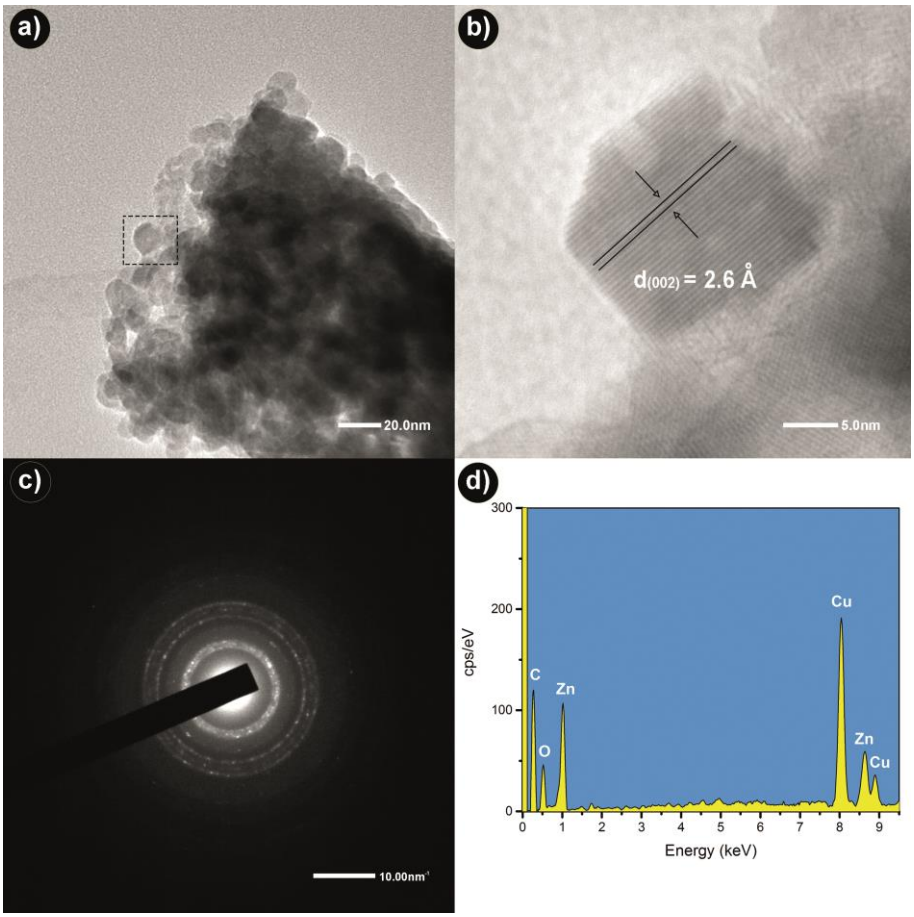

Fig. S5 (a) TEM image of the transparent ZnO thin film (b) High resolution TEM image of the marked area in (c) SAED pattern of the transparent ZnO thin film (d) EDS spectra of the transparent ZnO thin films.

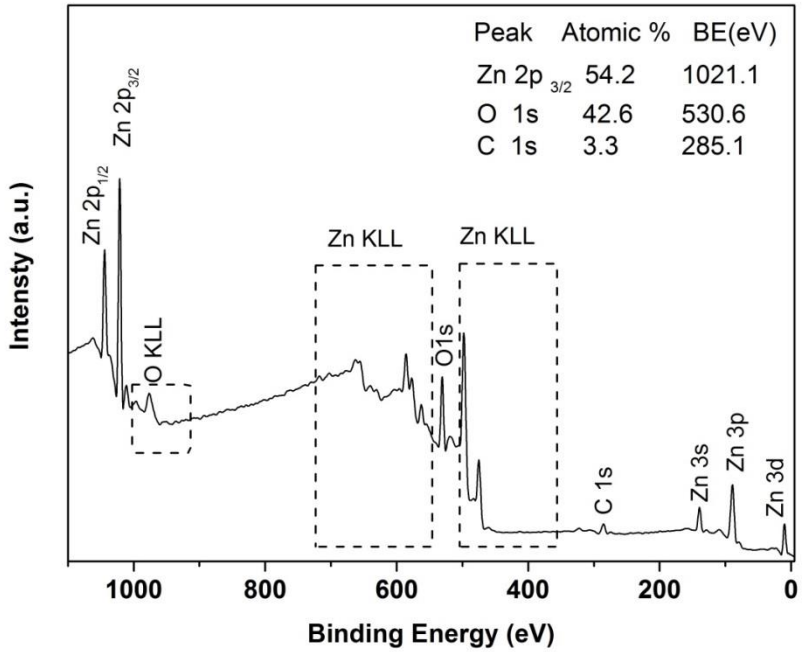

Fig. S6 XPS spectrum of transparent ZnO thin film.

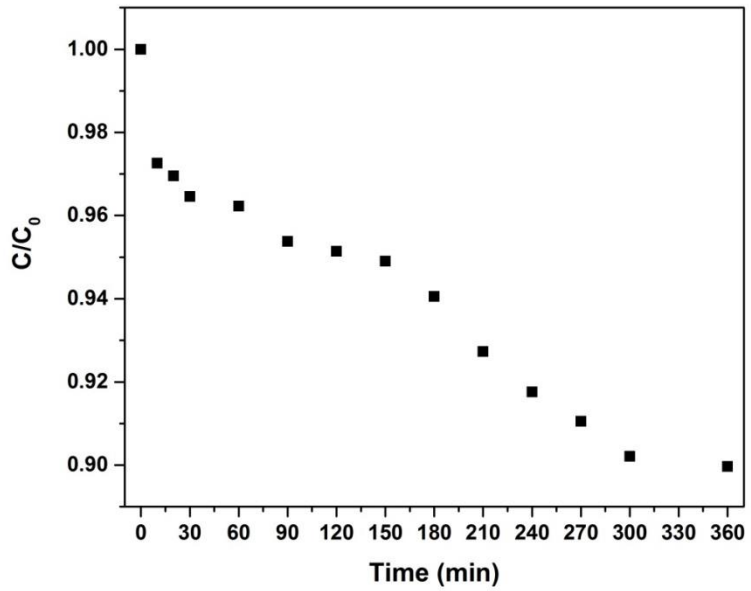

Fig. S7. Results of experiments for the photodegradation of 4-Nitrophenmol (4-NP) under UV irradiation.

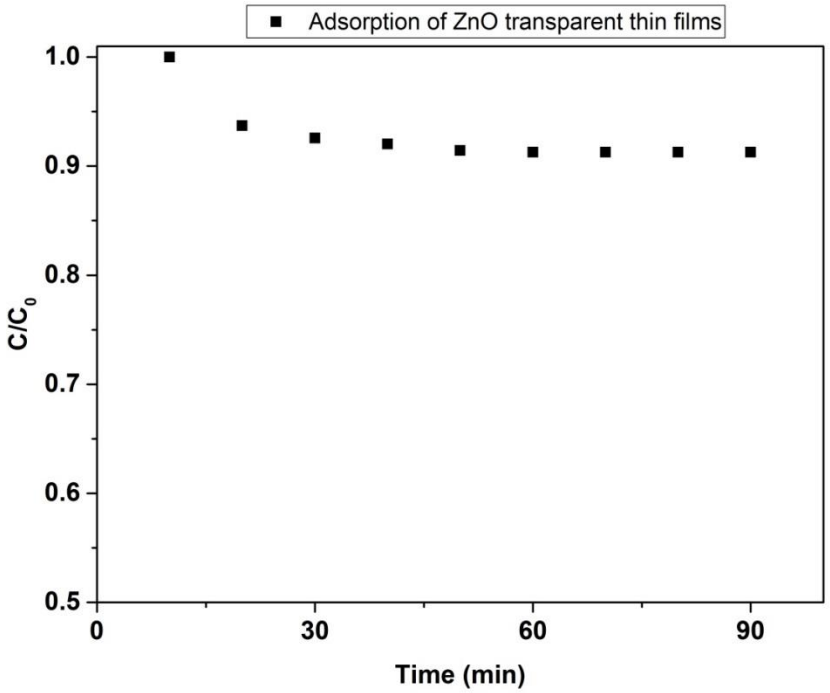

Fig. S8. Results of adsorption experiments of 4-Nitrophenmol (4-NP) on a transparent ZnO thin film.

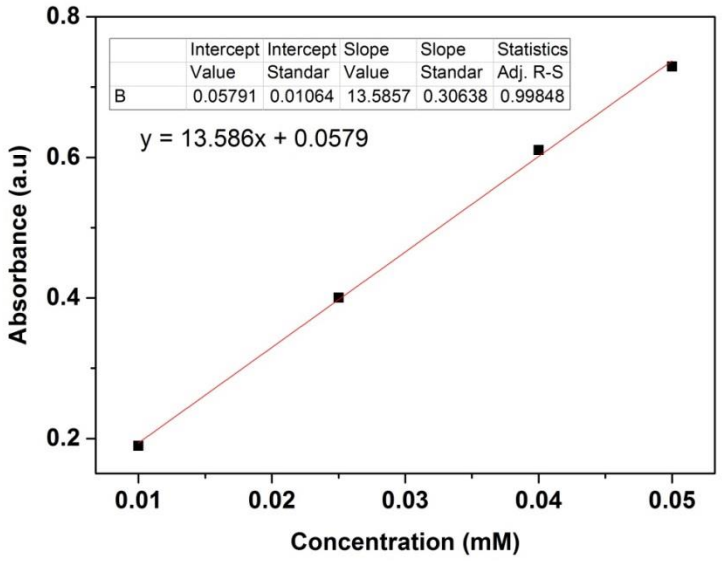

Fig. S9. Calibration curve for calculating 4-NP concentration in the photocatalytic experiments.

Multifunctional Silver Coated TiO_2 Transparent Thin Films for Photocatalytic and Antimicrobial Applications

J.G.Cuadra[1],S.Molina-Prados[2],GladysMínguez-Vega[2],Ana.C.Estrada[3],T.Trindade[3], C.Oliveira[4],M.P.Seabra[5], J.Labrincha[5],S.Porcar[1], D.Fraga[1],J.B.Carda[1]

[1] Department of Inorganic and Organic Chemistry, University Jaume I,Avda. Sos Baynat s/n, Castellon, 12071, Spain

[2] GROC-UJI, Institute of New Imaging Technologies, Universitat Jaume I, Avda. Sos Baynat s/n, Castellon, 12071, Spain

[3] Department of Chemistry, CICECO, Aveiro Institute of Nanotechnology, University of Aveiro, 3810-193 Aveiro, Portugal

[4] Department of Biology, CESAM, University of Aveiro, Campus Universitário de Santiago, 3810-193, Aveiro, Portugal

[5] Materials and Ceramic Engineering Department, CICECO, University of Aveiro, Campus Universitário de Santiago,
3810-193 Aveiro, Portugal

Supporting Information

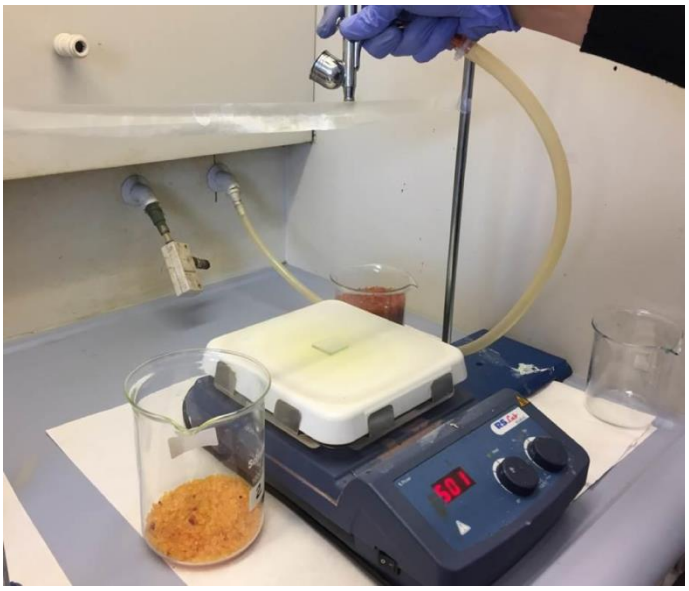

Fig.S1 Spray pyrolysis set up for the deposition of transparent TiO_2 thin films

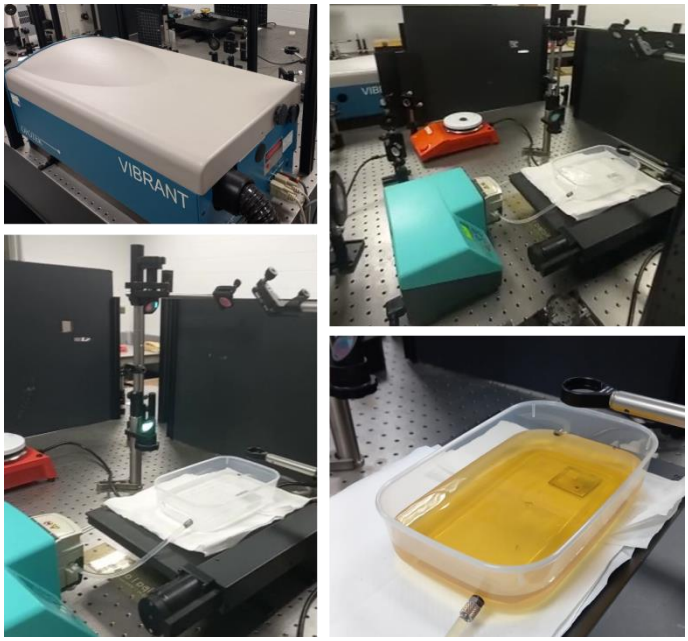

Fig.S2. Image of the Nd:YAG laser bent to the second harmonic wavelength (532 nm) synthesising silver NPs

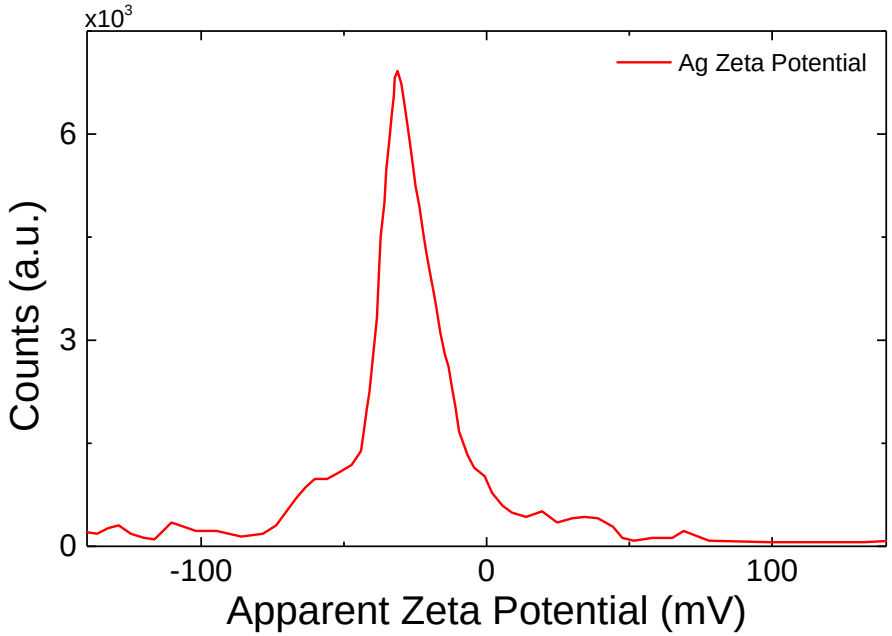

Fig.S3. Zeta potential Ag nanoparticles synthesized from PLAL before being deposited on the transparent TiO_2 thin film.

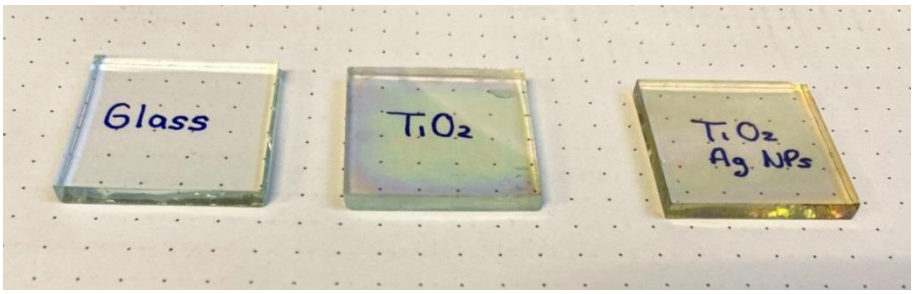

Fig.S4. Image of TiO_2 ans TiO_2-Ag NPs transparent thin films on glass

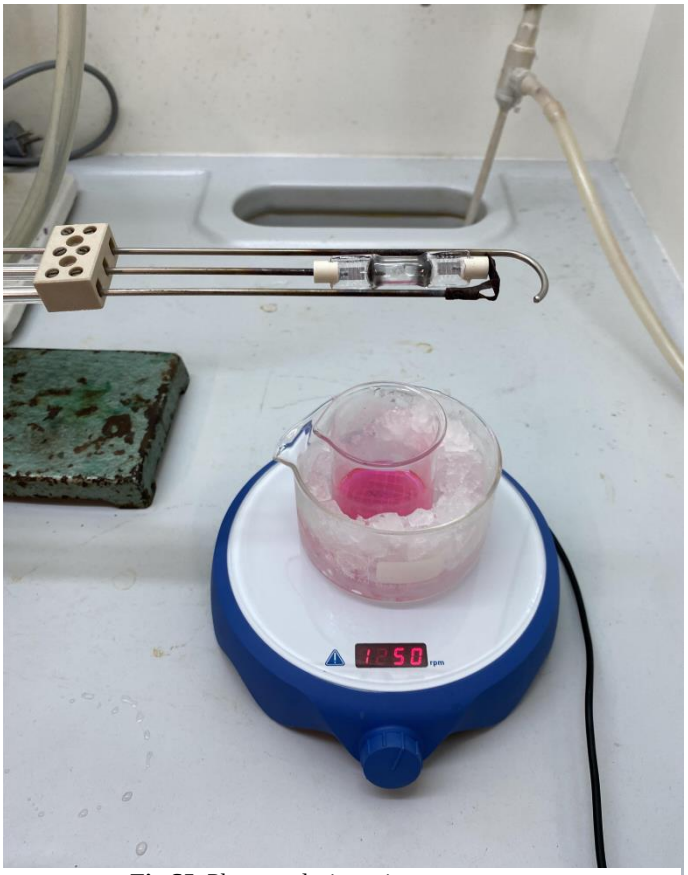

Fig.S5. Photocatalysis testing set up system

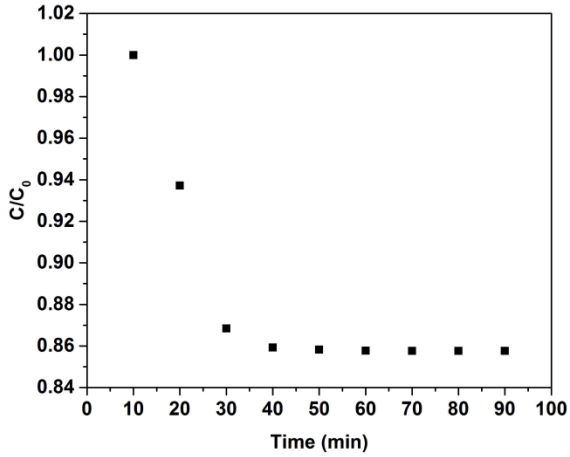

Fig.S6. Adsorption spectra of the thin films

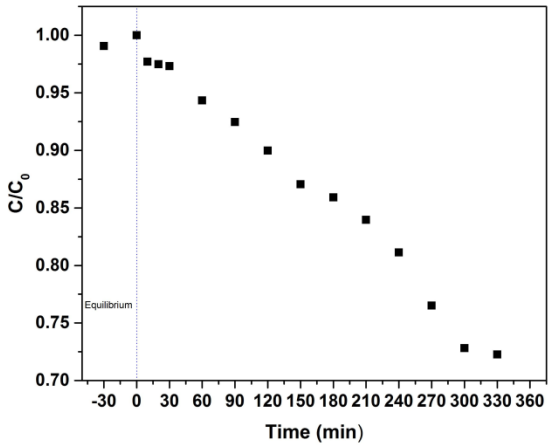

Fig.S7. The photocatalytic degeneration of RhB Rhodamine B only irradiated by UV lamp

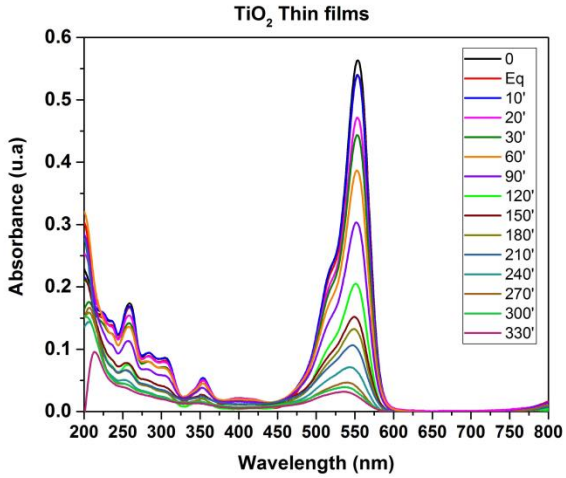

Fig.S8. UV-Vis absorption spectra's of RhB dye degradation using TiO_2

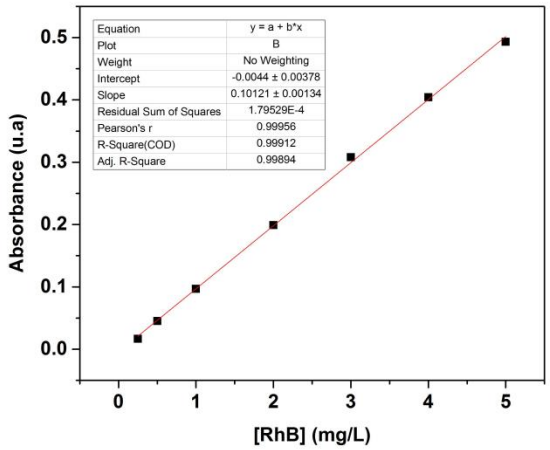

Fig.S9. Calibration line for calculation of RhB concentrations

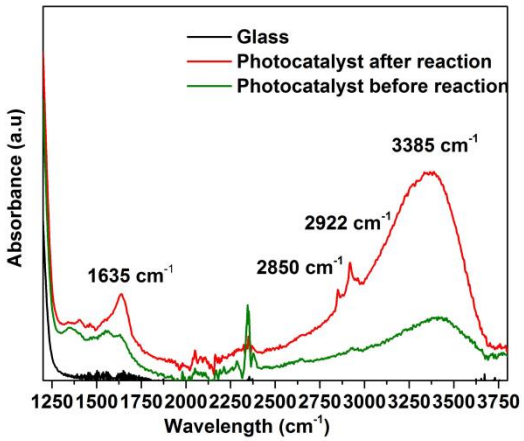

Fig.S10. FTIR spectra FTIR spectra of the TiO_2-Ag transparent thin films before and after the photocatalytic process

Table S.1 ICP-OES results of the leached amount of silver and titanium after the photocatalytic screening experiments

		0′			
Parameters	Test method	Analytical Technique	Result	Uncertainty	Units
Ti	Internal method based on ISO 11885	ICP-OES	< 80	-	µg/L
Ag	Internal method based on ISO 11885	ICP-OES	< 100	-	µg/L
		210′			
Ti	Internal method based on ISO 11885	ICP-OES	< 80	-	µg/L
Ag	Internal method based on ISO 11885	ICP-OES	< 100	-	µg/L
		300′			
Ti	Internal method based on ISO 11885	ICP-OES	< 80	-	µg/L
Ag	Internal method based on ISO 11885	ICP-OES	< 100	-	µg/L

Appendix II: R Express waiver by co-authors

UNIVERSITAT JAUME I
Escola de Doctorat · ED

João António Labrincha Baptista, como coautor/ coautora doy mi **autorización** a Jaime González Cuadra para la presentación de lassiguientes publicaciones como parte de su tesis doctoral.

Relación de publicaciones:

"Multifunctional Silver-Coated Transparent TiO_2 Thin Films for Photocatalytic and Antimicrobial Applications" J.G. Cuadra, S. Molina-Prados, Gladys Mínguez-Vega, Ana. C. Estrada, T. Trindade, C. Oliveira, M.P. Seabra, J. Labrincha, S. Porcar, R. Cadena , D. Fraga, J.B. Carda, Applied Surface Science, 617 (2023)
https://doi.org/10.1016/j.apsusc.2023.156519

"Functional Properties of Transparent ZnO Thin Films Synthetized by Using Spray Pyrolysis for Environmental and Biomedical Applications" J.G. Cuadra, A.C. Estrada, C. Oliveira, L.A. Abderrahim, S. Porcar, D. Fraga, T. Trindade, M.P. Seabra, J. Labrincha, J.B. Carda, Ceramics International, (2023),
https://doi.org/10.1016/j.ceramint.2023.07.246.

Asimismo, **renuncio** a poder utilizar estas publicaciones como parte de otra tesis doctoral.

Y para que conste firmo el presente documento,

Lugar, fecha y firma

Aveiro, 29-08-2023

Assinado por: **João António Labrincha Baptista**
Num. de Identificação: 06052832
Data: 2023.08.29 10:36:28+01'00'

CHAVE MÓVEL

Todo ello, atendiendo al artículo 28 del Reglamento de los estudios de doctorado de la Universitat Jaume I de Castelló, regulados por el RD 99/2011, en la Universitat Jaume I (Aprobado en la sesión nº 8/2020 del Consejo de Gobierno de 02 /10/2020):

"(...)

4. En el caso de publicaciones conjuntas, todas las personas coautoras deberán manifestar explícitamente su autorización para que la doctoranda o doctorando presente el trabajo como parte de su tesis y la renuncia expresa a presentar este mismo trabajo como parte de otra tesis doctoral. Esta autorización se adjuntará como documentación en el momento del inicio de evaluación de la tesis.

UNIVERSITAT JAUME I
Escola de Doctorat · ED

Juan Bautista Carda Castelló, como coautor/ coautora doy mi **autorización** a Jaime González Cuadra para la presentación de las siguientes publicaciones como parte de su tesis doctoral.

Relación de publicaciones:

"ZnO/Ag Nanocomposites with Enhanced Antimicrobial Activity" J.G. Cuadra*, L.Scalschi, B.Vicedo S. M. Gucc, V. Izquierdo-Roca, S.Porcar, D. Fraga, J.B. Carda, Appl. Sci 12, 5023 (2022) https://doi.org/10.3390/app12105023

"*Multifunctional Silver-Coated Transparent TiO_2 Thin Films for Photocatalytic and Antimicrobial Applications*" J.G. Cuadra, S. Molina-Prados, Gladys Mínguez-Vega, Ana. C. Estrada, T. Trindade, C. Oliveira, M.P. Seabra, J. Labrincha, S. Porcar, R. Cadena , D. Fraga, J.B.Carda, AppliedSurface Science, 617 (2023) https://doi.org/10.1016/j.apsusc.2023.156519.

"Functional Properties of Transparent ZnO Thin Films Synthetized by Using Spray Pyrolysis for Environmental and Biomedical Applications" J.G. Cuadra, A.C. Estrada, C. Oliveira, L.A. Abderrahim, S. Porcar, D. Fraga, T. Trindade, M.P. Seabra, J. Labrincha, J.B. Carda, Ceramics International, (2023), https://doi.org/10.1016/j.ceramint.2023.07.246.

Asimismo, **renuncio** a poder utilizar estas publicaciones como parte de otra tesis doctoral.

Y para que conste firmo el presente documento,

_____

Lugar, fecha y firma

Firmado por JUAN BAUTISTA CARDA CASTELLO - NIF:***1693** el día 31/08/2023 con un certificado emitido por ACCVCA-120

Todo ello, atendiendo al artículo 28 del Reglamento de los estudios de doctorado de la Universitat Jaume I de Castelló, regulados por el RD 99/2011, en la Universitat Jaume I (Aprobado en la sesión nº 8/2020 del Consejo de Gobierno de 02 /10/2020):

"(...)

4. En el caso de publicaciones conjuntas, todas las personas coautoras deberán manifestar explícitamente su autorización para que la doctoranda o doctorando presente el trabajo como parte de su tesis y la renuncia expresa a presentar este mismo trabajo como parte de otra tesis doctoral. Esta autorización se adjuntará como documentación en el momento del inicio de evaluación de la tesis.

UNIVERSITAT JAUME I
Escola de Doctorat · ED

(Nombre) Maxim Guc, como coautor/ coautora doy mi **autorización**
a (Nombre del doctorando/doctoranda) Jaime González Cuadra para la presentación de las siguientes publicaciones como parte de su tesis doctoral.

Relación de publicaciones:

"ZnO/Ag Nanocomposites with Enhanced Antimicrobial Activity" J.G. Cuadra*, L. Scalschi, B. Vicedo, M. Guc, V. Izquierdo-Roca, S. Porcar, D. Fraga, J.B. Carda, Appl. Sci. 12, 5023 (2022) https://doi.org/10.3390/app12105023

Asimismo, **renuncio** a poder utilizar estas publicaciones como parte de otra tesis doctoral.

Y para que conste firmo el presente documento,

Lugar, fecha y firma

Barcelona, 05/09/2023

Todo ello, atendiendo al artículo 28 del Reglamento de los estudios de doctorado de la Universitat Jaume I de Castelló, regulados por el RD 99/2011, en la Universitat Jaume I (Aprobado en la sesión nº 8/2020 del Consejo de Gobierno de 02 /10/2020):

"(...)

4. En el caso de publicaciones conjuntas, todas las personas coautoras deberán manifestar explícitamente su autorización para que la doctoranda o doctorando presente el trabajo como parte de su tesis y la renuncia expresa a presentar este mismo trabajo como parte de otra tesis doctoral. Esta autorización se adjuntará como documentación en el momento del inicio de evaluación de la tesis.

UNIVERSITAT JAUME I
Escola de Doctorat · ED

Robinson Cadena Bareño, como coautor doy mi **autorización** a Jaime González Cuadra para la presentación de las siguientes publicaciones como parte de su tesis doctoral.

Relación de publicaciones:

"*Multifunctional Silver-Coated Transparent TiO_2 Thin Films for Photocatalytic and Antimicrobial Applications*" J.G. Cuadra, S. Molina-Prados, Gladys Mínguez-Vega, Ana. C. Estrada, T. Trindade, C. Oliveira, M.P. Seabra, J. Labrincha, S. Porcar, R. Cadena , D. Fraga, J.B.Carda, AppliedSurface Science, 617 (2023) https://doi.org/10.1016/j.apsusc.2023.156519.

Asimismo, **renuncio** a poder utilizar estas publicaciones como parte de otra tesis doctoral y, para que conste, firmo el presente documento.

ROBINSON CADENA BAREÑO - NIF:11461571G

Firmado digitalmente por ROBINSON CADENA BAREÑO - NIF:11461571G
Fecha: 2023.09.08 12:43:53 +02'00'

Castellón de la Plana, España, 08 deseptiembre de 2023

Todo ello, atendiendo al artículo 28 del Reglamento de los estudios de doctorado de la Universitat Jaume I de Castelló, regulados por el RD 99/2011, en la Universitat Jaume I (Aprobado en la sesión nº 8/2020 del Consejo de Gobierno de 02 /10/2020):

"(…)

4. En el caso de publicaciones conjuntas, todas las personas coautoras deberán manifestar explícitamente su autorización para que la doctoranda o doctorando presente el trabajo como parte de su tesis y la renuncia expresa a presentar este mismo trabajo como parte de otra tesis doctoral. Esta autorización se adjuntará como documentación en el momento del inicio de evaluación de la tesis.

UNIVERSITAT JAUME I
Escola de Doctorat · ED

(Nombre)Samuel Porcar García, como coautor/ coautora doy mi **autorización** a (Nombre del doctorando/doctoranda) Jaime González Cuadra para la presentación de las siguientes publicaciones como parte de su tesis doctoral.

Relación de publicaciones:

"ZnO/Ag Nanocomposites with Enhanced Antimicrobial Activity" J.G. Cuadra*, L.Scalschi, B.Vicedo S. M. Gucc, V. Izquierdo-Roca, S.Porcar, D. Fraga, J.B. Carda, Appl. Sci 12, 5023 (2022) https://doi.org/10.3390/app12105023

"*Multifunctional Silver-Coated Transparent TiO_2 Thin Films for Photocatalytic and Antimicrobial Applications*" J.G. Cuadra, S. Molina-Prados, Gladys Mínguez-Vega, Ana. C. Estrada, T. Trindade, C. Oliveira, M.P. Seabra, J. Labrincha, S. Porcar, R. Cadena , D. Fraga, J.B.Carda, AppliedSurface Science, 617 (2023) https://doi.org/10.1016/j.apsusc.2023.156519.

"Functional Properties of Transparent ZnO Thin Films Synthetized by Using Spray Pyrolysis for Environmental and Biomedical Applications" J.G. Cuadra, A.C. Estrada, C. Oliveira, L.A. Abderrahim, S. Porcar, D. Fraga, T. Trindade, M.P. Seabra, J. Labrincha, J.B. Carda, Ceramics International, (2023), https://doi.org/10.1016/j.ceramint.2023.07.246.

Asimismo, **renuncio** a poder utilizar estas publicaciones como parte de otra tesis doctoral.

Y para que conste firmo el presente documento,

Firmado por SAMUEL PORCAR GARCIA - NIF:20905216X el día 29/08/2023

Samuel Porcar García, Castellón de la Plana a 29/08/2023

Todo ello, atendiendo al artículo 28 del Reglamento de los estudios de doctorado de la Universitat Jaume I de Castelló, regulados por el RD 99/2011, en la Universitat Jaume I (Aprobado en la sesión nº 8/2020 del Consejo de Gobierno de 02 /10/2020):

"(...)

4. En el caso de publicaciones conjuntas, todas las personas coautoras deberán manifestar explícitamente su autorización para que la doctoranda o doctorando presente el trabajo como parte de su tesis y la renuncia expresa a presentar este mismo trabajo como parte de otra tesis doctoral. Esta autorización se adjuntará como documentación en el momento del inicio de evaluación de la tesis.

UNIVERSITAT JAUME I
Escola de Doctorat · ED

Sergio Fernández Molina-Prados, como coautor/ coautora doy mi **autorización** a Jaime González Cuadra para la presentación de lassiguientes publicaciones como parte de su tesis doctoral.

Relación de publicaciones:

"Multifunctional Silver-Coated Transparent TiO_2 Thin Films for Photocatalytic and Antimicrobial Applications" J.G. Cuadra, S. Molina-Prados, Gladys Mínguez-Vega, Ana. C. Estrada, T. Trindade, C. Oliveira, M.P. Seabra, J. Labrincha, S. Porcar, R. Cadena , D. Fraga, J.B. Carda, Applied Surface Science, 617 (2023)
https://doi.org/10.1016/j.apsusc.2023.156519

Asimismo, **renuncio** a poder utilizar estas publicaciones como parte de otra tesis doctoral.

Y para que conste firmo el presente documento,

Lugar, fecha y firma

Firmado por SERGIO FERNANDEZ MOLINA-PRADOS - NIF:21703459S el día 31/08/2023 con un certificado emitido por ACCVCA-120

31 de Agosto de 2023

Todo ello, atendiendo al artículo 28 del Reglamento de los estudios de doctorado de la Universitat Jaume I de Castelló, regulados por el RD 99/2011, en la Universitat Jaume I (Aprobado en la sesión nº 8/2020 del Consejo de Gobierno de 02 /10/2020):

"(...)

4. En el caso de publicaciones conjuntas, todas las personas coautoras deberán manifestar explícitamente su autorización para que la doctoranda o doctorando presente el trabajo como parte de su tesis y la renuncia expresa a presentar este mismo trabajo como parte de otra tesis doctoral. Esta autorización se adjuntará como documentación en el momento del inicio de evaluación de la tesis.

UNIVERSITAT JAUME I
Escola de Doctorat · ED

Tito Trindade, como coautor doy mi **autorización**
a Jaime González Cuadra para la presentación de lassiguientes publicaciones como parte de su tesis doctoral.

Relación de publicaciones:

"Multifunctional Silver-Coated Transparent TiO_2 Thin Films for Photocatalytic and Antimicrobial Applications" J.G. Cuadra, S. Molina-Prados, Gladys Mínguez-Vega, Ana. C. Estrada, T. Trindade, C. Oliveira, M.P. Seabra, J. Labrincha, S. Porcar, R. Cadena , D. Fraga, J.B. Carda, Applied Surface Science, 617 (2023)
https://doi.org/10.1016/j.apsusc.2023.156519

"Functional Properties of Transparent ZnO Thin Films Synthetized by Using Spray Pyrolysis for Environmental and Biomedical Applications" J.G. Cuadra, A.C. Estrada, C. Oliveira, L.A. Abderrahim, S. Porcar, D. Fraga, T. Trindade, M.P. Seabra, J. Labrincha, J.B. Carda, Ceramics International, (2023),
https://doi.org/10.1016/j.ceramint.2023.07.246.

Asimismo, **renuncio** a poder utilizar estas publicaciones como parte de otra tesis doctoral.

Y para que conste firmo el presente documento,

Universidade de Aveiro, 31-8-2023

Tito Trindade

Todo ello, atendiendo al artículo 28 del Reglamento de los estudios de doctorado de la Universitat Jaume I de Castelló, regulados por el RD 99/2011, en la Universitat Jaume I (Aprobado en la sesión nº 8/2020 del Consejo de Gobierno de 02 /10/2020):

"(...)

4. En el caso de publicaciones conjuntas, todas las personas coautoras deberán manifestar explícitamente su autorización para que la doctoranda o doctorando presente el trabajo como parte de su tesis y la renuncia expresa a presentar este mismo trabajo como parte de otra tesis doctoral. Esta autorización se adjuntará como documentación en el momento del inicio de evaluación de la tesis.

UNIVERSITAT JAUME I
Escola de Doctorat · ED

(Nombre) Victor Izquierdo-Roca, como coautor/ coautora doy mi **autorización** a (Nombre del doctorando/doctoranda) Jaime González Cuadra para la presentación de las siguientes publicaciones como parte de su tesis doctoral.

Relación de publicaciones:

"ZnO/Ag Nanocomposites with Enhanced Antimicrobial Activity" J.G. Cuadra*, L. Scalschi, B. Vicedo, M. Guc, V. Izquierdo-Roca, S. Porcar, D. Fraga, J.B. Carda, Appl. Sci. 12, 5023 (2022) https://doi.org/10.3390/app12105023

Asimismo, **renuncio** a poder utilizar estas publicaciones como parte de otra tesis doctoral.

Y para que conste firmo el presente documento,

Lugar, fecha y firma

Barcelona, 07/09/2023

Todo ello, atendiendo al artículo 28 del Reglamento de los estudios de doctorado de la Universitat Jaume I de Castelló, regulados por el RD 99/2011, en la Universitat Jaume I (Aprobado en la sesión nº 8/2020 del Consejo de Gobierno de 02 /10/2020):

"(...)

4. En el caso de publicaciones conjuntas, todas las personas coautoras deberán manifestar explícitamente su autorización para que la doctoranda o doctorando presente el trabajo como parte de su tesis y la renuncia expresa a presentar este mismo trabajo como parte de otra tesis doctoral. Esta autorización se adjuntará como documentación en el momento del inicio de evaluación de la tesis.

UNIVERSITAT JAUME I
Escola de Doctorat · ED

(Nombre) Loredana Maria Scalschi, como coautor/ coautora doy mi **autorización** a (Nombre del doctorando/doctoranda) Jaime González Cuadra para la presentación de las siguientes publicaciones como parte de su tesis doctoral.

Relación de publicaciones:

"ZnO/Ag Nanocomposites with Enhanced Antimicrobial Activity" J.G. Cuadra*, L.Scalschi, B.Vicedo S. M. Gucc, V. Izquierdo-Roca, S.Porcar, D. Fraga, J.B. Carda, Appl. Sci 12, 5023 (2022) https://doi.org/10.3390/app12105023

Asimismo, **renuncio** a poder utilizar estas publicaciones como parte de otra tesis doctoral.

Y para que conste firmo el presente documento,

LOREDANA MARIA| SCALSCHI

Firmado digitalmente por LOREDANA MARIA|SCALSCHI
Fecha: 2023.08.29 23:18:17 +02'00'

Lugar, fecha y firma

Todo ello, atendiendo al artículo 28 del Reglamento de los estudios de doctorado de la Universitat Jaume I de Castelló, regulados por el RD 99/2011, en la Universitat Jaume I (Aprobado en la sesión nº 8/2020 del Consejo de Gobierno de 02 /10/2020):

"(...)

4. En el caso de publicaciones conjuntas, todas las personas coautoras deberán manifestar explícitamente su autorización para que la doctoranda o doctorando presente el trabajo como parte de su tesis y la renuncia expresa a presentar este mismo trabajo como parte de otra tesis doctoral. Esta autorización se adjuntará como documentación en el momento del inicio de evaluación de la tesis.

UNIVERSITAT JAUME I
Escola de Doctorat · ED

Abderrahim Lahlahi Attalhaoui, como coautor/ coautora doy mi **autorización**
a (Nombre del doctorando/doctoranda) Jaime González Cuadra para la presentación de las siguientes publicaciones como parte de su tesis doctoral.

Relación de publicaciones:

"Functional Properties of Transparent ZnO Thin Films Synthetized by Using Spray Pyrolysis for Environmental and Biomedical Applications" J.G. Cuadra, A.C. Estrada, C. Oliveira, L.A. Abderrahim, S. Porcar, D. Fraga, T. Trindade, M.P. Seabra, J. Labrincha, J.B. Carda, Ceramics International, (2023), https://doi.org/10.1016/j.ceramint.2023.07.246.

Asimismo, **renuncio** a poder utilizar estas publicaciones como parte de otra tesis doctoral.

Y para que conste firmo el presente documento,

Castellón, 4 de septiembre del 2023

Firmado por ABDERRAHIM LAHLAHI ATTALHAOUI - NIF:***8062** el día 04/09/2023 con un certificado emitido

Todo ello, atendiendo al artículo 28 del Reglamento de los estudios de doctorado de la Universitat Jaume I de Castelló, regulados por el RD 99/2011, en la Universitat Jaume I (Aprobado en la sesión nº 8/2020 del Consejo de Gobierno de 02 /10/2020):

"(...)

4. En el caso de publicaciones conjuntas, todas las personas coautoras deberán manifestar explícitamente su autorización para que la doctoranda o doctorando presente el trabajo como parte de su tesis y la renuncia expresa a presentar este mismo trabajo como parte de otra tesis doctoral. Esta autorización se adjuntará como documentación en el momento del inicio de evaluación de la tesis.

UNIVERSITAT JAUME I
Escola de Doctorat · ED

Ana Cristina Estrada, como coautora doy mi **autorización**
a Jaime González Cuadra para la presentación de lassiguientes publicaciones como parte de su tesis doctoral.

Relación de publicaciones:

"Multifunctional Silver-Coated Transparent TiO_2 Thin Films for Photocatalytic and Antimicrobial Applications" J.G. Cuadra, S. Molina-Prados, Gladys Mínguez-Vega, Ana. C. Estrada, T. Trindade, C. Oliveira, M.P. Seabra, J. Labrincha, S. Porcar, R. Cadena , D. Fraga, J.B. Carda, Applied Surface Science, 617 (2023)
https://doi.org/10.1016/j.apsusc.2023.156519

"Functional Properties of Transparent ZnO Thin Films Synthetized by Using Spray Pyrolysis for Environmental and Biomedical Applications" J.G. Cuadra, A.C. Estrada, C. Oliveira, L.A. Abderrahim, S. Porcar, D. Fraga, T. Trindade, M.P. Seabra, J. Labrincha, J.B. Carda, Ceramics International, (2023),
https://doi.org/10.1016/j.ceramint.2023.07.246.

Asimismo, **renuncio** a poder utilizar estas publicaciones como parte de otra tesis doctoral.

Y para que conste firmo el presente documento,

Universidade de Aveiro, 30/08/2023

A Estrada

Todo ello, atendiendo al artículo 28 del Reglamento de los estudios de doctorado de la Universitat Jaume I de Castelló, regulados por el RD 99/2011, en la Universitat Jaume I (Aprobado en la sesión nº 8/2020 del Consejo de Gobierno de 02 /10/2020):

"(...)

4. En el caso de publicaciones conjuntas, todas las personas coautoras deberán manifestar explícitamente su autorización para que la doctoranda o doctorando presente el trabajo como parte de su tesis y la renuncia expresa a presentar este mismo trabajo como parte de otra tesis doctoral. Esta autorización se adjuntará como documentación en el momento del inicio de evaluación de la tesis.

UNIVERSITAT JAUME I
Escola de Doctorat · ED

Begonya Vicedo, como coautora doy mi **autorización**
a Jaime González Cuadra para la presentación de lassiguientes publicaciones como parte de su tesis doctoral.

Relación de publicaciones:

"ZnO/Ag Nanocomposites with Enhanced Antimicrobial Activity" J.G. Cuadra*, L.Scalschi, B.Vicedo S. M. Gucc, V. Izquierdo-Roca, S.Porcar, D. Fraga, J.B. Carda, Appl. Sci 12, 5023 (2022) https://doi.org/10.3390/app12105023

Asimismo, **renuncio** a poder utilizar estas publicaciones como parte de otra tesis doctoral.

Y para que conste firmo el presente documento,

BEGONYA|
VICEDO|JOVER

Firmado digitalmente por BEGONYA|VICEDO|JOVER
Nombre de reconocimiento (DN): cn=BEGONYA|VICEDO|JOVER, serialNumber=74085075M, givenName=BEGONYA, sn=VICEDO JOVER, ou=CIUDADANOS, o=ACCV, c=ES
Fecha: 2023.08.29 11:36:11 +02'00'

Castelló de la Plana, 29/08/2023

Todo ello, atendiendo al artículo 28 del Reglamento de los estudios de doctorado de la Universitat Jaume I de Castelló, regulados por el RD 99/2011, en la Universitat Jaume I (Aprobado en la sesión nº 8/2020 del Consejo de Gobierno de 02 /10/2020):

"(...)

4. En el caso de publicaciones conjuntas, todas las personas coautoras deberán manifestar explícitamente su autorización para que la doctoranda o doctorando presente el trabajo como parte de su tesis y la renuncia expresa a presentar este mismo trabajo como parte de otra tesis doctoral. Esta autorización se adjuntará como documentación en el momento del inicio de evaluación de la tesis.

UNIVERSITAT JAUME I
Escola de Doctorat · ED

Cláudia Sofia Soares de Oliveira, como coautor/ coautora doy mi **autorización** a Jaime González Cuadra para la presentación de lassiguientes publicaciones como parte de su tesis doctoral.

Relación de publicaciones:

"Multifunctional Silver-Coated Transparent TiO_2 Thin Films for Photocatalytic and Antimicrobial Applications" J.G. Cuadra, S. Molina-Prados, Gladys Mínguez-Vega, Ana. C. Estrada, T. Trindade, C. Oliveira, M.P. Seabra, J. Labrincha, S. Porcar, R. Cadena , D. Fraga, J.B. Carda, Applied Surface Science, 617 (2023)
https://doi.org/10.1016/j.apsusc.2023.156519

"Functional Properties of Transparent ZnO Thin Films Synthetized by Using Spray Pyrolysis for Environmental and Biomedical Applications" J.G. Cuadra, A.C. Estrada, C. Oliveira, L.A. Abderrahim, S. Porcar, D. Fraga, T. Trindade, M.P. Seabra, J. Labrincha, J.B. Carda, Ceramics International, (2023),
https://doi.org/10.1016/j.ceramint.2023.07.246.

Asimismo, **renuncio** a poder utilizar estas publicaciones como parte de otra tesis doctoral.

Y para que conste firmo el presente documento,

Aveiro, 4/9/2023

Cláudia Sofia Soares de Oliveira

Todo ello, atendiendo al artículo 28 del Reglamento de los estudios de doctorado de la Universitat Jaume I de Castelló, regulados por el RD 99/2011, en la Universitat Jaume I (Aprobado en la sesión nº 8/2020 del Consejo de Gobierno de 02 /10/2020):

"(...)

4. En el caso de publicaciones conjuntas, todas las personas coautoras deberán manifestar explícitamente su autorización para que la doctoranda o doctorando presente el trabajo como parte de su tesis y la renuncia expresa a presentar este mismo trabajo como parte de otra tesis doctoral. Esta autorización se adjuntará como documentación en el momento del inicio de evaluación de la tesis.

UNIVERSITAT JAUME I
Escola de Doctorat · ED

Diego Fraga Chiva, como coautor/ coautora doy mi **autorización** a Jaime González Cuadra para la presentación de lassiguientes publicaciones como parte de su tesis doctoral.

Relación de publicaciones:

"ZnO/Ag Nanocomposites with Enhanced Antimicrobial Activity" J.G. Cuadra*, L.Scalschi, B.Vicedo S. M. Gucc, V. Izquierdo-Roca, S.Porcar, D. Fraga, J.B. Carda, Appl. Sci 12, 5023 (2022) https://doi.org/10.3390/app12105023

"*Multifunctional Silver-Coated Transparent TiO_2 Thin Films for Photocatalytic and Antimicrobial Applications*" J.G. Cuadra, S. Molina-Prados, Gladys Mínguez-Vega, Ana. C. Estrada, T. Trindade, C. Oliveira, M.P. Seabra, J. Labrincha, S. Porcar, R. Cadena , D. Fraga, J.B.Carda, AppliedSurface Science, 617 (2023) https://doi.org/10.1016/j.apsusc.2023.156519.

"Functional Properties of Transparent ZnO Thin Films Synthetized by Using Spray Pyrolysis for Environmental and Biomedical Applications" J.G. Cuadra, A.C. Estrada, C. Oliveira, L.A. Abderrahim, S. Porcar, D. Fraga, T. Trindade, M.P. Seabra, J. Labrincha, J.B. Carda, Ceramics International, (2023), https://doi.org/10.1016/j.ceramint.2023.07.246.

Asimismo, **renuncio** a poder utilizar estas publicaciones como parte de otra tesis doctoral.

Y para que conste firmo el presente documento,

DIEGO|FRAGA|CHIVA

Firmado digitalmente por DIEGO|FRAGA|CHIVA
Fecha: 2023.08.31 11:03:33 +02'00'

Lugar, fecha y firma

Todo ello, atendiendo al artículo 28 del Reglamento de los estudios de doctorado de la Universitat Jaume I de Castelló, regulados por el RD 99/2011, en la Universitat Jaume I (Aprobado en la sesión nº 8/2020 del Consejo de Gobierno de 02 /10/2020):

"(...)

4. En el caso de publicaciones conjuntas, todas las personas coautoras deberán manifestar explícitamente su autorización para que la doctoranda o doctorando presente el trabajo como parte de su tesis y la renuncia expresa a presentar este mismo trabajo como parte de otra tesis doctoral. Esta autorización se adjuntará como documentación en el momento del inicio de evaluación de la tesis.

UNIVERSITAT JAUME I
Escola de Doctorat · ED

Gladys Mínguez Vega, como coautor/ coautora doy mi **autorización** a Jaime González Cuadra para la presentación de lassiguientes publicaciones como parte de su tesis doctoral.

Relación de publicaciones:

"Multifunctional Silver-Coated Transparent TiO_2 Thin Films for Photocatalytic and Antimicrobial Applications" J.G. Cuadra, S. Molina-Prados, Gladys Mínguez-Vega, Ana. C. Estrada, T. Trindade, C. Oliveira, M.P. Seabra, J. Labrincha, S. Porcar, R. Cadena , D. Fraga, J.B. Carda, Applied Surface Science, 617 (2023) https://doi.org/10.1016/j.apsusc.2023.156519

Asimismo, **renuncio** a poder utilizar estas publicaciones como parte de otra tesis doctoral.

Y para que conste firmo el presente documento,

Castelló, 30 de Agosto de 2023

MARIA GLADIS| MINGUEZ| VEGA

Firmado digitalmente por MARIA GLADIS| MINGUEZ|VEGA
Fecha: 2023.08.30 09:12:21 +02'00'

Todo ello, atendiendo al artículo 28 del Reglamento de los estudios de doctorado de la Universitat Jaume I de Castelló, regulados por el RD 99/2011, en la Universitat Jaume I (Aprobado en la sesión nº 8/2020 del Consejo de Gobierno de 02 /10/2020):

"(...)

4. En el caso de publicaciones conjuntas, todas las personas coautoras deberán manifestar explícitamente su autorización para que la doctoranda o doctorando presente el trabajo como parte de su tesis y la renuncia expresa a presentar este mismo trabajo como parte de otra tesis doctoral. Esta autorización se adjuntará como documentación en el momento del inicio de evaluación de la tesis.